INL/JOU-19-57010-Revision-0

Fuel-cladding chemical interaction in an annular U-10wt.%Zr fuel with HT-9 cladding

February 2021

Xiang Liu, Luca Capriotti, Tiankai Yao, Jason M. Harp, Michael T Benson, Lingfeng He, Yachun Wang, Fei Teng

Changing the World's Energy Future

INL is a U.S. Department of Energy National Laboratory operated by Battelle Energy Alliance, LLC

INL/JOU-19-57010-Revision-0

Fuel-cladding chemical interaction in an annular U-10wt.%Zr fuel with HT-9 cladding

Xiang Liu, Luca Capriotti, Tiankai Yao, Jason M. Harp, Michael T Benson, Lingfeng He, Yachun Wang, Fei Teng

February 2021

Idaho National Laboratory
Idaho Falls, Idaho 83415

http://www.inl.gov

Prepared for the
U.S. Department of Energy
Under DOE Idaho Operations Office
Contract DE-AC07-05ID14517

Fuel-cladding chemical interaction of a prototype annular U-10Zr fuel with Fe-12Cr ferritic/martensitic HT-9 cladding

Xiang Liu[a,*], Luca Capriotti[a,*], Tiankai Yao[a], Jason M. Harp[b], Michael T. Benson[a], Yachun Wang[a], Fei Teng[a], Lingfeng He[a]

[a]*Idaho National Laboratory, Idaho Falls, ID 83415, USA*
[b]*Oak Ridge National Laboratory, Oak Ridge, TN 37831, USA*

[*]Corresponding authors
Email addresses: Xiang.liu@inl.gov (X.Liu), Luca.Capriotti@inl.gov (L. Capriotti)

Abstract

As an alternative fuel form, the annular metallic fuel design eliminates the liquid sodium bond between the fuel and the cladding, providing back-end fuel cycle and other benefits. The fuel-cladding chemical interaction (FCCI) of annular fuel also presents new features. Here, state-of-the-art electron microscopy and spectroscopy techniques were used to study the FCCI of a prototype annular U-10wt%Zr (U-10Zr) fuel with ferritic/martensitic HT-9 cladding irradiated to 3.3% fission per initial heavy atom. Compared with sodium-bonded solid fuels, negligible amounts of lanthanides were found in the FCCI layer in the investigated helium-bonded annular fuel. Instead, most lanthanides were retained in the newly formed UZr_2 phase in the fuel center region. The interdiffusion of iron and uranium resulted in tetragonal (**U**,Zr)$_6$Fe phase (space group I4/mcm) and cubic (**U**,Zr)(**Fe**,Cr)$_2$ phase (space group $Fd\bar{3}m$). The (**U**,Zr)(**Fe**,Cr)$_2$ phase contains a high density of voids and intergranular uranium monocarbides of NaCl-type crystal structure (space group $Fm\bar{3}m$). At the interdiffusion zone and inner cladding interface, a porous lamellar structure composed of alternating Cr-rich layers and U-rich layers was observed. Next to the lamellar region, the unexpected phase transformation from body-centered cubic ferrite (α-Fe) to tetragonal binary Fe-Cr σ phase (space group $P4_2/mnm$) occurred, and tetragonal Fe-Cr-U-Si phase (space group I4/mmm) was identified. Due to the diffusion of carbon into the interdiffusion zone, carbon depletion inside the HT-9 led to the disappearance of the martensite lath structure, and intergranular U-rich carbides formed as a result of the diffusion of uranium into the cladding. These detailed new findings reveal the unique features of the FCCI behavior of annular U-Zr fuels, which could be a promising alternative fuel form for high burnup fast reactor applications.

Keywords: Fuel-cladding chemical interaction (FCCI); metallic fuel; advanced nuclear fuel; transmission electron microscopy (TEM); HT-9 cladding; phase transformation.

1. Introduction

Metallic U-Zr alloy fuels are candidate fuel types for sodium-cooled fast reactors (SFR) [1–4]. Irradiation-induced swelling [5], fission gas release [6], and fuel-cladding chemical interaction (FCCI) [7,8] are key limiting factors that restrict fuel performance at high burnup. Historically, SFR fuel designs were adapted to mitigate the challenges posed by swelling and fission gas release. A low smear density was employed to accommodate the rapid swelling and avoid premature mechanical failure of the cladding. A long gas plenum was used to accommodate the released fission gas. Limitations on the peak inner cladding temperature of fuel pins below 625 °C were historically used to mitigate FCCI. However, this limited the

maximum outlet temperature of SFR to between 500–550 °C, which excludes SFR use from many potential process heat applications [9]. One goal of current SFR fuel design should be to develop technologies that enable the expanded deployment of SFR technology to different applications. Three possible applications of SFR technology are actinide management, process heat, and once-through fuel for power or test reactor applications [10]. Annular metallic fuel that is sodium free is an exemplary technology that can help enable once-through fuel scenarios.

Swelling in metallic fuel can be accommodated in many ways [11]. Most often, it was accommodated by placing a solid fuel into a larger cladding tube and filling the space between with a high thermal conductivity liquid, like sodium. However, sodium-bonded spent fuels are considered mixed hazardous waste in a once-through fuel cycle and require a costly sodium removal process prior to disposal [12]. As a possible alternative to the historical solid U-Zr fuels, annular U-Zr fuels are being evaluated due to their back-end fuel cycle benefits. In the annular U-Zr fuel design shown in Figure 1, the small gap between the fuel and the cladding allows helium to be used as the bonding material, eliminating the hazards associated with sodium. However, because of the differences in bonding material and fuel design, the FCCI behavior of these annular U-Zr fuels could be very different from historical solid U-Zr fuels.

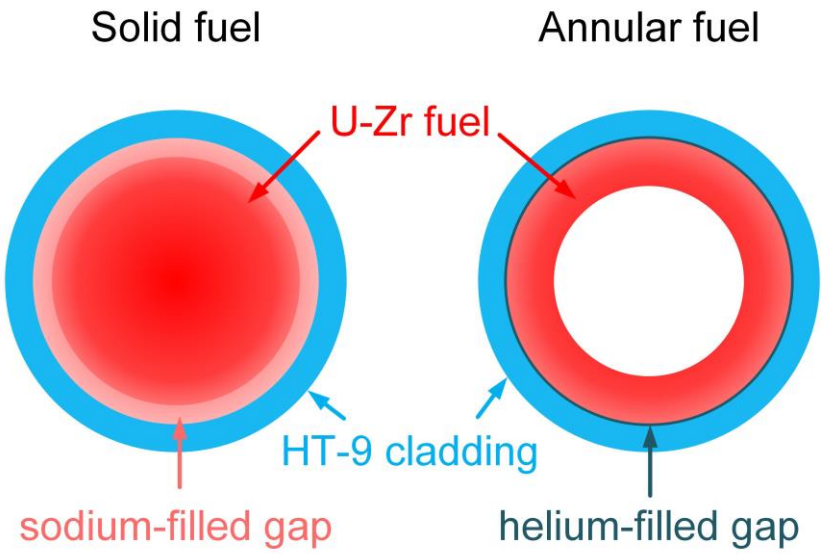

Figure 1. Illustration of the differences in the design of sodium-bonded solid fuel versus helium-bonded annular fuel.

Metallic fuel FCCI can involve both fission products interaction with cladding and interaction between the primary fuel elements and the cladding. On one hand, as the lanthanide fission products diffuse down the thermal gradient and interact with cladding constituents, a brittle wastage zone along the inner surface of the cladding is formed [13]. This wastage zone poses threats to the mechanical integrity of the cladding. On the other hand, the diffusion of iron into the fuel can form low melting eutectic phases and potentially lead to fuel melting. For instance, two representative phases found in U-Zr fuel with Fe base cladding interdiffusion studies [14–21] are U_6Fe and UFe_2, the melting points of which are ~1102 K and ~1504 K, respectively [22]. The melting point can be further lowered by the addition of plutonium in U-Pu-Zr fuels [23,24]. Direct interaction between cladding elements and fuel was also observed in the irradiation experience of U-5Fs alloys [25].

Previous studies found that Zr-rich regions (Zr-rind) at the fuel periphery could act as diffusion barriers to reduce FCCI, and the Zr-rind was assumed to be a result of impurities during fuel fabrication [7]. Zr liners were then proposed as one approach to mitigate FCCI.

The vast majority of existing irradiated metallic alloy fuel pins from past U.S. fast reactor fuel research programs were composed of U-10wt% Zr (U-10Zr) fuel sodium bonded to HT-9 cladding with a smear density of ~75% [3,26] to accommodate fuel swelling. The liquid sodium bond was chosen to ensure efficient heat transfer from the fuel to the cladding. HT-9 is a Fe-12Cr base ferritic/martensitic alloy that shows excellent swelling resistance and compatibility with metallic fuels [27–29]. The FCCI of HT-9 cladding with U-Zr and U-Pu-Zr fuels were investigated in previous scanning electron microscopy (SEM) [13,26,30] and electron micro probe analyzer (EPMA) [13] studies, and it was found that lanthanides penetrated into the cladding and iron diffused into the fuel. Previous studies [7,31] also proposed that the transport of lanthanides could be through liquid-like diffusion via interconnected pores filled with sodium and cesium. The liquid sodium bond used in historical solid U-Zr fuels might have played an important role in the transportation of lanthanides to the FCCI region.

In this study, the FCCI behavior of an sodium-free helium-bonded annular U-10Zr fuel with HT-9 cladding was investigated in detail for the first time, utilizing the recently available advanced electron microscopy and spectroscopy capabilities for highly radioactive samples at the Materials and Fuels Complex (MFC), Idaho National Laboratory (INL). The results shed light on the unique FCCI behavior of annular U-10Zr fuel, which could be a promising fuel type for SFR applications.

2. Experimental

2.1 Materials

The investigated fuel is an annular U-10Zr fuel from the Advanced Fuels Campaign (AFC) series (AFC-3A) of irradiation experiments. As part of the AFC-3A irradiation, this fuel rodlet was designated AFC-3A R4, and the corresponding fuel fabrication was described in Fielding *et al.* [32], and pre-irradiation characterization was reported in O'Holleran *et al.* [33]. Post-irradiation examination (PIE) data and the overall irradiation performance of AFC-3A and AFC-3B fuels were discussed in a recent study [12].

The AFC-3A R4 fuel rodlet has a nominal composition of U-10wt%Zr. The rodlet is in the annular fuel form with an inner diameter of 3.25 mm, an outer diameter of 4.86 mm, and a total height of 38.0 mm. The nominal smear density is 55%, and the as-fabricated smear density is 53.8%. The sodium bond was eliminated, and helium was used as the bonding material instead. The fuel alloy was fabricated by mixing uranium and zirconium metals in an arc melter and homogenized through several melts, followed by injection casting into a quartz mold with an inner quartz core. After casting, the inner quartz core was removed by drilling, and the outside mold was removed by breaking the quartz off the outside of the cast pin. The fuel slug was then cut into the desired length for irradiation testing.

2.2 Neutron irradiation

The as-fabricated annular U-10Zr fuel was sealed inside ferritic/martensitic steel HT-9. The cladding had an outer diameter of 5.842 mm and a wall thickness of 0.4445 mm. The nominal chemical composition of the HT-9 cladding tube is listed in Table 1.

Table 1. Nominal chemical composition of the HT-9 cladding tube.

Element	Fe	C	Mn	P	S	Si	Ni	Cr	Mo	Cu	V	Co	W
wt%	Bal.	0.22	0.56	0.13	0.002	0.30	0.57	11.53	1.08	0.02	0.31	0.02	0.52

at%	Bal.	1.007	0.56	0.23	0.003	0.587	0.534	12.19	0.619	0.017	0.335	0.0187	0.1555

The rodlet was sealed inside a cylindrical capsule container that served as the primary boundary between the rodlet and the coolant. The capsules were back-filled with helium gas. The temperature of the rodlets is controlled by the gap between the rodlets and the capsule and by the enrichment level of the fuel.

The investigated annular fuel was part of the AFC-3 irradiation experiments, which were performed at the INL Advanced Test Reactor (ATR). The AFC capsules were irradiated in a cadmium-shrouded position that hardens the ATR neutron spectrum to create a radial power profile appropriate for fast spectrum fuel testing [34–36]. Detailed description of the irradiation experiment setup can be found in recent works [12,35]. The irradiation history, including the linear heat generation rate (LHGR, in unit of W/cm) and peak inner cladding temperature (PICT) of each effective full-power day (EFPD), is plotted in Figure 2. As mentioned in a previous AFC-3 study [12], the PICT was calculated from the LHGR and assumed as-built dimensions of the rodlets and capsules. However, due to fabrication defects, the capsules had poor cylindricity in the inner bore. The actual local cladding temperature could have noticeable uncertainty.

The AFC-3A and 3B irradiation lasted for about 120 EFPD. The burnup of the AFC-3A R4 rodlet was determined to be 3.3% fission per initial heavy metal atom (FIMA), and the fission density was about 8.91 $\times 10^{20}$ fission/cm^3.

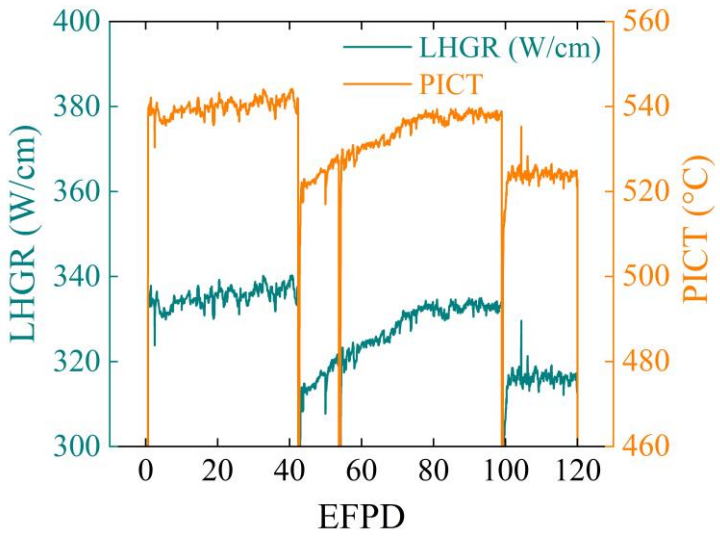

Figure 2. PICT and LHGR for each EFPD for the AFC-3A R4 rodlet.

2.3 Post-irradiation electron microscopy characterization

The electron microscopy characterization of the irradiated fuel was performed at the Electron Microscopy Laboratory (EML) and the Irradiated Materials Characterization Laboratory (IMCL) at Idaho National Laboratory (INL). A JEOL JSM-7000F field emission gun (FEG) scanning electron microscope (SEM) equipped with energy dispersive X-ray spectroscopy (EDS) was used for the initial microstructure characterization. Figure 3 shows the overall microstructure of irradiated annular U-10Zr fuel with HT-9 cladding.

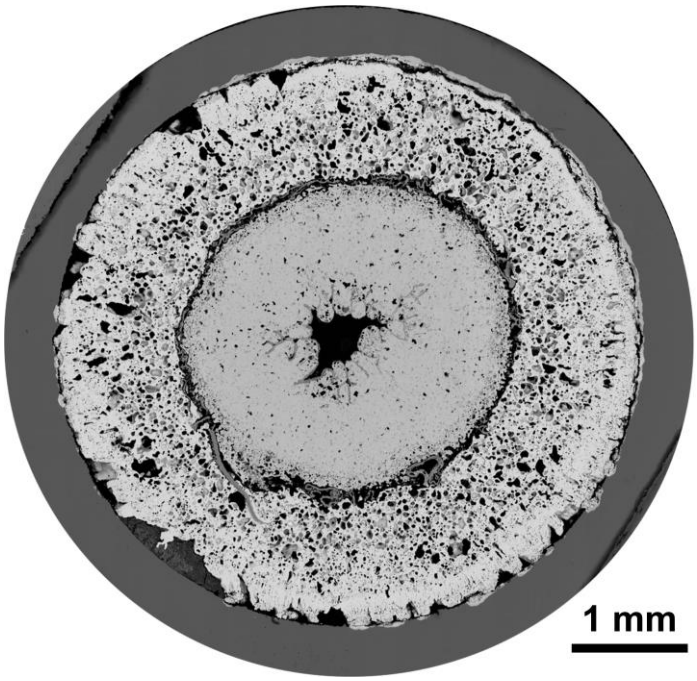

Figure 3. Montage created from a set of SEM images showing the overall microstructure of the irradiated annular U-10Zr fuel.

Following the SEM characterization, a FEI Quanta 3D scanning electron microscope/focused ion beam (SEM/FIB) was used to prepare the transmission electron microscopy (TEM) lamellae. After lift-out, the TEM lamellae were mounted onto Cu grids and thinned to a thickness of ~100 nm using 30 keV Ga ions with decreasing ion beam current. The final thinning current was about 100 pA. To minimize FIB-induced damage, the lamellae were polished by 5 keV Ga ions for ~2 min and 2 keV Ga ions for ~4 min. TEM and scanning transmission electron microscopy with energy dispersive X-ray spectroscopy (STEM-EDS) characterization was carried out on a Thermo Scientific Talos F200X field emission gun (FEG) scanning/transmission electron microscope (S/TEM) equipped with ChemiSTEM™ and operated at 200 kV. STEM-EDS was used for elemental mapping and composition analysis. All EDS quantifications were performed using the Thermo Scientific Velox™ software using the default Brown-Powell ionization cross-section model and multi-polynomial model for background correction. TEM diffraction patterns and STEM-EDS results were used together for phase identification.

3. Results

As shown in Figure 3, the dimensions of the cladding and the outer diameter of the irradiated fuel were similar to the unirradiated condition. However, the originally empty center region of the annular fuel is now filled with a new phase. As discussed in a recent PIE study on the AFC-3 fuels [12], this annular fuel grew inward, and the center region seemed more resistant to oxidation than the outer region, suggesting constituent redistribution and higher Zr concentration in the center region.

To gain insight into the elemental distribution in the irradiated fuel, large area SEM-EDS mapping was performed from the center region of the fuel all the way into the cladding, as shown in Figure 4. The U and Zr distribution show that the fuel region is composed of two different phases: a Zr-rich phase at the center region and a U-rich phase at the outer region. A (Zr, Si)-rich layer was found between these two phases. Chromium was almost exclusively found inside the cladding, indicating no Cr diffusion into the fuel. However, as shown in Figure 4 (d), Fe was found diffused into the fuel. The fuel and the cladding were not

in good contact at the chosen EDS mapping region and almost no U was found in the cladding, as shown in Figure 4 (a). The Zr-rich phase is UZr_2, which will be discussed in a separate study.

The most surprising result shown in Figure 4 is the distribution of neodymium, which is the most representative element of lanthanides. It is obvious that Nd was mostly retained in the Zr-rich phase at the fuel center, as shown in Figure 4 (c). This is very different from the lanthanide behavior in irradiated solid U-Zr fuels in which the lanthanides were mostly found in the FCCI region [13,26,37].

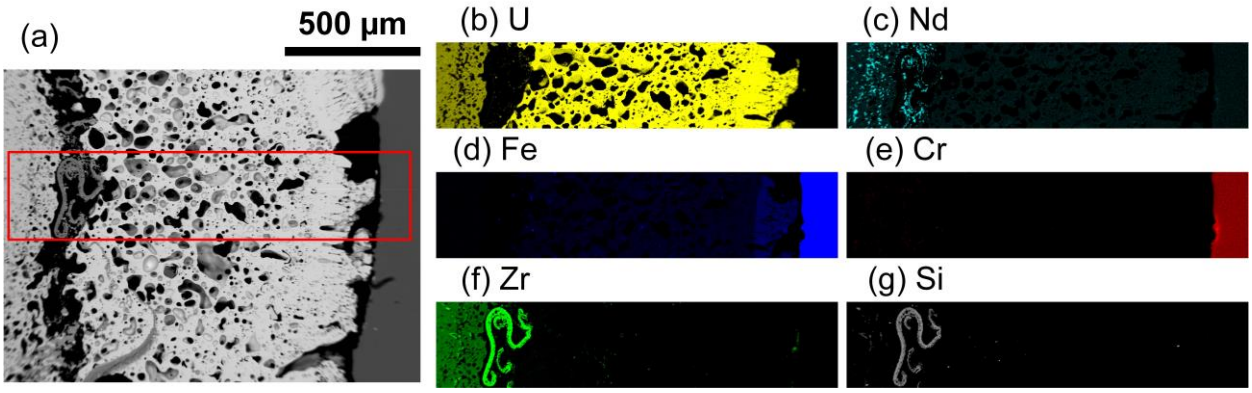

Figure 4. SEM-EDS results showing the overall elemental distribution from the fuel center to the cladding: (a) SEM image, (b)–(g) raw intensity maps of U, Nd, Fe, Cr, Zr, and Si of the region marked by solid red lines in (a).

The fuel came into contact with the cladding and reacted at multiple locations, as shown in Figure 3. To further investigate the detailed microstructure of the FCCI region, two TEM lamellae, lamella #1 and lamella #2, were lifted out from a location that showed good fuel-cladding contact. The SEM images at different magnifications in Figure 5 shows the locations of the TEM lift-outs. As shown in the high-mag SEM image in Figure 5 (d), four distinct areas were identified in the wastage zone inside the cladding: Region I inside the interdiffusion zone, Region II at the interface of the interdiffusion zone and the inner cladding, Region III on the cladding side of the interface, and Region IV from the cladding region. The interdiffusion zone-inner cladding interface is basically composed of two small regions with distinct microstructures: one with a lamellar structure (Region II) and the other (Region III) with two different contrasts (light grey and dark grey). Lamella #1 was lifted out from a region inside the fuel but near the cladding, as shown in Figure 5 (b). Lamella #2 covers all four regions in the wastage zone, as shown in Figure 5 (c)–(d).

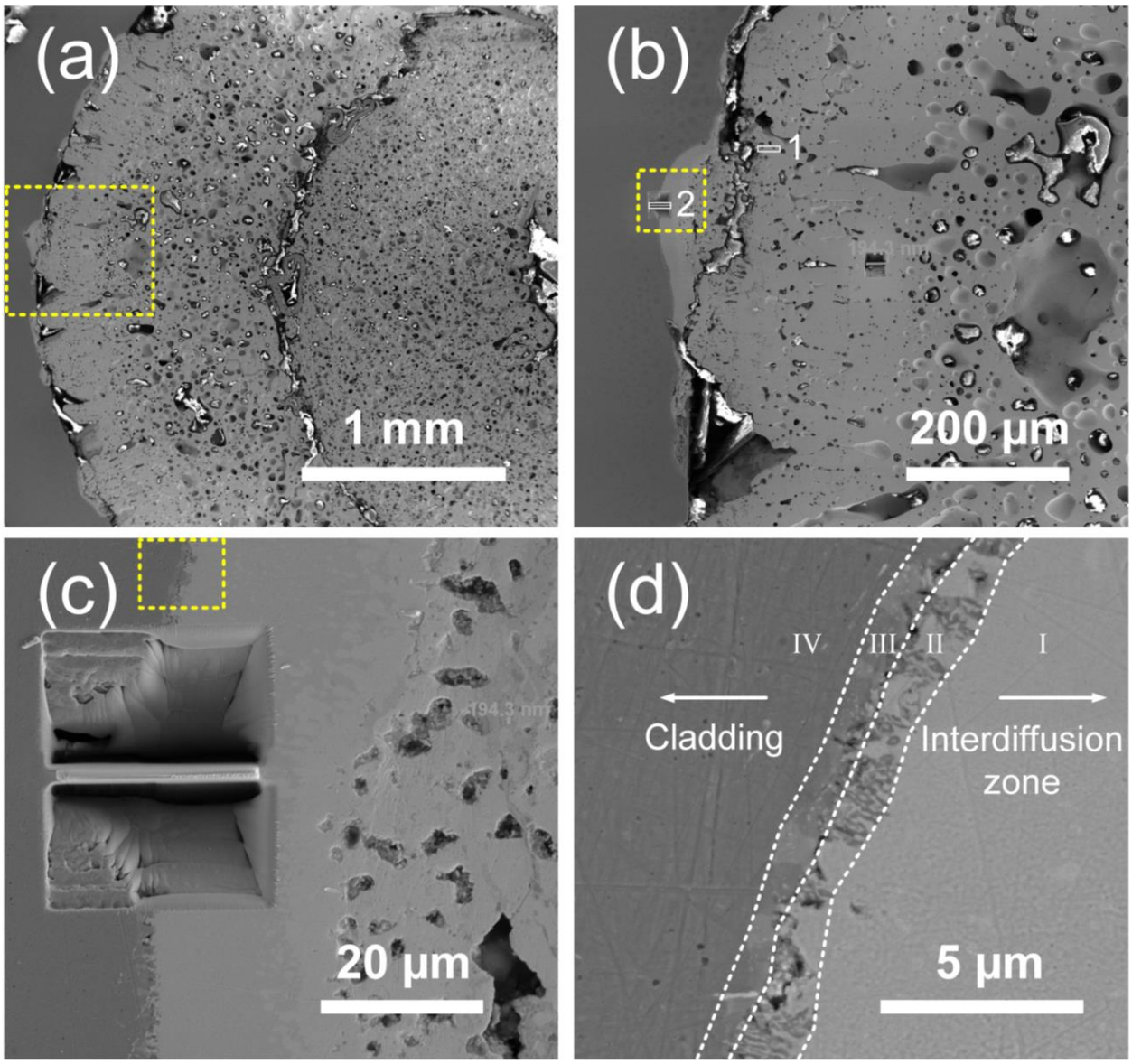

Figure 5. (a)–(d) SEM images at different magnifications showing the microstructure of the FCCI region and the location of the lift-out. Rectangular areas marked by dotted yellow lines indicate the area of the next SEM image. Two lamellae marked as 1 and 2 in (b) were studied in present work.

Before TEM characterization, SEM-EDS mapping was performed at one of the regions that showed good fuel-cladding contact, and an example result is shown in Figure 6. At the fuel-cladding interface, the SEM image and the elemental maps show a lamellar structure similar to the Region II in Figure 5 (d).

It should also be noted that in the SEM images and elemental maps in Figure 6, precipitates which were later confirmed to be U-rich carbides were found at the grain boundaries of the HT-9 grains, as indicated by the red arrows. Most of the precipitates were located inside the light-blue band in Figure 6 (b). A few precipitates were found in the cladding further away from the FCCI interface.

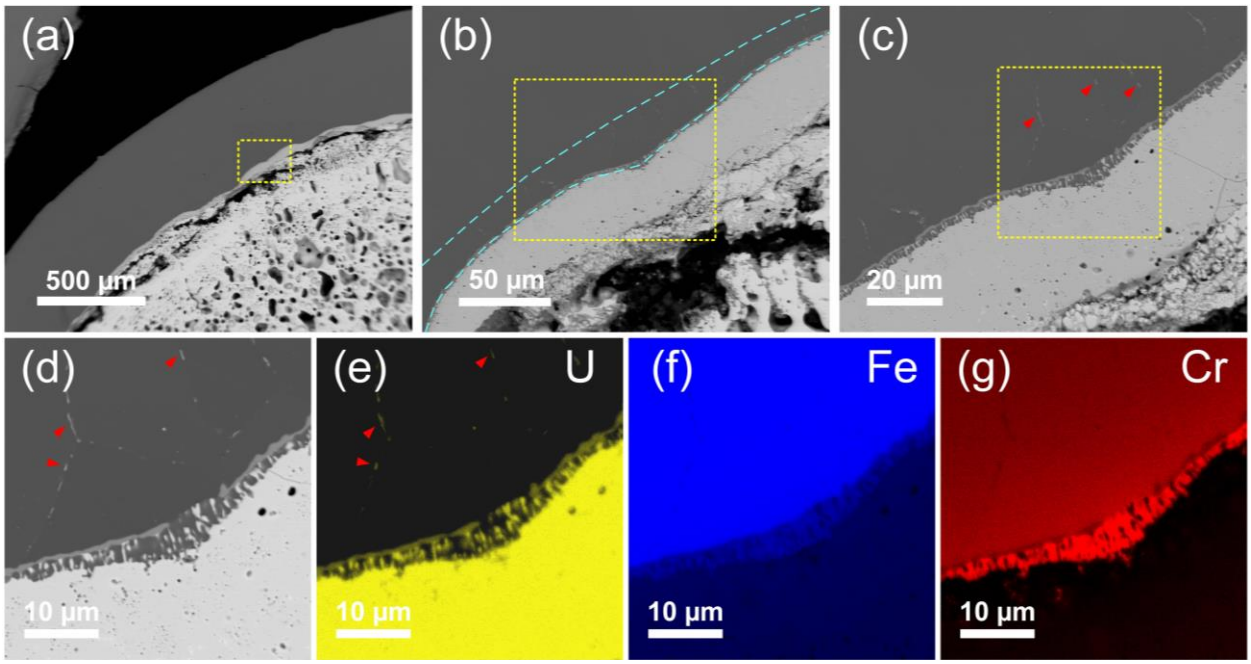

Figure 6. SEM images and EDS mapping showing the microstructure and elemental distribution at the fuel-cladding interface: (a)–(d) SEM images at different magnifications, with the rectangular areas marked by dotted yellow lines indicate the area of the next SEM image; (e)–(g) Elemental maps of U, Fe, and Cr of the region in (d). Red arrows in (c)–(e) indicate the U-rich precipitates at the grain boundaries of HT-9 cladding, and the dashed blue lines indicate the region where the U-rich precipitates were found.

TEM was then used to reveal details of the microstructure near the FCCI region. Figure 7 shows the STEM-EDS results of lamella #1 lifted out near the edge of the fuel. As shown in the elemental maps in Figure 7 (b)–(d), two phases, one Zr-rich and one (U,Fe)-rich, were found in this lamella. The noticeable Fe signal inside lamella #1 suggests the diffusion of Fe into the fuel. The EDS spectra of the (U,Fe)-rich phase and the Zr-rich phase are shown in Figure 7 (e) and (f), respectively. Based on the spectra, the composition of the Zr-rich phase was measured to be ~96 at% Zr and ~2.4 at% U. The composition of the (U,Fe)-rich phase was measured to be ~77 at% U, ~4 at% Zr, and ~14 at% Fe, very close to the composition of the U_6Fe phase identified in previous U-Fe diffusion couple studies [14–21].

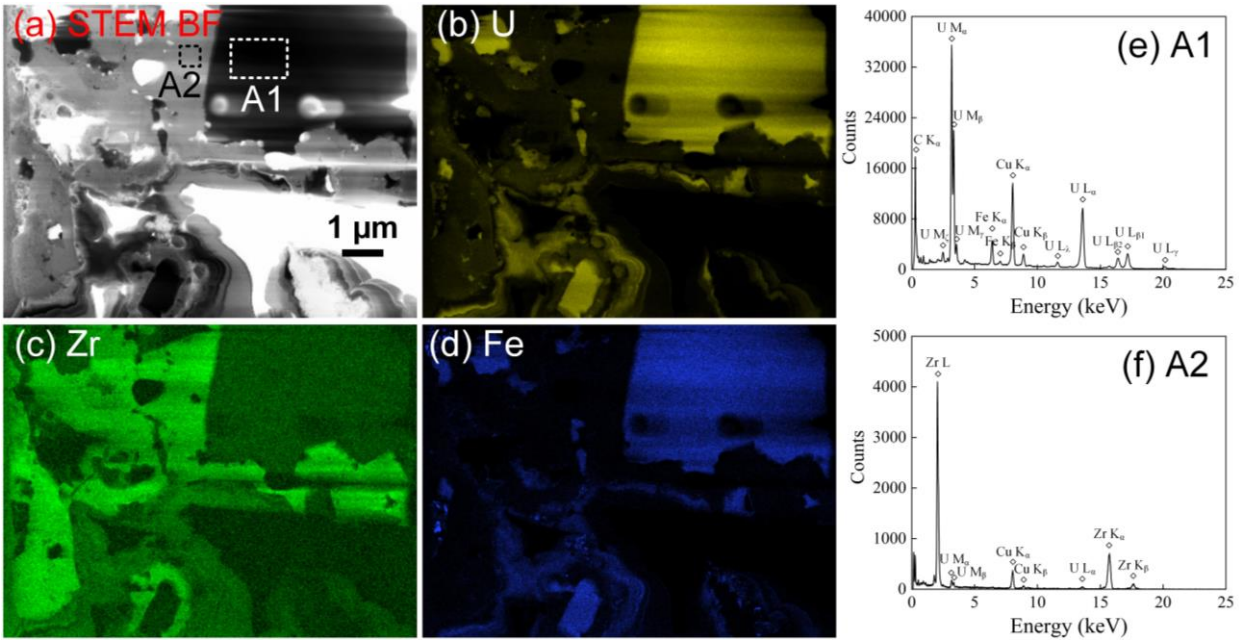

Figure 7. STEM EDS results of lamella #1: (a) STEM bright-field (BF) image, (b)–(d) raw intensity maps of U, Zr, and Fe, (e) EDS spectrum of area A1 marked in (a), (f) EDS spectrum of area A2 marked in (a). The Cu K_α and K_β peaks are background signals from the Cu grid.

To confirm the crystal structure of the (U,Fe)-rich phase, TEM diffraction patterns were acquired, and the results are shown in Figure 8. Indeed all the diffraction patterns from this (U,Fe)-rich phase matched well with the standard tetragonal U_6Fe phase, as shown by the indexed results in Figure 8 (b)–(d). Therefore, the composition and the crytal structure confirms that this (U,Fe)-rich phase is U_6Fe (space group I4/mcm), or more precisely (**U**,Zr)$_6$Fe (bold symbols indicate the dominant elements).

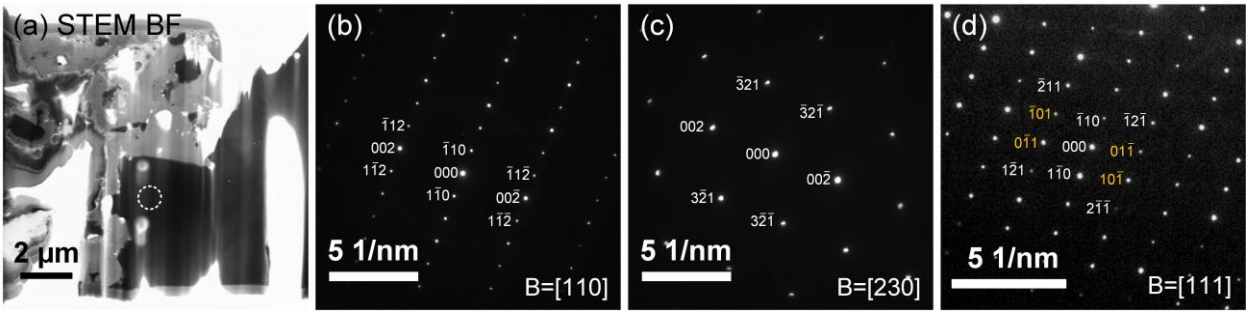

Figure 8. TEM results of the (**U**,Zr)$_6$Fe: (a) STEM BF image, (b)–(d) diffraction patterns of the area marked by dashed white lines in (a), taken at different zones. Yellow labels indicate double diffraction spots.

Lamella #2 was lifted out inside the wastage zone (Figure 5) and has a much more complicated microstructure. Figure 9 displays the overall microstructure of the FCCI region contained in TEM lamella #2. Using the same convention as Figure 5 (d), the lamella can be divided into four regions: Region I inside the interdiffusion zone, Region II and III at the interface of the interdiffusion zone and the inner cladding, and Region IV from the cladding region. Region I is marked by fine grains with a high density of nano-sized voids. Region II contains the lamellar structure. Region III is featured by small grains and fine precipitates. Region IV contains relatively large grains with little voids or porosity. The interface region (Regions II and III) is very porous.

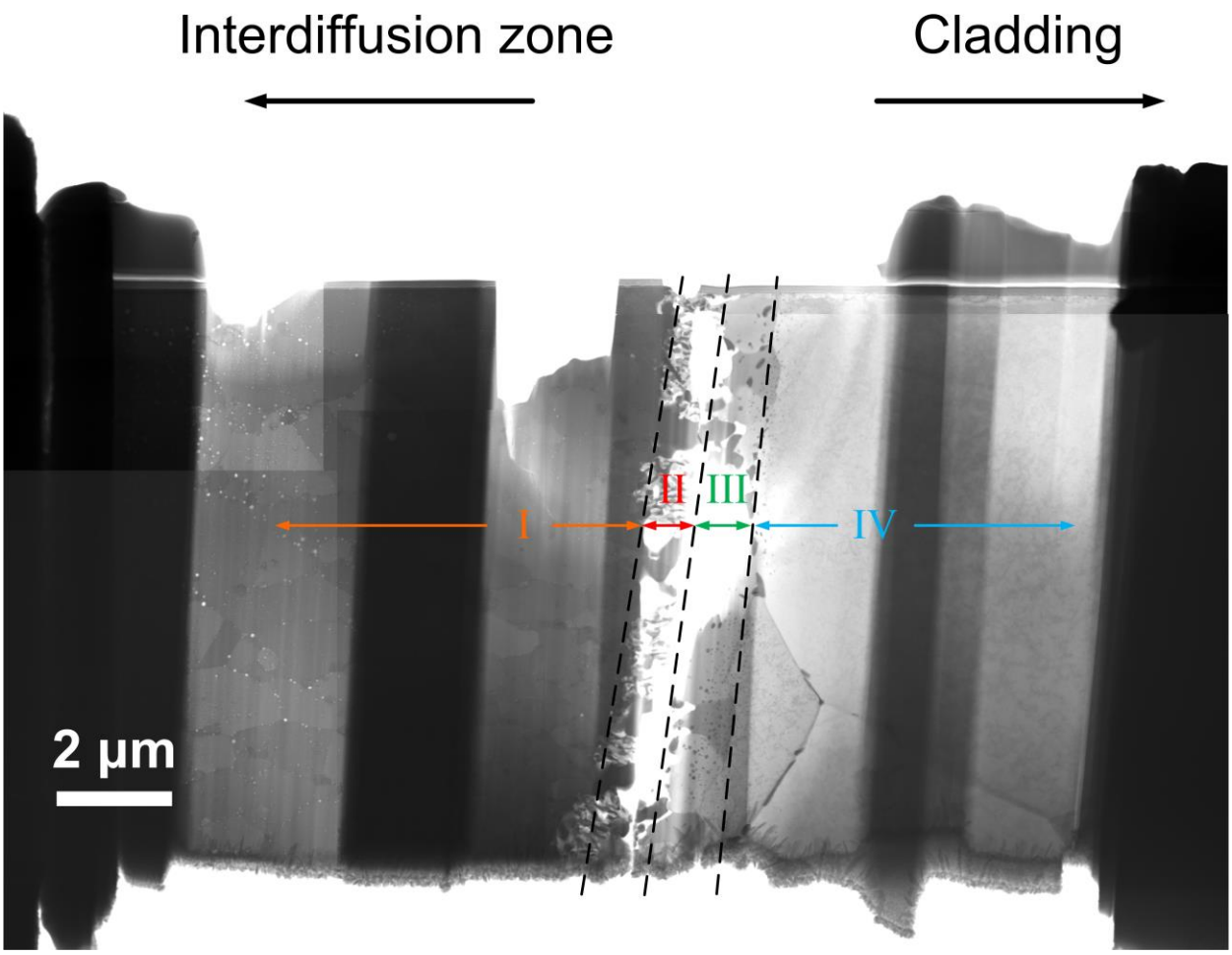

Figure 9. STEM BF image showing the overall microstructure of the FCCI region.

Figure 10 shows the STEM-EDS results of an area inside Region I. The elemental maps show that the matrix of Region I contains U, Fe, and Cr. Uranium carbide precipitates were frequently found in Region I. Figure 10 (g) and (h) also show the EDS spectrum of the uranium carbide (spot 1) and the matrix (spot 2), respectively.

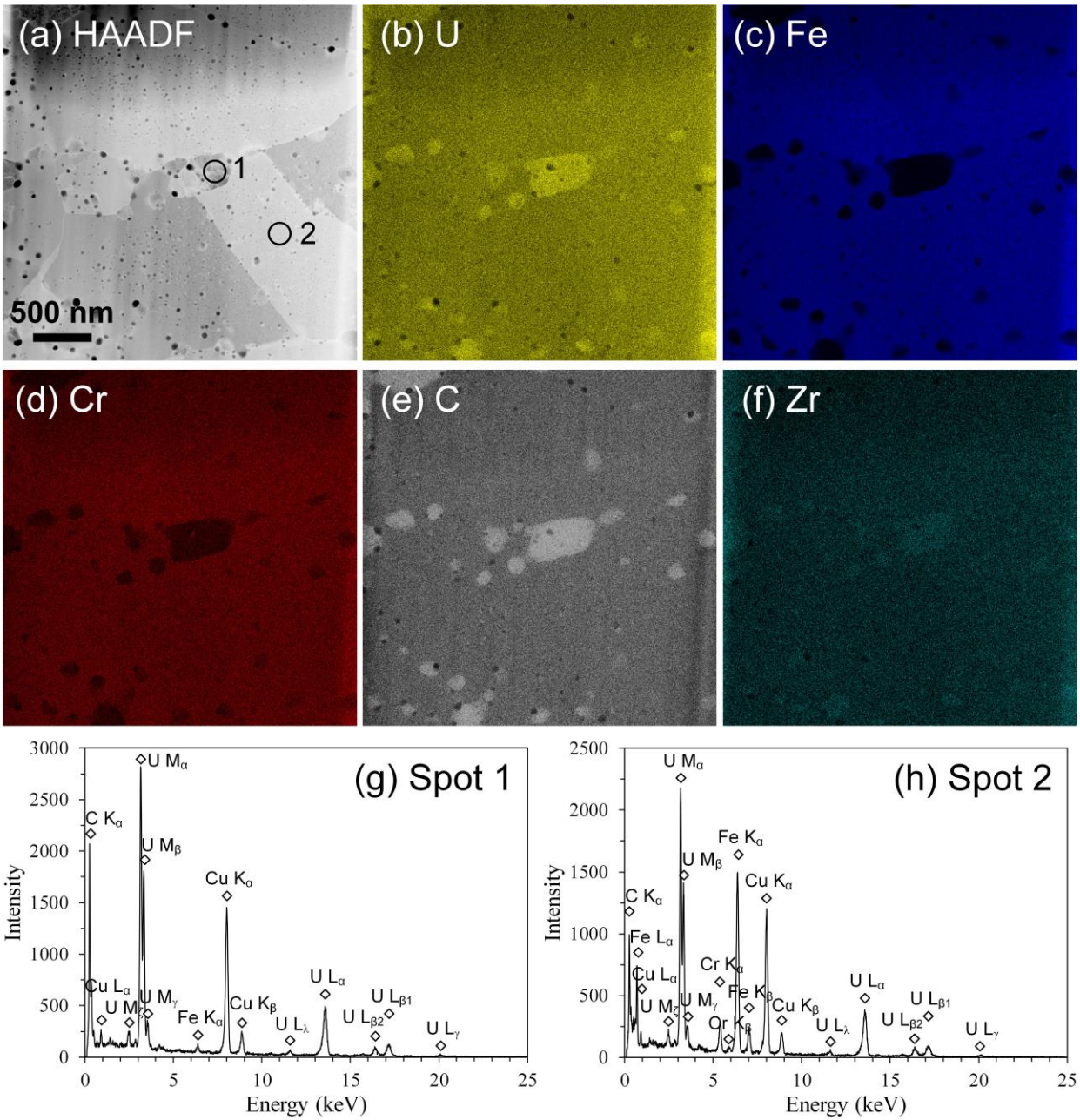

Figure 10. STEM-EDS results of Region I: (a) HAADF image, (b)–(f) raw intensity maps of U, Fe, Cr, C, and W, respectively, (g) EDS spectrum of spot 1 shown in (a), and (h) EDS spectrum of spot 2 shown in (a).

The EDS measurements showed that the matrix in Region I contained about 58.5 at% Fe, 28.1 at% U, 10.0 at% Cr, and 1.2 at% Zr. The (Fe,Cr):(U,Zr) ratio was close to 2:1, which is consistent with the UFe_2 phase. Since U and Fe are the dominant elements, it should be identified as (**U**,Zr)(**Fe**,Cr)$_2$, in which bold symbols indicate the dominant elements.

TEM diffraction patterns were taken to confirm the crystal structure of the matrix in Region I, and the results are shown in Figure 11. Two diffraction patterns (Figure 11 (b) and (c)) were taken and they both matched the UFe_2 phase (space group $Fd\bar{3}m$) perfectly, confirming that the crystal structure of this

(**U**,Zr)(**Fe**,Cr)$_2$ phase is the same as that of the UFe_2 phase that was reported in previous U-Zr and Fe diffusion couple studies [14–16,18–20].

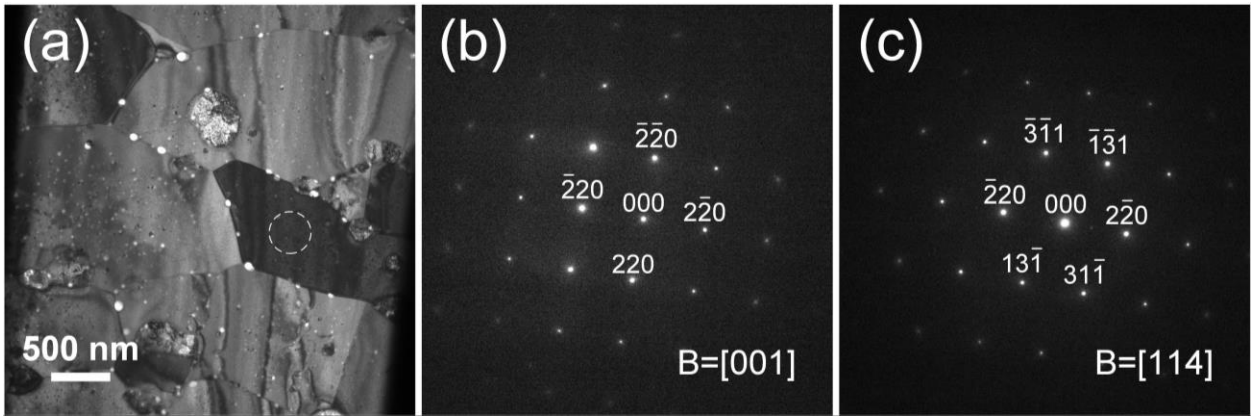

Figure 11. (a) TEM BF image showing the microstructure in Region I, (b) and (c) diffraction patterns taken from the area indicated by the dashed circle in (a).

To confirm the crystal structure of the U-rich carbides in the (**U**,Zr)(**Fe**,Cr)$_2$ phase, TEM diffraction patterns were taken at several different zones. The three diffraction patterns shown in Figure 12 (b)–(d) match perfectly with the [001], [011], and [013] zones of uranium monocarbide (UC) of the NaCl-type crystal structure (space group $Fm\bar{3}m$), respectively. Thus, these U-rich carbides were confirmed to be UC.

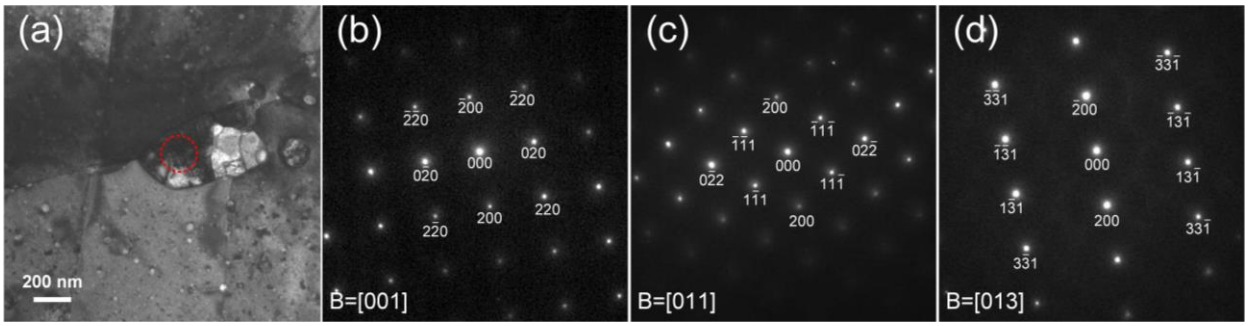

Figure 12. (a) TEM BF image of an intergranular U-rich carbide, (b)–(d) diffraction patterns of the carbide highlighted in (a) at different zone axes. The diffraction patterns confirm the U-rich carbides are uranium monocarbide with a NaCl-type structure.

Details of the microstructure of the (**U**,Zr)(**Fe**,Cr)$_2$ phase are shown in Figure 13. Overall, the (**U**,Zr)(**Fe**,Cr)$_2$ phase contains a high number density of voids, suggesting that this intermetallic phase is prone to irradiation induced swelling. The voids inside grains are generally smaller and some larger voids are located at the interfaces of the uranium carbides. In addition, as shown in the high-mag STEM BF image in Figure 13 (d) and the corresponding elemental maps in Figure 13 (e)–(h), the voids inside the grains are mostly coupled with small uranium carbide precipitates.

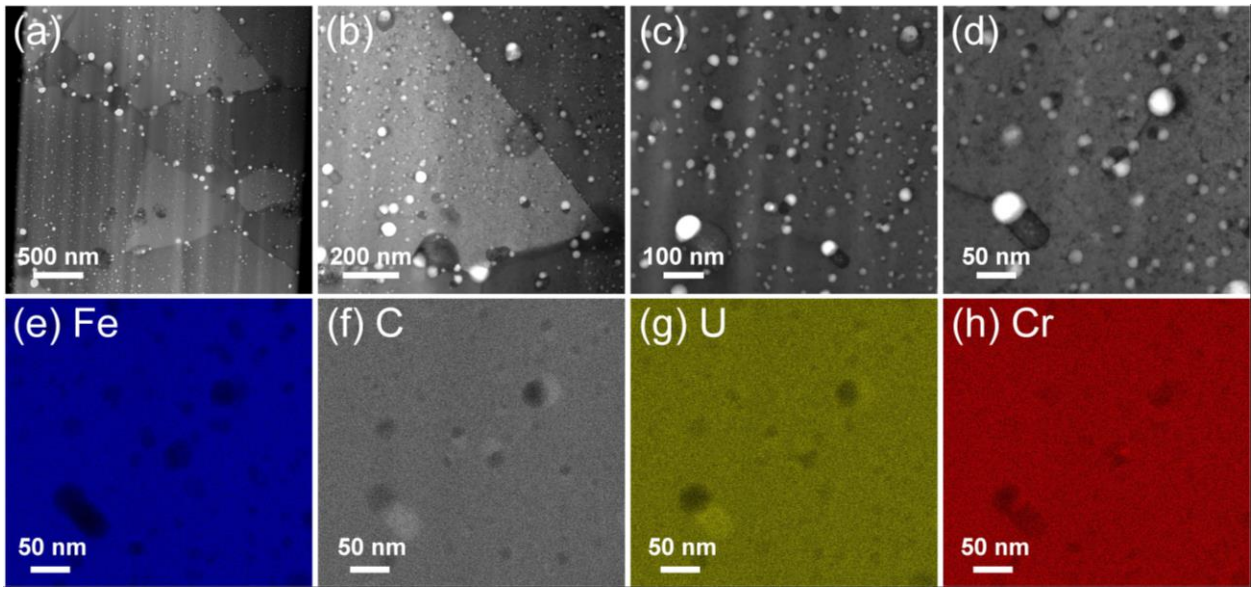

Figure 13. Microstructure of Region I: (a)–(d) STEM BF images of different magnifications, (e)–(h) raw intensity maps of Fe, C, U, and Cr, respectively.

Figure 14. displays the detailed STEM-EDS results of the interaction region. From the high angle annular dark field (HAADF) image in Figure 14 (a) and elemental maps in Figure 14 (b)–(f), it is clear that the interaction region is featured by lamellar structures, uranium carbides, high porosity, and localized distribution of cesium. The lamellar structure is composed of alternating U-rich lamellae and Cr-rich lamellae with a typical width of about 160 nm.

The compositional difference of different regions is more clearly seen in the linescan shown in Figure 14 (g), from which four different regions corresponding to Region I, II, III, and IV are easily identified. From the elemental maps in Figure 14 (b)–(e) show that uranium is mostly found in Region I and Region II, with some U-rich carbides in region III, indicating diffusion of uranium into the cladding. Figure 14 (e) shows that carbon is mostly distributed in Regions I and II, suggesting significant diffusion of carbon into the wastage zone. Figure 14 (d) shows that Regions II and III contain significant amount of chromium, and only limited amount of chromium is found in Region I. It should be noted that some residual cesium was found in Regions II and III, the interface of the interdiffusion zone and the cladding. Since cesium is highly reactive, the actual amount of cesium at the interface before mechanical polishing could be much higher.

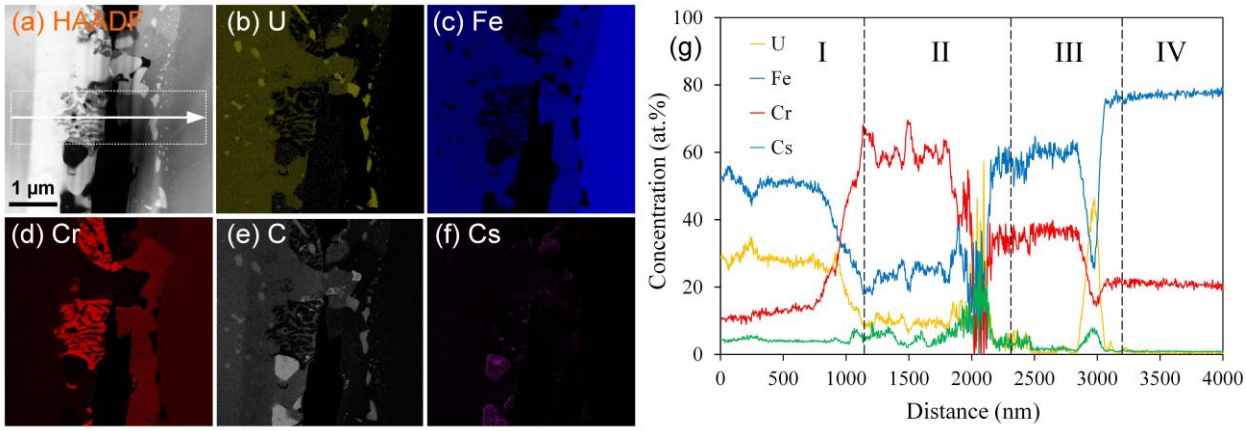

Figure 14. STEM-EDS results of the interaction region: (a) STEM HAADF image, (b)–(f) elemental at.% maps (after quantification) of U, Fe, Cr, C, and Cs, respectively, (g) EDS linescan across the rectangular area marked by dotted white lines in (a).

From the Cr map in Figure 14 (d) and also the EDS linescan in Figure 14 (g), it is apparent that there are noticeable fluctuations in the Cr concentration in both Region II and Region III. The fluctuation in Region II is apparently due to the lamellar structure. A closer look into Region III provides some information as to why Region III is also showing concentration fluctuation. Figure 15 shows higher magnification EDS results focusing on Region III. As shown in Figure 15 (a), areas A1, A2, and A3 are inside Region III, and area A4 is in Region IV. The STEM BF image in Figure 15 (a) and elemental maps in Figure 15 (b)–(i), it show that there are two different phases in Region III: areas A1 and A3 seem to be one phase with higher Cr concentration, whereas area A2 seems to be a different phase with a lower Cr concentration and also contains some amount of U, Si, Ni, Mo, and W. The compositional differences of these two different phases is also seen from the EDS spectra in Figure 15 (j)–(k), and more quantitatively from the EDS linescan across areas A1 and A2 in Figure 15 (m). From the EDS results, it was confirmed that one phase contained almost only Fe (~59.5 at%) and Cr (~30.8 at%), whereas the other phase contained Fe (~64.0 at%), Cr (~16.4 at%), U (~8.2 at%), Si (~2.3 at%), and Mo (~4.1 at.%).

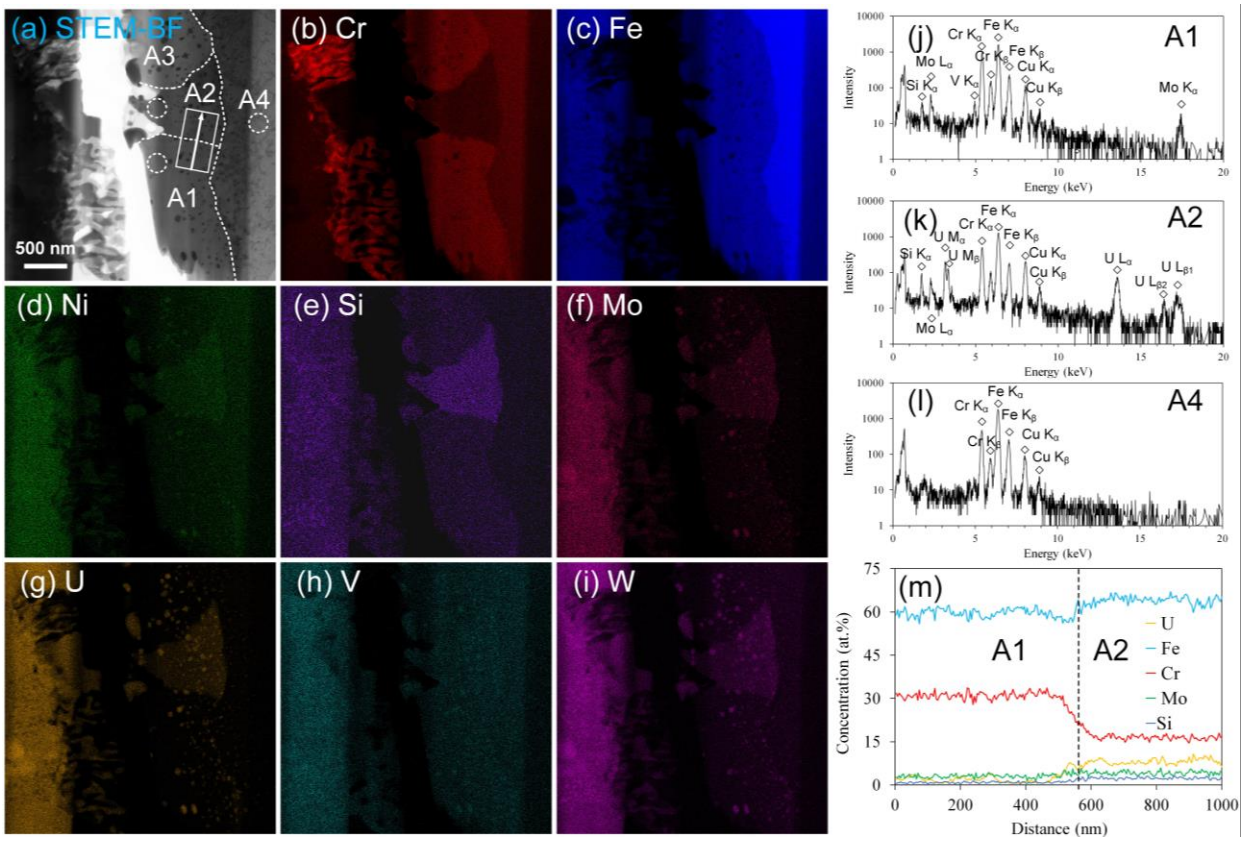

Figure 15. STEM-EDS results of Region III: (a) STEM BF image with four different areas indicated by A1, A2, A3, and A4, (b)–(i) raw intensity maps of Cr, Fe, Ni, Si, Mo, U, V, and W, respectively, (j)–(l) log-scale EDS spectrum corresponding to the areas indicated by dotted circles in A1, A2, and A4, respectively, and (m) EDS linescan from A1 to A2, as indicated by the arrow in (a).

TEM diffraction patterns were then used to identify the crystal structure of the two different phases in Region III, and the results are shown in Figure 16. The diffraction patterns of areas A1 and A3 match well with the binary Fe-Cr σ phase (space group $P4_2/mnm$), as shown by the indexed diffraction patterns of A1

(Figure 16 (b)) and A3 (Figure 16 (g)), respectively. Four diffraction patterns of area A2 were taken, and all four patterns matched well with the quaternary $UCr_{0.1}Fe_{9.9}Si_2$ phase (space group I4/mmm), as shown by the indexed patterns in Figure 16 (c)–(f). In addition, the indexed diffraction pattern of area A4 (Region IV) in Figure 16 (h) confirms that it is the body-centered cubic (BCC) ferrite (α-Fe) phase.

Although the crystal structure of the two phases in Region III was identified, it should be noted that the composition of these two phases differs from those of the standard σ phase and $UCr_{0.1}Fe_{9.9}Si_2$ phase. The σ phase contained only ~30.8 at% Cr and a small amount of Mo. Although there are some discrepancies between calculated Fe-Cr phase diagrams [38–40], the Cr content of the σ phase ranges from ~43% to ~52%, depending on the temperature. The composition of the Fe-Cr-U-Si phase contained less Fe, much more Cr, and much less Si, than the standard $UCr_{0.1}Fe_{9.9}Si_2$ phase.

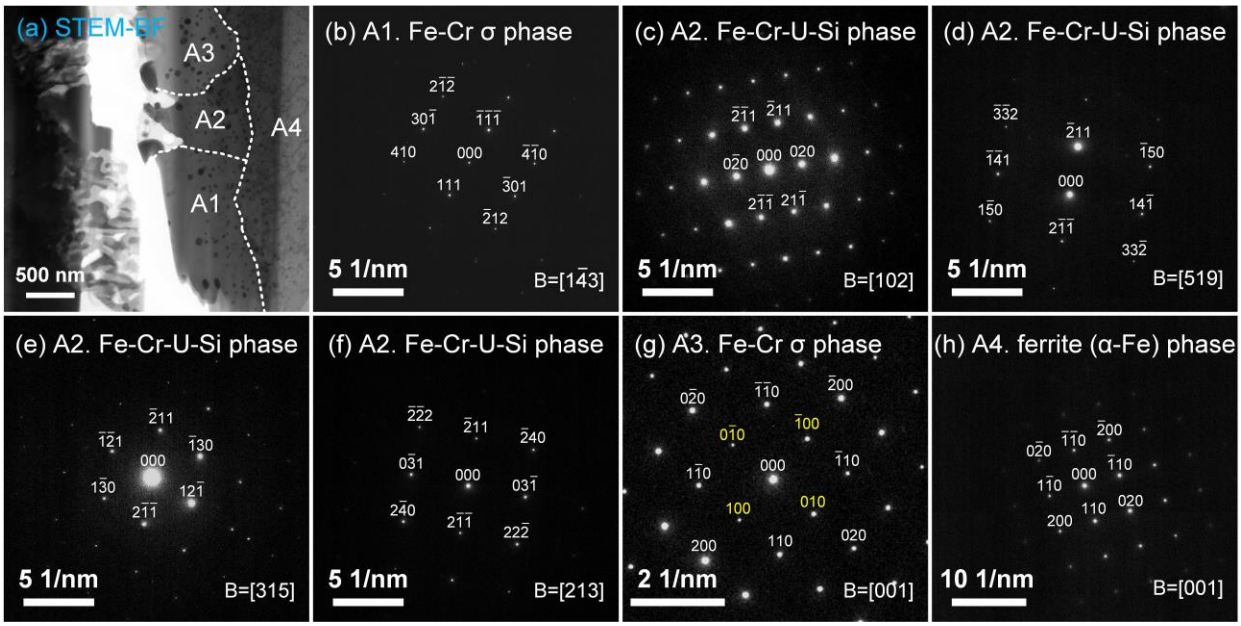

Figure 16. TEM results of the phases in Region III and Region IV: (a) STEM-BF image with areas marked as A1, A2, A3, and A4, (b) diffraction pattern of A1, (c)–(f) diffraction patterns of four different zones of A2, (g) diffraction pattern of A3, and (h) diffraction pattern of A4.

As shown in Figure 16 (h), area A4 in Region IV was identified as the ferrite (α-Fe) phase. However, as displayed in Figure 14 (g), the average Cr concentration of Region IV has increased to ~18 at%, and the average Fe concentration has decreased to ~76 at%, which are significantly different from the composition of unreacted HT-9 (~12.19 at% Cr) before irradiation. The increase in Cr concentration and decrease in Fe concentration in the cladding are apparently the result of the outward diffusion of Fe, as shown by the observed (**U**,Zr)$_6$Fe and (**U**,Zr)(**Fe**,Cr)$_2$ phases. Because of the outward diffusion of Fe, a spatial gradient is expected along the diffusion direction. A closer look at the chemical composition inside the cladding region (Region IV) shows that the Cr and Fe concentrations are indeed not constant but are dependent on the radial location. The results are shown in Figure 17. It is apparent that the Cr content is much higher than ~12.19 at%, and it decreases with increasing distance from the interaction region.

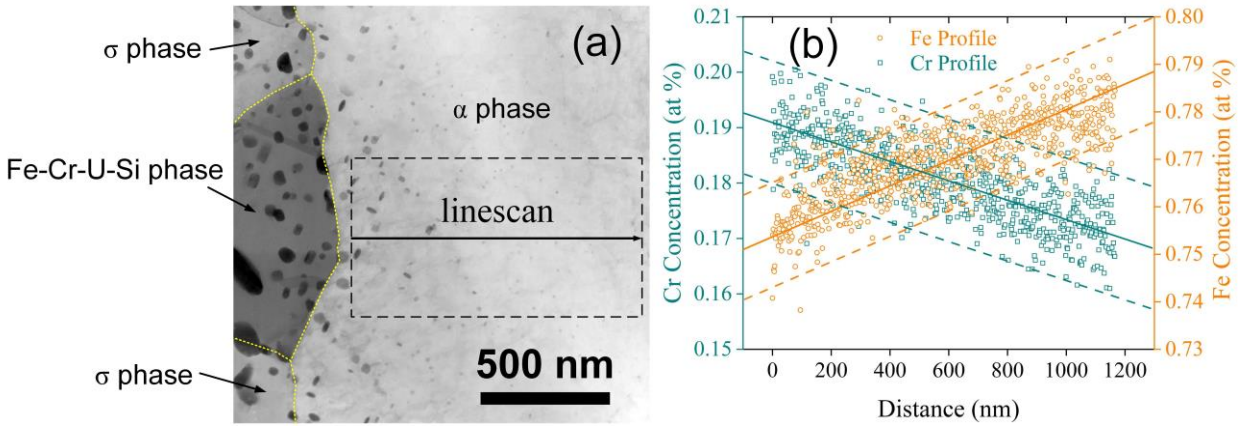

Figure 17. STEM-EDS results of the ferrite (α-Fe) phase: (a) STEM-BF image showing the microstructure of the α-Fe phase, σ phase, and Fe-Cr-U-Si phase, and (b) EDS linescan showing the Fe and Cr profiles. The EDS linescan area is marked by dotted black lines in (a).

HT-9 is a well-known Fe-12Cr ferritic/martensitic steel that has shown excellent swelling resistance in previous irradiation studies. The microstructure of HT-9 is composed of a tempered martensite structure, and the martensite lath is typically several hundred nanometers in width. Both Figure 17 (a) and Region IV in Figure 9 show that the martensite lath structure has disappeared, with only relatively large ferrite (α-Fe) grains in Region IV. This phenomenon can be more clearly seen from the low-mag backscattered electron image in Figure 18, which shows that the grains close to the FCCI region become equiaxed ferrite grains, whereas the grains near the outer surface of the cladding still maintains the martensite lath structure. The equiaxed ferrite grain structure was even found at regions ~200 μm away from the FCCI region.

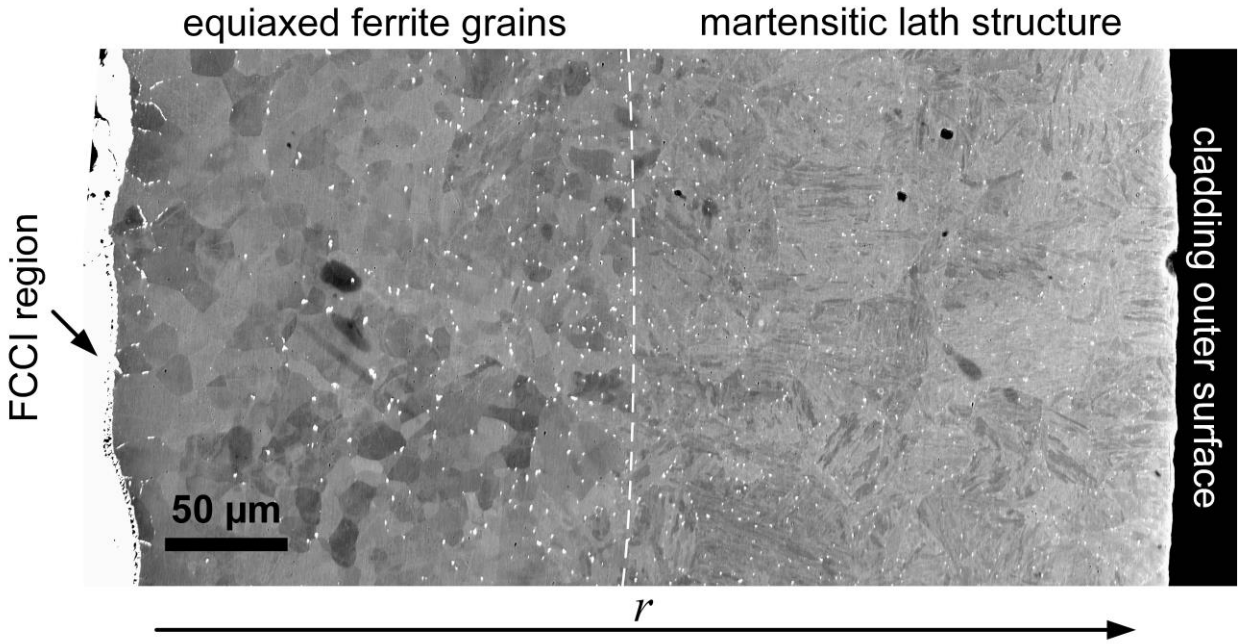

Figure 18. Backscattered electron image showing an overview of the microstructure of the cladding at different radial locations.

The disappearing of the martensite lath structure in the inner region of the cladding is likely due to the diffusion of carbon into the wastage zone, which also resulted in the aforementioned UC precipitates in the (**U**,Zr)(**Fe**,Cr)$_2$ phase. The loss of carbon destabilizes the martensite structure, and ferrite grains are formed instead. The area affected by decarbonization extended much deeper (~200 μm) into the cladding compared with the size of the wastage zone. A similar decarbonization and ferrite formation process in HT-9 cladding after FCCI was mentioned in a previous study [1], in which it was reported that in a solid U-10Zr fuel with HT-9 cladding, a decarbonized zone of ~100 um was developed after 5 at% burnup.

4. Discussions

4.1 Distribution of lanthanides

One of the most unique features of this irradiated U-10Zr fuel is the spatial distribution of the lanthanides. Previous studies [13,31] of solid U-Zr fuel with HT-9 cladding have found significant amount of lanthanides, primarily neodymium and cerium, in the FCCI region at high burnup (> 10 at%). Some low burnup studies [26,37] also confirmed similar behaviors of lanthanides in solid U-Zr fuels. A study [37] of the historical X447 EBR-II experiment indicated that lanthanide fission products were already present in the FCCI region in the DP-69 pin at a local burnup as low as 2.4% FIMA and an average PICT of 667 °C. A recent study of Mechanistic Fuel Failure-3 (MFF-3) experiment showed significant lanthanide distribution in the FCCI region in fuel pin #193045, which has a local burnup of 5.7 % FIMA and an average PICT of 615 °C. Thus, it is believed that the lanthanides in solid U-10Zr fuel can transport and redistribute to the FCCI region even at relatively low burnup. In contrast, almost no lanthanides were found in the FCCI region in this present work. Instead, most lanthanides were found to be retained in the center region, which was identified as single-phase UZr_2 [41]. The biggest difference is that previous studies of lanthanides are from solid U-Zr fuels with sodium bond, whereas only helium was used as the back-fill gas in the annular U-Zr fuel. It is known that the solid-state diffusion of lanthanides is very slow, and the lanthanides observed in the FCCI layer in previous studies were assumed to be driven by liquid-like diffusion [31] through the fuel pores that were partially filled with sodium and cesium, followed by similar liquid-like diffusion through the sodium bond from the fuel surface to the cladding. In the annular fuel, helium gas replaced the liquid sodium bond. Therefore, the liquid-like diffusion through fuel pores and from the fuel surface to the cladding is significantly suppressed. The fact that much less lanthanides were found in helium back-filled annular fuel might indirectly support the liquid-like diffusion mechanism of lanthanides, which has not been determined yet.

The lanthanide behavior in the annular fuel indicates that the annular fuel using helium bond could be a promising alternative fuel form for fast reactor applications. Elimination of sodium can not only provide back-end fuel cycle benefits but also offer an alternative way to mitigate the transport of lanthanides to the FCCI region by suppressing the liquid-like diffusion mechanism. Further irradiation testing is needed to confirm the lanthanide distribution at higher burnups.

4.2 (**U**,Zr)$_6$Fe and (**U**,Zr)(**Fe**,Cr)$_2$ phases due to interdiffusion of uranium and iron

The interdiffusion of U and Fe near the FCCI region formed tetragonal (**U**,Zr)$_6$Fe phase and cubic (**U**,Zr)(**Fe**,Cr)$_2$ phase. The (**U**,Zr)$_6$Fe is located near the edge of the fuel, and the (**U**,Zr)(**Fe**,Cr)$_2$ phase is in the wastage zone inside the cladding. These two phases are similar to those found in previous U-Fe diffusion couple studies [14–21]. However, the microstructure of the irradiated (**U**,Zr)(**Fe**,Cr)$_2$ phase is much more complicated than the pure UFe_2 phase formed in diffusion couple studies. As shown in Figure 13, the (**U**,Zr)(**Fe**,Cr)$_2$ phase contains a high density of voids and intergranular UC precipitates, indicating that the intermetallic (**U**,Zr)(**Fe**,Cr)$_2$ phase is susceptible to void swelling under irradiation and can therefore degrade the mechanical property of the inner cladding region.

4.3 Compositional and microstructural changes in the cladding

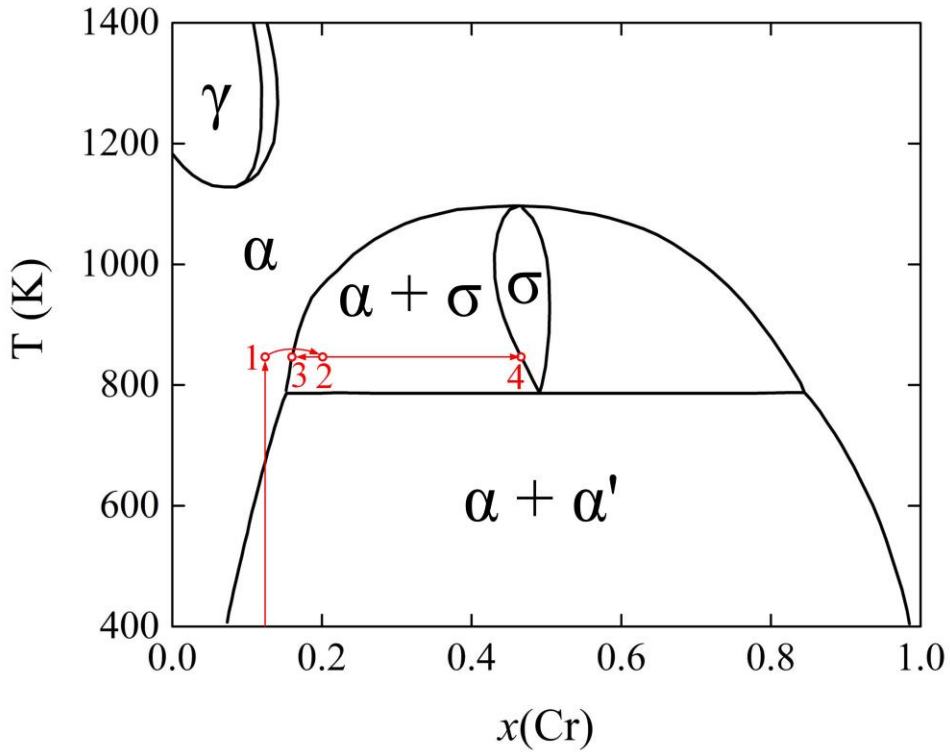

Figure 19. A likely pathway of the observed phase transformation in Region III based on the current Fe-Cr phase diagram [42].

At the cladding side of the interface of the interdiffusion zone and the cladding region (Region III), two different phases were observed: the Fe-Cr σ phase and the tetragonal Fe-Cr-U-Si phase. These two phases are different from the original ferrite/martensite α-Fe phase of HT-9, indicating that phase transformation has occurred at the inner surface of the cladding. Since the unirradiated HT-9 contains only ~12.19 at% Cr, such phase transformation was not expected. A likely pathway for such phase transformation is shown on the Fe-Cr phase diagram [42] in Figure 19. The unirradiated HT-9 contains ~12.19 at% Cr. Therefore, the starting point is somewhere inside the miscibility gap (α+α' region). At the beginning of irradiation, the cladding temperature was raised to ~540 ºC (813 K), and the system was brought to point 1. With increasing burnup, Fe started to diffuse into the fuel, and the Cr content of the most inner region of the cladding started to increase correspondingly. This causes the system to move from point 1 to point 2, passing the α–σ phase boundary. Now the system is thermodynamically favorable to decompose into the σ phase (point 4) and the α phase (point 3). The σ phase is one of the two phases observed in Region III. However, because of the diffusion of uranium into the cladding, the other phase, the α phase, was further transformed to the Fe-Cr-U-Si phase. It should be noted that the compositions of the Fe-Cr σ phase and the tetragonal Fe-Cr-U-Si phase differ from the compositions of the equilibrium σ phase and the standard $UCr_{0.1}Fe_{9.9}Si_2$ phase, respectively. A likely reason is that these two phases were under neutron irradiation and were not at equilibrium. It should also be noted that both phases contain significant amount of uranium carbide precipitates, due to the interdiffusion of U and C.

Two conditions are needed to result in the observed phase transformation: noticeable diffusion of Fe away from the cladding to raise the Cr content and temperature high enough to enter the α+σ region. The brittle σ phase could result in cladding embrittlement. To avoid such phase transformation, the cladding

temperature should be lowered or ways to suppress the outward diffusion of Fe should be identified (e.g., introduce internal sinks into the cladding to suppress radiation-enhanced diffusion).

The outward diffusion of Fe not only resulted in the phase transformation at the inner surface of the cladding, but also raised the Cr content in Region IV inside the cladding. The increase in Cr content moves the system further into the α+α' region at lower temperatures and can potentially induce the formation of the brittle α' phase.

Another consequence of the FCCI is that the martensite lath structure at the inner side of the cladding is gone, possibly due to decarbonization caused by the outward diffusion of C into the wastage zone. The martensite structure is characterized by high densities of dislocations and lath structure. This is different from the α phase shown in Figure 17, indicating that the original martensite has transformed to the ferrite phase. Uranium carbide precipitates were found in the ferrite (α-Fe) grains in Region IV. The carbides appear as small precipitates inside the ferrite grains (Figure 17) and as large precipitates at the ferrite grain boundaries (Figure 6 and Figure 9) and the phase boundaries between Region III and Region IV. The uranium carbide precipitates were only found in the first ~15–30 μm region away from the interface, and the equiaxed ferrite grain structure extended ~200 μm deep into the cladding.

These changes in the composition and microstructure of the region near the FCCI layer in the cladding could adversely affect the local mechanical properties and radiation resistance of the cladding.

5. Conclusions

Annular U-Zr fuel is a promising fuel form due to its back-end fuel cycle benefits. Using advanced electron microscopy and spectroscopy characterization techniques, this study revealed the fuel cladding chemical interaction characteristics of a prototype annular U-10wt%Zr fuel and a Fe-12Cr base HT-9 cladding irradiated to 3.3% FIMA. Unlike the solid U-Zr fuels, most lanthanides were retained in the newly formed UZr_2 phase in the center region of the irradiated annular U-10Zr fuel, suggesting an alternative way to mitigate the transport of lanthanides to the FCCI region. Higher burnup irradiation testing is required to confirm whether the center UZr_2 phase region can still retain the lanthanides at higher burnups.

Based on the microstructure results, the microstructural evolution near the FCCI region of the investigated annular U-10Zr fuel with HT-9 cladding is illustrated in Figure 20.

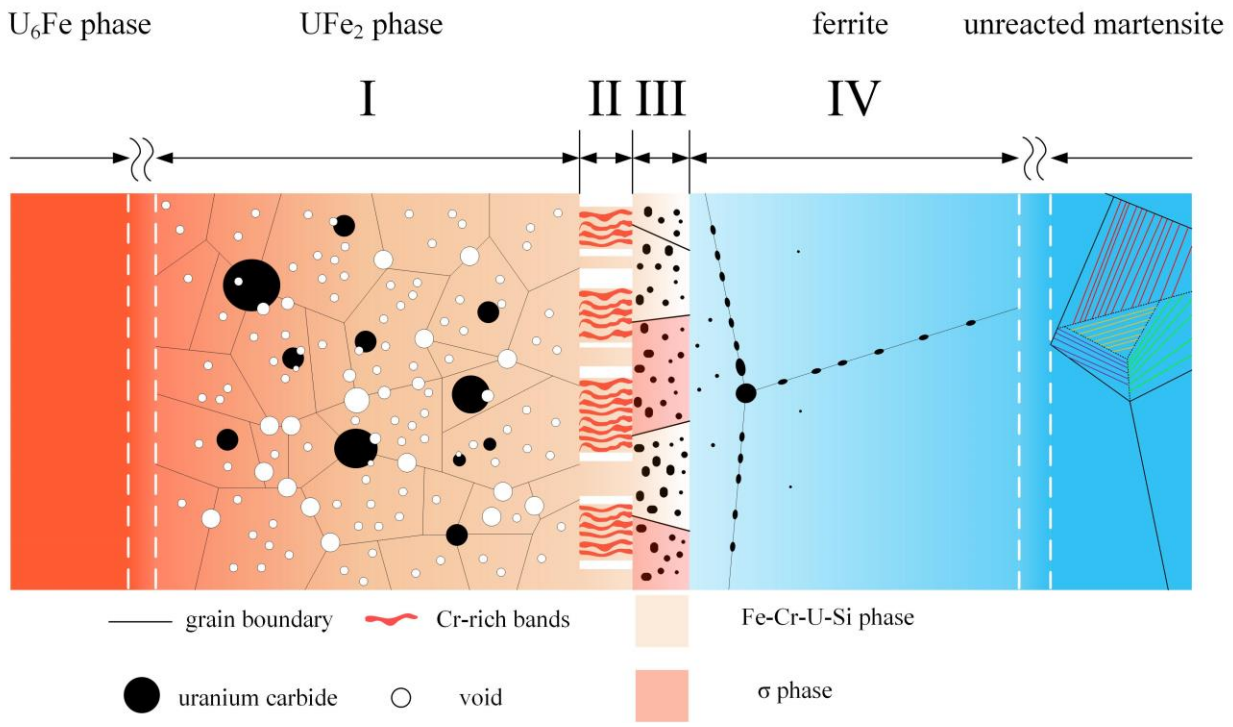

Figure 20. Illustration of the microstructural evolution near the FCCI region.

In the FCCI interdiffusion region, cubic (**U**,Zr)(**Fe**,Cr)$_2$ phase and tetragonal (**U**,Zr)$_6$Fe phase were formed. The (**U**,Zr)(**Fe**,Cr)$_2$ phase contained a significant number of voids and UC precipitates. Most of the voids are spatially associated with the UC precipitates.

At the interface region (Region II and Region III), a lamellar structure was found on the interdiffusion zone side (Region II), and phase transformation was identified on the cladding side (Region III). The lamellar structure is composed of alternating U-rich lamellae and Cr-rich lamellae with a typical width of about 160 nm.

Two phases were identified in Region III: the σ phase and the tetragonal Fe-Cr-U-Si phase. The phase transformation in Region III was explained by a pathway on the Fe-Cr phase diagram. The outward diffusion of Fe (increase in Cr content) and high temperature (e.g., ~540 ºC) are both required to form the σ phase. The Fe-Cr-U-Si phase was formed due to the diffusion of U into the cladding.

In the inner cladding region (Region IV), martensite lath structure was not observed, and large ferrite grains were found, possibly due to the outward diffusion of C. The Cr content of the ferrite grains is much higher (~18 at%) than that of the unirradiated HT-9 (~12.19 at%), and the ferrite grains contain small intragranular uranium carbide precipitates and large intergranular uranium carbide precipitates. Uranium carbide precipitates were found only in the first ~15–30 μm region away from the interface. These microstructural and compositional changes of the cladding could result in local degradation of mechanical properties and radiation resistance.

It should be noted that this prototype annular fuel had imperfect cylindricity, and the actual local cladding temperature varied at different locations depending on the local fuel-cladding gap size. In some locations, the local cladding temperature was much hotter than expected. Significant improvements have been made to the fuel fabrication process and the cylindricity of the of the annular fuels can now be well-controlled, and much less FCCI is expected in these improved fuels.

Acknowledgment

X. Liu acknowledges the financial support from the U.S. Department of Energy, Office of Nuclear Energy under DOE Idaho Operations Office Contract DEAC07-051D14517 as part of a Nuclear Science User Facilities. T. Yao and L. He acknowledge the support from the Center for Thermal Energy Transport under Irradiation, an Energy Frontier Research Center funded by the U.S. Department of Energy, Office of Science, Basic Energy Sciences. This work was supported by the Advanced Fuels Campaign (AFC) of the Nuclear Technology Research and Development (NTRD) program in the U.S. Department of Energy, Office of Nuclear Energy under DOE Idaho Operations Office Contract DE-AC07-05ID14517. Accordingly, the U.S. Government retains and the publisher, by accepting the article for publication, acknowledges that the U.S. Government retains a nonexclusive, paid-up, irrevocable, worldwide license to publish or reproduce the published form of this manuscript or allow others to do so, for U.S. Government purposes.

References

[1] G.L. Hofman, L.C. Walters, T.H. Bauer, Metallic fast reactor fuels, Prog. Nucl. Energy. 31 (1997) 83–110. doi:10.1016/0149-1970(96)00005-4.

[2] W.J. Carmack, D.L. Porter, Y.I. Chang, S.L. Hayes, M.K. Meyer, D.E. Burkes, C.B. Lee, T. Mizuno, F. Delage, J. Somers, Metallic fuels for advanced reactors, J. Nucl. Mater. 392 (2009) 139–150. doi:10.1016/j.jnucmat.2009.03.007.

[3] D.C. Crawford, D.L. Porter, S.L. Hayes, Fuels for sodium-cooled fast reactors: US perspective, J. Nucl. Mater. 371 (2007) 202–231. doi:10.1016/j.jnucmat.2007.05.010.

[4] Y.-I. Chang, TECHNICAL RATIONALE FOR METAL FUEL IN FAST REACTORS, Nucl. Eng. Technol. 39 (2007) 161–170. doi:10.5516/NET.2007.39.3.161.

[5] G.L. Hofman, R.G. Pahl, C.E. Lahm, D.L. Porter, Swelling behavior of U-Pu-Zr fuel, Metall. Trans. A. 21 (1990) 517–528. doi:10.1007/BF02671924.

[6] C.B. Lee, D.H. Kim, Y.H. Jung, Fission gas release and swelling model of metallic fast reactor fuel, J. Nucl. Mater. 288 (2001) 29–42. doi:10.1016/S0022-3115(00)00718-2.

[7] C. Matthews, C. Unal, J. Galloway, D.D. Keiser, S.L. Hayes, Fuel-Cladding Chemical Interaction in U-Pu-Zr Metallic Fuels: A Critical Review, Nucl. Technol. 198 (2017) 231–259. doi:10.1080/00295450.2017.1323535.

[8] D.D. Keiser, Fuel cladding chemical interaction in metallic sodium fast reactor fuels: A historical perspective, J. Nucl. Mater. 514 (2019) 393–398. doi:10.1016/j.jnucmat.2018.09.045.

[9] D.L. Porter, C.B. Hilton, Extending Sodium Fast Reactor Driver Fuel Use to Higher Temperatures, Nucl. Technol. 173 (2011) 218–225. doi:10.13182/NT11-A11551.

[10] S. Hayes, D. Dempsey, J.M. Harp, G.L. Povirk, Developmental Objectives for Advanced Reactor Fuels, Idaho Falls, ID (United States), 2017. doi:10.2172/1599357.

[11] L.R. Blake, Achieving high burn-up in fast reactors, J. Nucl. Energy. Parts A/B. React. Sci. Technol. 14 (1961) 31–48. doi:10.1016/0368-3230(61)90071-4.

[12] J.M. Harp, H.J.M. Chichester, L. Capriotti, Postirradiation examination results of several metallic fuel alloys and forms from low burnup AFC irradiations, J. Nucl. Mater. 509 (2018) 377–391. doi:10.1016/j.jnucmat.2018.07.003.

[13] D.D. Keiser, Fuel-cladding interaction layers in irradiated U-Zr and U-Pu-Zr fuel elements, Argonne, IL (United States), 2006. doi:10.2172/885496.

[14] T. Ogata, M. Kurata, K. Nakamura, A. Itoh, M. Akabori, Reactions between U–Zr alloys and Fe at 923 K, J. Nucl. Mater. 250 (1997) 171–175. doi:10.1016/S0022-3115(97)00262-6.

[15] T. Chen, T.A. Smith, J.G. Gigax, D. Chen, R. Balerio, L. Shao, B.H. Sencer, J.R. Kennedy, Intermetallic formation and interdiffusion in diffusion couples made of uranium and single crystal iron, J. Nucl. Mater. 467 (2015) 82–88. doi:10.1016/j.jnucmat.2015.05.026.

[16] D.D. Keiser, M.A. Dayananda, Interdiffusion between U-Zr fuel vs selected cladding steels, Metall. Mater. Trans. A. 25 (1994) 1649–1653. doi:10.1007/BF02668530.

[17] D.D. Keiser, M.A. Dayananda, Interdiffusion between U-Zr fuel and selected Fe-Ni-Cr alloys, J. Nucl. Mater. 200 (1993) 229–243. doi:10.1016/0022-3115(93)90334-U.

[18] K. Huang, Y. Park, A. Ewh, B.H. Sencer, J.R. Kennedy, K.R. Coffey, Y.H. Sohn, Interdiffusion and reaction between uranium and iron, J. Nucl. Mater. 424 (2012) 82–88. doi:10.1016/j.jnucmat.2012.02.004.

[19] Y. Park, K. Huang, A. Paz y Puente, H.S. LEE, B.H. Sencer, J.R. Kennedy, Y.H. Sohn, Diffusional Interaction Between U-10 wt pct Zr and Fe at 903 K, 923 K, and 953 K (630 °C, 650 °C, and 680 °C), Metall. Mater. Trans. A. 46 (2015) 72–82. doi:10.1007/s11661-014-2277-2.

[20] C.T. Lee, H. Kim, T.K. Kim, C.B. Lee, Diffusion behavior in an interface between U–10Zr alloy and HT-9 steel, J. Nucl. Mater. 395 (2009) 140–144. doi:10.1016/j.jnucmat.2009.10.044.

[21] Y. Xie, M.T. Benson, L. He, J.A. King, R.D. Mariani, D.J. Murray, Diffusion behaviors between metallic fuel alloys with Pd addition and Fe, J. Nucl. Mater. 525 (2019) 111–124. doi:10.1016/j.jnucmat.2019.07.028.

[22] M. Kurata, T. Ogata, K. Nakamura, T. Ogawa, Thermodynamic assessment of the Fe–U, U–Zr and Fe–U–Zr systems, J. Alloys Compd. 271–273 (1998) 636–640. doi:10.1016/S0925-8388(98)00176-5.

[23] T. OGATA, K. NAKAMURA, M. KURATA, T. YOKOO, M.A. MIGNANELLI, Reactions between U-Pu-Zr Alloys and Fe at 923 K, J. Nucl. Sci. Technol. 37 (2000) 244–252. doi:10.1080/18811248.2000.9714890.

[24] M. Kurata, K. Nakamura, T. Ogata, Thermodynamic evaluation of the quaternary U–Pu–Zr–Fe system – assessment of cladding temperature limits of metallic fuel in a fast reactor, J. Nucl. Mater. 294 (2001) 123–129. doi:10.1016/S0022-3115(01)00473-1.

[25] J.M. Harp, L. Capriotti, D.L. Porter, J.I. Cole, U-10Zr and U-5Fs: Fuel/cladding chemical

interaction behavior differences, J. Nucl. Mater. 528 (2020) 151840. doi:10.1016/j.jnucmat.2019.151840.

[26] J.M. Harp, D.L. Porter, B.D. Miller, T.L. Trowbridge, W.J. Carmack, Scanning electron microscopy examination of a Fast Flux Test Facility irradiated U-10Zr fuel cross section clad with HT-9, J. Nucl. Mater. 494 (2017) 227–239. doi:10.1016/j.jnucmat.2017.07.040.

[27] A.E. Bridges, A.E. Waltar, R.D. Leggett, R.B. Baker, J.L. Ethridge, A Liquid-Metal Reactor Core Demonstration Experiment Using HT-9, Nucl. Technol. 102 (1993) 353–366. doi:10.13182/NT93-A17034.

[28] R.G. Pahl, D.L. Porter, C.E. Lahm, G.L. Hofman, Experimental studies of U-Pu-Zr fast reactor fuel pins in the experimental breeder reactor-ll, Metall. Trans. A. 21 (1990) 1863–1870. doi:10.1007/BF02647233.

[29] L.. Walters, Thirty years of fuels and materials information from EBR-II, J. Nucl. Mater. 270 (1999) 39–48. doi:10.1016/S0022-3115(98)00760-0.

[30] A.B. Cohen, H. Tsai, L.A. Neimark, Fuel/cladding compatibility in U-19Pu-10Zr/HT9-clad fuel at elevated temperatures, J. Nucl. Mater. 204 (1993) 244–251. doi:10.1016/0022-3115(93)90223-L.

[31] R.D. Mariani, D.L. Porter, T.P. O'Holleran, S.L. Hayes, J.R. Kennedy, Lanthanides in metallic nuclear fuels: Their behavior and methods for their control, J. Nucl. Mater. 419 (2011) 263–271. doi:10.1016/j.jnucmat.2011.08.036.

[32] R.S. Fielding, P.A. Hansen, T.A. Hyde, J. Maupin, Fabrication Report for the FY11 Phases of the AFC-3A and 3B Irradiation Experiments, Idaho Natl. Lab. Rep. (2011) INL/LTD-11-23158.

[33] T.P. O'Holleran, C.A. Papesch, L.N. Squires, T.A. Hyde, J.R. Kennedy, T. Hartmann, AFC-3 Fuel Characterization, Idaho Natl. Lab. Rep. (2012) INL/LTD-12-24346.

[34] G.S. Chang, R.G. Ambrosek, Hardening neutron spectrum for advanced actinide transmutation experiments in the ATR, Radiat. Prot. Dosimetry. 115 (2005) 63–68. doi:10.1093/rpd/nci167.

[35] J.M. Harp, S.L. Hayes, P.G. Medvedev, D.L. Porter, L. Capriotti, Testing Fast Reactor Fuels in a Thermal Reactor: A Comparison Report, Idaho Natl. Lab. Rep. (2017) INL/EXT-17-41677. doi:10.2172/1458766.

[36] P. Medvedev, S. Hayes, S. Bays, S. Novascone, L. Capriotti, Testing fast reactor fuels in a thermal reactor, Nucl. Eng. Des. 328 (2018) 154–160. doi:10.1016/j.nucengdes.2017.12.034.

[37] William J. Carmack, Temperature and Burnup Correlated FCCI in U-10Zr Metallic Fuel, 2012. doi:10.2172/1055966.

[38] J.-O. Andersson, B. Sundman, Thermodynamic properties of the Cr-Fe system, Calphad. 11 (1987) 83–92. doi:10.1016/0364-5916(87)90021-6.

[39] W. Xiong, M. Selleby, Q. Chen, J. Odqvist, Y. Du, Phase Equilibria and Thermodynamic Properties in the Fe-Cr System, Crit. Rev. Solid State Mater. Sci. 35 (2010) 125–152. doi:10.1080/10408431003788472.

[40] A. Jacob, E. Povoden-Karadeniz, E. Kozeschnik, Revised thermodynamic description of the Fe-Cr system based on an improved sublattice model of the σ phase, Calphad. 60 (2018) 16–28. doi:10.1016/j.calphad.2017.10.002.

[41] T. Yao, unpublished work, (n.d.).

[42] W. Xiong, P. Hedström, M. Selleby, J. Odqvist, M. Thuvander, Q. Chen, An improved thermodynamic modeling of the Fe–Cr system down to zero kelvin coupled with key experiments, Calphad. 35 (2011) 355–366. doi:10.1016/j.calphad.2011.05.002.

Fuel-cladding chemical interaction of a prototype annular U-10Zr fuel with Fe-12Cr ferritic/martensitic HT-9 cladding

Xiang Liu[a,*], Luca Capriotti[a,*], Tiankai Yao[a,*], Jason M. Harp[b], Michael T. Benson[a], Yachun Wang[a], Fei Teng[a], Lingfeng He[a]

[a]*Idaho National Laboratory, Idaho Falls, ID 83415, USA*
[b]*Oak Ridge National Laboratory, Oak Ridge, TN 37831, USA*

[*]Corresponding authors
Email addresses: Xiang.liu@inl.gov (X.Liu), Luca.Capriotti@inl.gov (L. Capriotti), tiankai.yao@inl.gov (T. Yao)

Abstract

Solid metallic fuels have been traditionally used in sodium-cooled fast reactors. However, the sodium bond used in solid fuels complicates the fuel fabrication and back-end fuel cycle processes. As an alternative fuel form, the annular metallic fuel design with helium bond is being investigated to eliminates the liquid sodium bond between the fuel and the cladding. The fuel-cladding chemical interaction (FCCI) of annular fuel also presents features different from sodium bonded solid fuel. Here, state-of-the-art electron microscopy and spectroscopy techniques were used to study the FCCI of a prototype annular U-10wt%Zr (U-10Zr) fuel with ferritic/martensitic HT-9 cladding irradiated to 3.3% fission per initial heavy atom. Compared with sodium-bonded solid fuels, negligible amounts of lanthanides were found in the FCCI layer in the investigated helium-bonded annular fuel. Instead, most lanthanides were retained in the Zr-rich phase in the fuel center region. The interdiffusion of iron and uranium resulted in tetragonal (**U**,Zr)$_6$Fe phase (space group I4/mcm) and cubic (**U**,Zr)(**Fe**,Cr)$_2$ phase (space group Fd$\bar{3}$m). The (**U**,Zr)(**Fe**,Cr)$_2$ phase contains a high density of voids and intergranular uranium monocarbides of NaCl-type crystal structure (space group Fm$\bar{3}$m). At the interdiffusion zone and inner cladding interface, a porous lamellar structure composed of alternating Cr-rich layers and U-rich layers was observed. Next to the lamellar region, unexpected phase transformation from body-centered cubic ferrite (α-Fe) to tetragonal binary Fe-Cr σ phase (space group P4$_2$/mnm) occurred, and tetragonal Fe-Cr-U-Si phase (space group I4/mmm) was identified. Due to the diffusion of carbon into the interdiffusion zone, carbon depletion inside the HT-9 led to the disappearance of the martensite lath structure, and intergranular U-rich carbides formed as a result of the diffusion of uranium into the cladding. These findings reveal the unique FCCI behavior of annular U-Zr fuels, which could be a promising alternative fuel form for high burnup fast reactor applications.

Keywords: Fuel-cladding chemical interaction (FCCI); metallic fuel; advanced nuclear fuel; transmission electron microscopy (TEM); HT-9 cladding; phase transformation.

---

1. Introduction

Sodium-cooled fast reactors (SFR) is one of the advanced reactor designs that have been successfully built and operated globally [1]. One goal of current SFR fuel design is to develop technologies that enable the expanded deployment of SFR technology for different applications. Three possible applications of SFR

technology are actinide management, process heat, and once-through fuel for power or test reactor applications [2].

Metallic U-Zr alloy fuels are candidate fuel types for SFR [3–6]. Irradiation-induced swelling [7], fission gas release [8], and fuel-cladding chemical interaction (FCCI) [9,10] are key limiting factors that restrict fuel performance at high burnup. Historically, SFR fuel designs were adapted to mitigate the challenges posed by swelling and fission gas release. A low smear density was employed to accommodate the rapid swelling and avoid premature mechanical failure of the cladding. A relatively large volume gas plenum was used to accommodate the released fission gas. Limitations on the peak inner cladding temperature of fuel pins below 625 °C were historically used to mitigate FCCI. However, this limited the maximum outlet temperature of SFR to between 500–550 °C, which excludes SFR use from many potential process heat applications [11]. Annular metallic fuel that is sodium free is an exemplary technology that can help enable once-through fuel scenarios.

Swelling in metallic fuel can be accommodated in many ways [12]. Most often, it was accommodated by placing a solid fuel into a larger cladding tube and filling the space between with a high thermal conductivity liquid, like sodium. However, sodium-bonded spent fuels are considered mixed hazardous waste in a once-through fuel cycle and require a costly sodium removal process prior to disposal [13]. As a possible alternative to the historical solid U-Zr fuels, annular U-Zr fuels are being evaluated. In the annular U-Zr fuel design shown in Figure 1, the small gap between the fuel and the cladding allows helium to be used as the bonding material, eliminating the hazards associated with sodium. However, because of the differences in bonding material and fuel design, the FCCI behavior of these annular U-Zr fuels could be very different from historical solid U-Zr fuels.

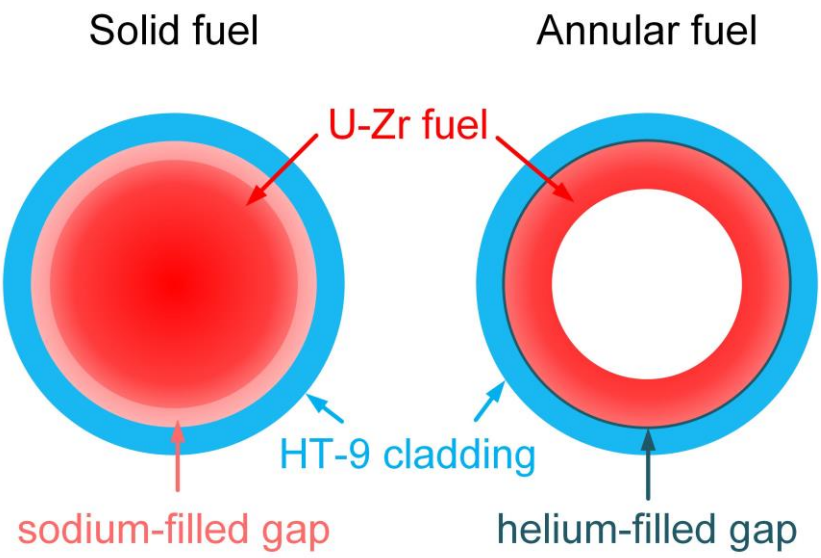

Figure 1. Illustration of the differences in the design of sodium-bonded solid fuel versus helium-bonded annular fuel.

Metallic fuel FCCI can involve both fission products interaction with cladding and interaction between the primary fuel elements and the cladding. On one hand, as the lanthanide fission products diffuse down the thermal gradient and interact with cladding constituents, a brittle wastage zone along the inner surface of the cladding is formed [14]. This wastage zone poses threats to the mechanical integrity of the cladding. On the other hand, the diffusion of iron into the fuel can form low melting eutectic phases and potentially

lead to fuel melting. For instance, two representative phases found in U-Zr fuel with Fe base cladding interdiffusion studies [15–22] are U_6Fe and UFe_2, the melting points of which are ~1102 K and ~1504 K, respectively [23]. The melting point can be further lowered by the addition of plutonium in U-Pu-Zr fuels [24,25]. Direct interaction between cladding elements and fuel was also observed in the irradiation experience of U-5Fs alloys [26].

Previous studies found that Zr-rich regions (Zr-rind) at the fuel periphery could act as diffusion barriers to reduce FCCI, and the Zr-rind was assumed to be a result of impurities during fuel fabrication [9]. Zr liners were then proposed as one approach to mitigate FCCI.

The vast majority of existing irradiated metallic alloy fuel pins from past U.S. fast reactor fuel research programs were composed of U-10wt% Zr (U-10Zr) fuel sodium bonded to HT-9 cladding with a smear density of ~75% [5,27] to accommodate fuel swelling. The liquid sodium bond was chosen to ensure efficient heat transfer from the fuel to the cladding. HT-9 is a Fe-12Cr base ferritic/martensitic alloy that shows excellent swelling resistance and compatibility with metallic fuels [28–30]. The FCCI of HT-9 cladding with U-Zr and U-Pu-Zr fuels were investigated in previous scanning electron microscopy (SEM) [14,27,31] and electron micro probe analyzer (EPMA) [14] studies, and it was found that lanthanides penetrated into the cladding and iron diffused into the fuel. Previous studies [9,32] also proposed that the transport of lanthanides could be through liquid-like diffusion via interconnected pores filled with sodium and cesium. The liquid sodium bond used in historical solid U-Zr fuels might have played an important role in the transportation of lanthanides to the FCCI region.

In this study, the FCCI behavior of an sodium-free helium-bonded annular U-10Zr fuel with HT-9 cladding was investigated in detail for the first time, utilizing the recently available advanced electron microscopy and spectroscopy capabilities for highly radioactive samples at the Materials and Fuels Complex (MFC), Idaho National Laboratory (INL). The results shed light on the unique FCCI behavior of annular U-10Zr fuel, which could be a promising fuel type for SFR applications.

2. Experimental

2.1 Materials

The investigated fuel is an annular U-10Zr fuel from the Advanced Fuels Campaign (AFC) series (AFC-3A) of irradiation experiments. As part of the AFC-3A irradiation, this fuel rodlet was designated AFC-3A R4, and the corresponding fuel fabrication was described in Fielding *et al.* [33], and pre-irradiation characterization was reported in O'Holleran *et al.* [34]. Post-irradiation examination (PIE) data and the overall irradiation performance of AFC-3A and AFC-3B fuels were discussed in a recent study [13].

The AFC-3A R4 fuel rodlet has a nominal composition of U-10wt%Zr. The rodlet is in the annular fuel form with an inner diameter of 3.25 mm, an outer diameter of 4.86 mm, and a total height of 38.0 mm. The nominal smear density is 55%, and the as-fabricated smear density is 53.8%. Helium was used as the bonding material. The fuel alloy was fabricated by mixing uranium and zirconium metals in an arc melter and homogenized through several melts, followed by injection casting into a quartz mold with an inner quartz core. After casting, the inner quartz core was removed by drilling, and the outside mold was removed by breaking the quartz off the outside of the cast pin. The fuel slug was then cut into the desired length for irradiation testing. Some fabrication imperfections were observed for this annular U-10Zr fuel pin. Specifically, an oversized inner capsule tube diminishes the fuel outer diameter and leads to a generally large fuel cladding gap (> 50 μm) prior to irradiation. A lack of final machining step causes rough surfaces and localized contact between fuel and cladding during irradiation. Furthermore, the capsule tube inner

diameter was not concentric with the outer diameter due to poor cylindricity, which led to circumferential variations of the fuel pin.

2.2 Neutron irradiation

The as-fabricated annular U-10Zr fuel was sealed inside ferritic/martensitic steel HT-9. The cladding had an outer diameter of 5.842 mm and a wall thickness of 0.4445 mm. The HT-9 steel used in this work was from legacy EBR-II cladding. Although the heat treatment information for this specific cladding tube was not available, information from similar EBR-II Mark-IV driver fuel HT-9 cladding show that these cladding tubes met the grade UNS Designation S42100 and ASTM A771–83 requirements. All the HT-9 cladding tubes were manufactured by the Carpenter Technology Corporation. The HT-9 tubes were cold drawn 20±5 %, followed by adequate annealing at 2035 ºF (1113 ºC) and tempering at 1200–1300 ºF for two hours and rapid cooling. The final tempered martensitic microstructure has an ASTM grain size number of 7–9. The nominal chemical composition of the HT-9 cladding tube is listed in Table 1.

Table 1. Nominal chemical composition of the HT-9 cladding tube.

Element	Fe	C	Mn	P	S	Si	Ni	Cr	Mo	Cu	V	Co	W
wt%	Bal.	0.22	0.56	0.13	0.002	0.30	0.57	11.53	1.08	0.02	0.31	0.02	0.52
at%	Bal.	1.007	0.56	0.23	0.003	0.587	0.534	12.19	0.619	0.017	0.335	0.0187	0.1555

The rodlet was sealed inside a cylindrical capsule container that served as the primary boundary between the rodlet and the coolant. The capsules were back-filled with helium gas. The temperature of the rodlets is controlled by the gap between the rodlets and the capsule and by the enrichment level of the fuel.

The investigated annular fuel was part of the AFC-3 irradiation experiments, which were performed at the INL Advanced Test Reactor (ATR). The AFC capsules were irradiated in a cadmium-shrouded position that hardens the ATR neutron spectrum to create a radial power profile appropriate for fast spectrum fuel testing [35–37]. Detailed description of the irradiation experiment setup can be found in recent works [13,36]. The irradiation history, including the linear heat generation rate (LHGR, in unit of W/cm) and peak inner cladding temperature (PICT) of each effective full-power day (EFPD), is plotted in Figure 2. As mentioned in a previous AFC-3 study [13], the PICT was calculated from the LHGR and assumed as-built dimensions of the rodlets and capsules.

The effect of fuel cladding gaps/contacts on PICT was simulated by BISON fuel performance code [38] and found to be insignificant with only a 12 ℃ increase of PICT at maximum compared with nominal sodium bonded U-10Zr metallic fuel. However, cladding temperature variation/gradient shows stronger depends on irregularities of fuel cladding gaps/contacts. For example, the elliptical fuel shape and the single point fuel cladding contact during irradiation leads to a maximum temperature of 592 ºC at the contact but a much lower temperature of 528 ºC distant from the contact. The effects of large and small voids at a scale relevant to the microscopy observation (Figure 3) will leads to a temperature variation of 509 ºC–587 ºC and 566 ºC–597 ºC, respectively. Based on these numbers, the uncertainty of the cladding temperature should be within 15 %.

The initial enrichment level of the AFC-3A R4 rodlet was 45 wt.% U-235. The AFC-3A and 3B irradiation lasted for about 120 EFPD. The burnup of the AFC-3A R4 rodlet was determined to be 3.3% fission per initial heavy metal atom (FIMA), and the fission density was about 8.91×10^{20} fission/cm^3.

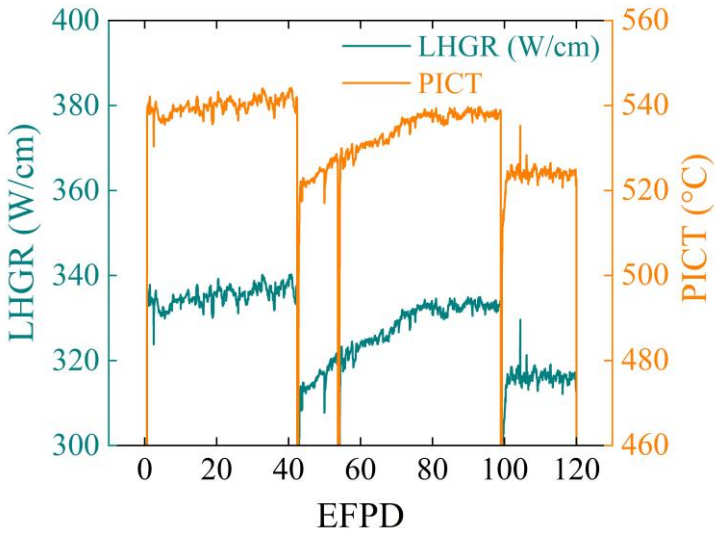

Figure 2. Peak inner cladding temperature (PICT) and linear heat generation rate (LHGR) for each effective full-power day (EFPD) for the AFC-3A R4 rodlet.

2.3 Post-irradiation electron microscopy characterization

The electron microscopy characterization of the irradiated fuel was performed at the Electron Microscopy Laboratory (EML) and the Irradiated Materials Characterization Laboratory (IMCL) at Idaho National Laboratory (INL). A JEOL JSM-7000F field emission gun (FEG) scanning electron microscope (SEM) equipped with energy dispersive X-ray spectroscopy (EDS) was used for the initial microstructure characterization. Figure 3 shows the overall microstructure of irradiated annular U-10Zr fuel with HT-9 cladding.

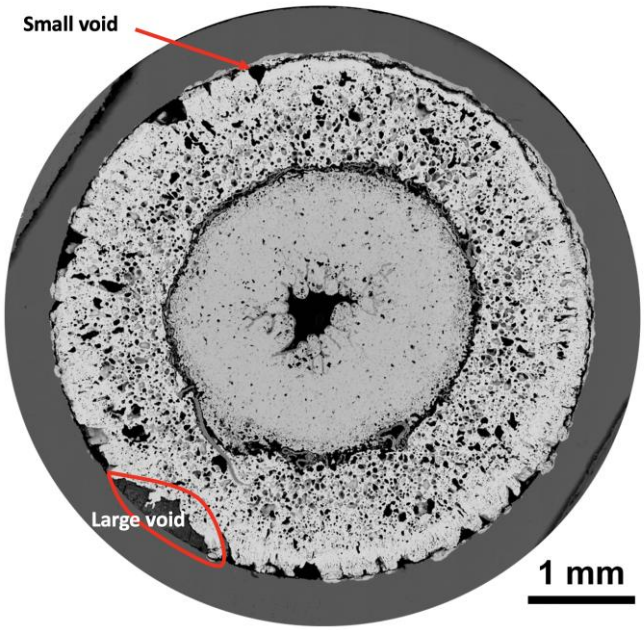

Figure 3. Montage created from a set of SEM images showing the overall microstructure of a cross section of the irradiated annular U-10Zr fuel.

Following the SEM characterization, a FEI Quanta 3D scanning electron microscope/focused ion beam (SEM/FIB) was used to prepare the transmission electron microscopy (TEM) lamellae. After lift-out, the TEM lamellae were mounted onto Cu grids and thinned to a thickness of ~100 nm using 30 keV Ga ions with decreasing ion beam current. The final thinning current was about 100 pA. To minimize FIB-induced damage, the lamellae were polished by 5 keV Ga ions for ~2 min and 2 keV Ga ions for ~4 min. TEM and scanning transmission electron microscopy with energy dispersive X-ray spectroscopy (STEM-EDS) characterization was carried out on a Thermo Scientific Talos F200X field emission gun (FEG) scanning/transmission electron microscope (S/TEM) equipped with ChemiSTEM™ and operated at 200 kV. STEM-EDS was used for elemental mapping and composition analysis. All EDS quantifications were performed using the Thermo Scientific Velox™ software using the default Brown-Powell ionization cross-section model and multi-polynomial model for background correction. TEM diffraction patterns and STEM-EDS results were used together for phase identification.

3. Results

As shown in Figure 3, the dimensions of the cladding and the outer diameter of the irradiated fuel were similar to the unirradiated condition. However, the originally empty center region of the annular fuel is now filled with a new phase. As discussed in a recent PIE study on the AFC-3 fuels [13], this annular fuel grew inward, and the center region seemed more resistant to oxidation than the outer region, suggesting constituent redistribution and higher Zr concentration in the center region.

To gain insight into the elemental distribution in the irradiated fuel, large area SEM-EDS mapping was performed from the center region of the fuel all the way into the cladding, as shown in Figure 4. The U and Zr distribution show that the fuel region is composed of two different phases: a Zr-rich phase at the center region and a U-rich phase at the outer region. A (Zr, Si)-rich layer was found between these two phases, and Si was believed to be from the quartz mold used during fuel fabrication. Chromium was almost exclusively found inside the cladding, indicating no Cr diffusion into the fuel. However, as shown in Figure 4 (d), Fe was found diffused into the fuel. The fuel and the cladding were not in good contact at the chosen EDS mapping region and almost no U was found in the cladding, as shown in Figure 4 (b).

The most surprising result shown in Figure 4 is the distribution of neodymium, which is the most representative element of lanthanides. Nd was mostly retained in the Zr-rich phase at the fuel center, as shown in Figure 4 (c). This is very different from the lanthanide behavior in irradiated solid U-Zr fuels in which the lanthanides were mostly found in the FCCI region [14,27,39].

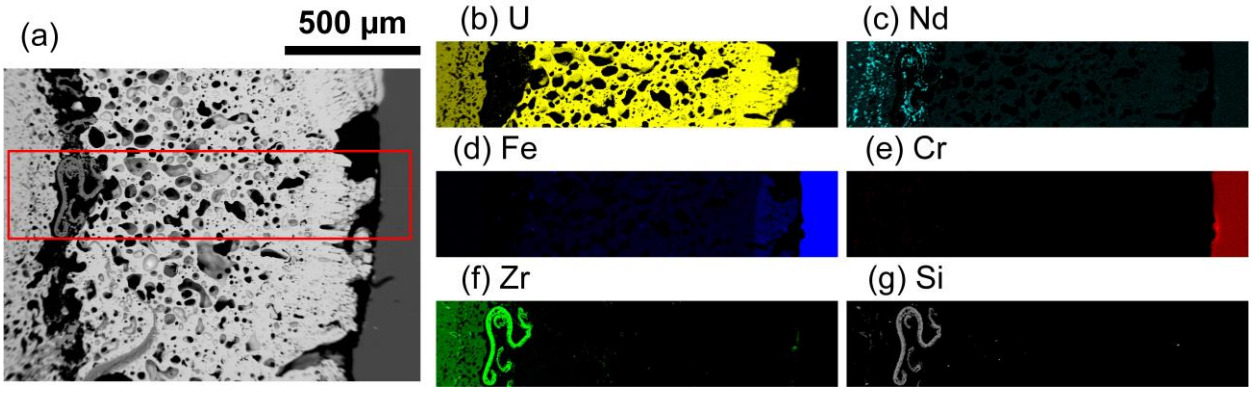

Figure 4. SEM-EDS results showing the overall elemental distribution from the fuel center to the cladding: (a) SEM image, (b)–(g) raw intensity maps of U, Nd, Fe, Cr, Zr, and Si of the region marked by solid red lines in (a).

The fuel came into contact with the cladding and reacted at multiple locations, as shown in Figure 3. To further investigate the detailed microstructure of the FCCI region, two TEM lamellae, lamella #1 and lamella #2, were lifted out from a location that showed significant fuel-cladding contact. The SEM images at different magnifications in Figure 5 shows the locations of the TEM lift-outs. As shown in the high-magnification SEM image in Figure 5 (d), four distinct areas were identified in the wastage zone inside the cladding: Region I inside the interdiffusion zone, Region II at the interface of the interdiffusion zone and the inner cladding, Region III on the cladding side of the interface, and Region IV from the bulk cladding region. The interdiffusion zone-inner cladding interface is basically composed of two thin regions with distinct microstructures: one with a lamellar structure (Region II) and the other (Region III) with two different contrasts (light grey and dark grey). Lamella #1 was lifted out from a region inside the fuel but near the cladding, as shown in Figure 5 (b). Lamella #2 covers all four regions in the wastage zone, as shown in Figure 5 (c)–(d).

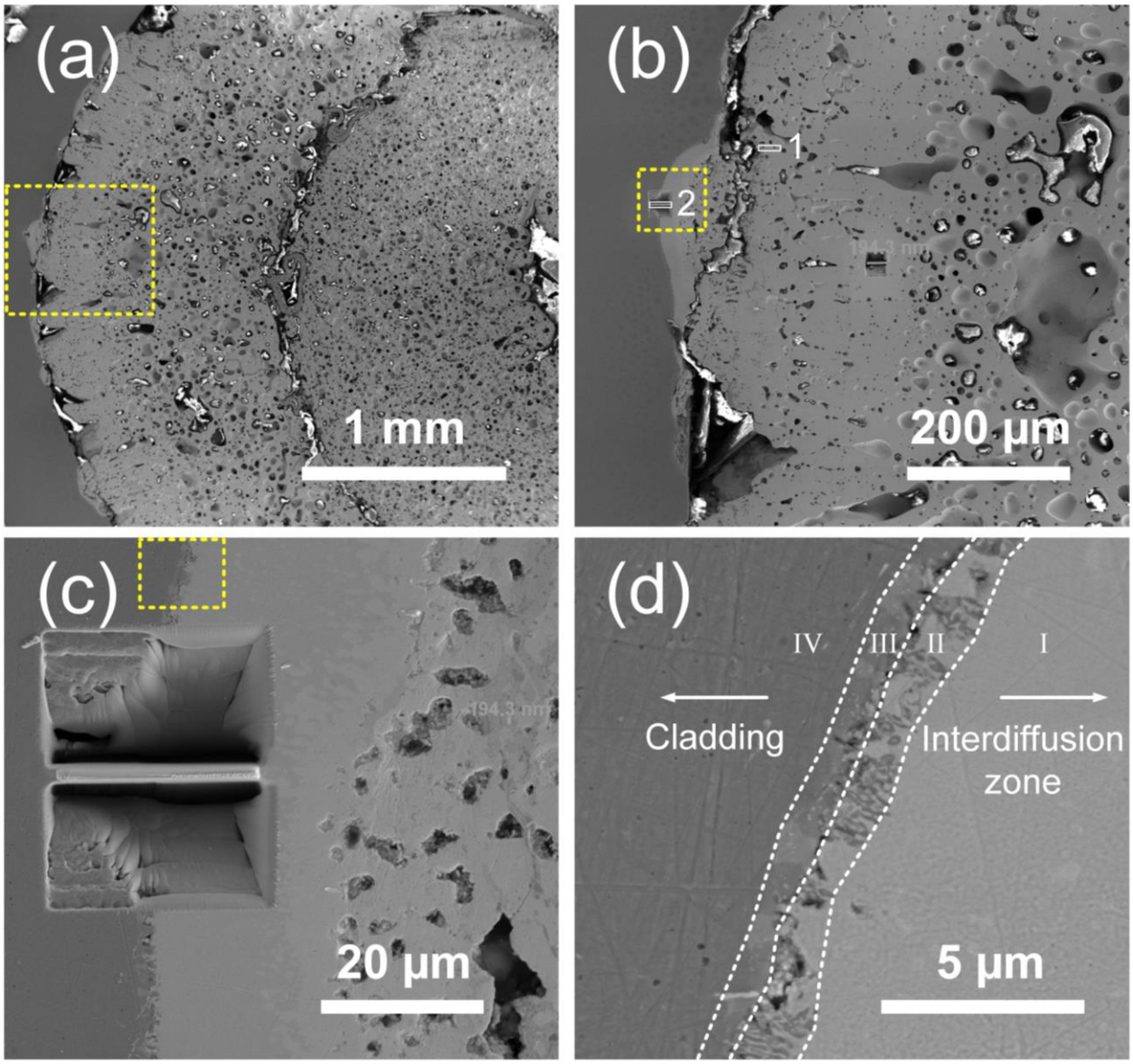

Figure 5. (a)–(d) SEM images at different magnifications showing the microstructure of the FCCI region and the location of the lift-out. Rectangular areas marked by dotted yellow lines indicate the area of the next SEM image. Two lamellae marked as 1 and 2 in (b) were studied in present work.

Before TEM characterization, SEM-EDS mapping was performed at one of the regions that showed good fuel-cladding contact, and an example result is shown in Figure 6. At the fuel-cladding interface, the SEM image and the elemental maps show a lamellar structure similar to the Region II in Figure 5 (d).

It should also be noted that in the SEM images and elemental maps in Figure 6, precipitates which were later confirmed to be U-rich carbides were found at the grain boundaries of the HT-9 grains, as indicated by the red arrows. Most of the precipitates were located inside the light-blue band in Figure 6 (b). A few precipitates were found in the cladding further away from the FCCI interface.

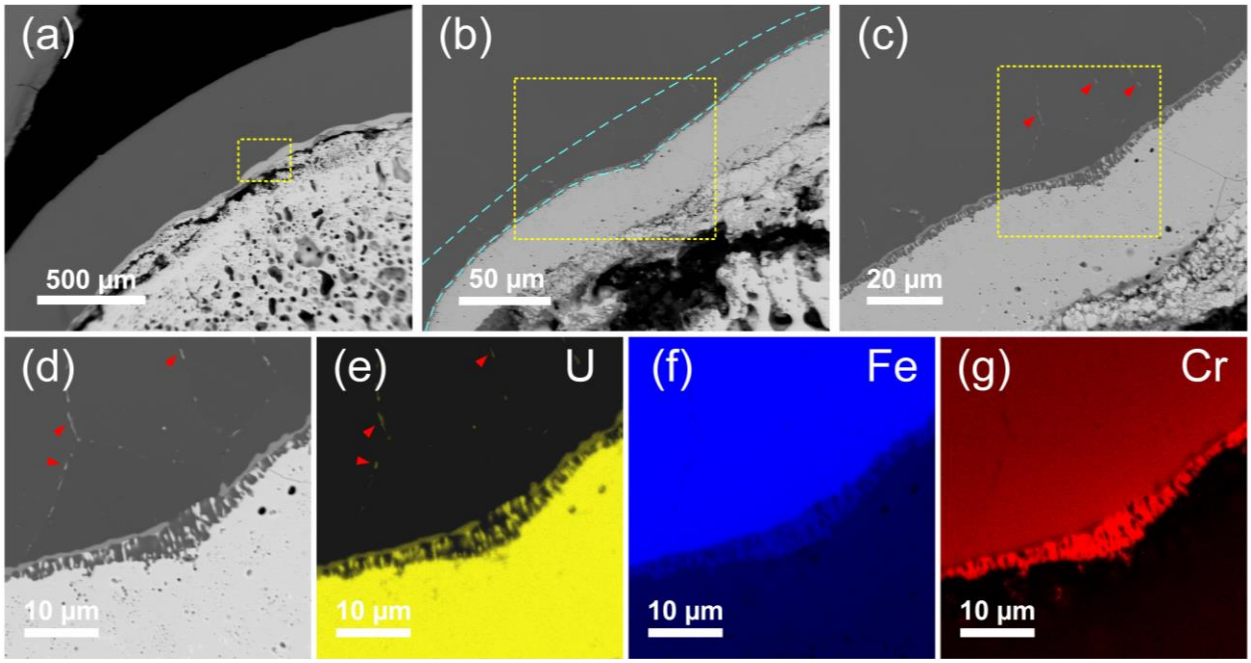

Figure 6. SEM images and EDS mapping showing the microstructure and elemental distribution at the fuel-cladding interface: (a)–(d) SEM images at different magnifications, with the rectangular areas marked by dotted yellow lines indicate the area of the next SEM image; (e)–(g) Elemental maps of U, Fe, and Cr of the region in (d). Red arrows in (c)–(e) indicate the U-rich precipitates at the grain boundaries of HT-9 cladding, and the dashed blue lines in (b) indicate the region where the U-rich precipitates were found.

TEM was then used to reveal details of the microstructure near the FCCI region. Figure 7 shows the STEM-EDS results of lamella #1 lifted out near the edge of the fuel. As shown in the elemental maps in Figure 7 (b)–(d), two phases, one Zr-rich and one (U,Fe)-rich, were found in this lamella. The noticeable Fe signal inside lamella #1 suggests the diffusion of Fe into the fuel. The EDS spectra of the (U,Fe)-rich phase and the Zr-rich phase are shown in Figure 7 (e) and (f), respectively. Based on the spectra, the composition of the Zr-rich phase was measured to be ~96 at% Zr and ~2.4 at% U. The composition of the (U,Fe)-rich phase was measured to be ~77 at% U, ~4 at% Zr, and ~14 at% Fe, very close to the composition of the U_6Fe phase identified in previous U-Fe diffusion couple studies [15–22].

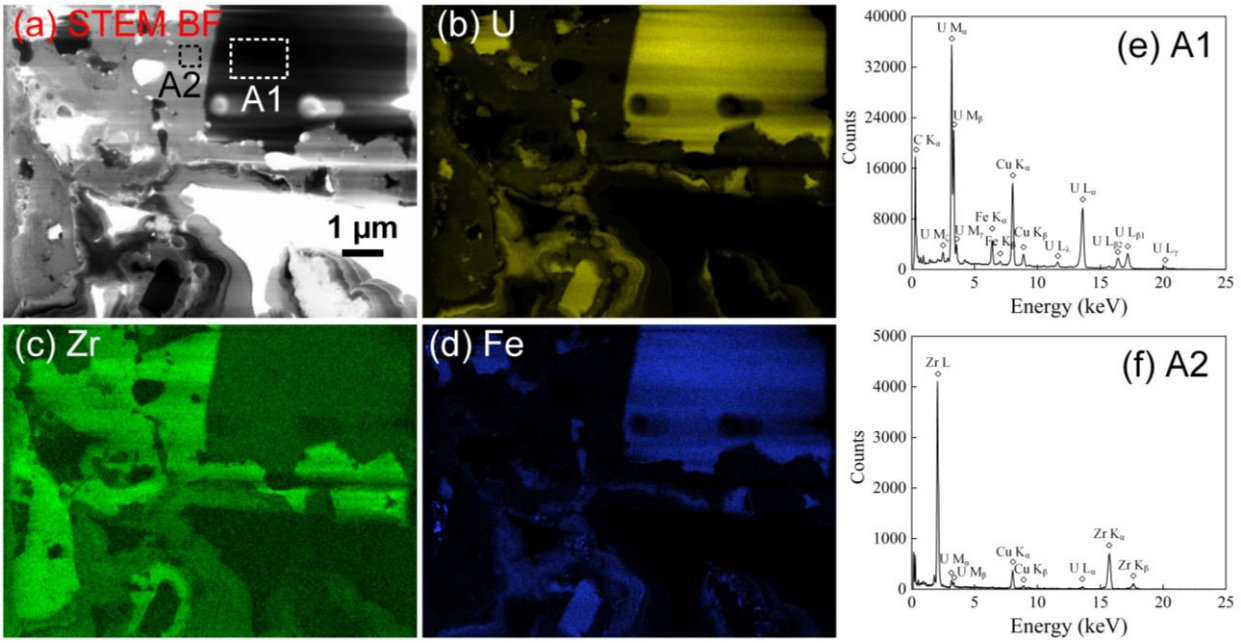

Figure 7. STEM EDS results of lamella #1: (a) STEM bright-field (BF) image, (b)–(d) raw intensity maps of U, Zr, and Fe, (e) EDS spectrum of area A1 marked in (a), (f) EDS spectrum of area A2 marked in (a). The Cu K_α and K_β peaks are background signals from the Cu grid.

To confirm the crystal structure of the (U,Fe)-rich phase, TEM diffraction patterns were acquired, and the results are shown in Figure 8. Indeed all the diffraction patterns from this (U,Fe)-rich phase matched well with the standard tetragonal U_6Fe phase, as shown by the indexed results in Figure 8 (b)–(d). Therefore, the composition and the crystal structure confirms that this (U,Fe)-rich phase is U_6Fe (space group I4/mcm), or more precisely (**U**,Zr)$_6$Fe (bold symbols indicate the dominant elements).

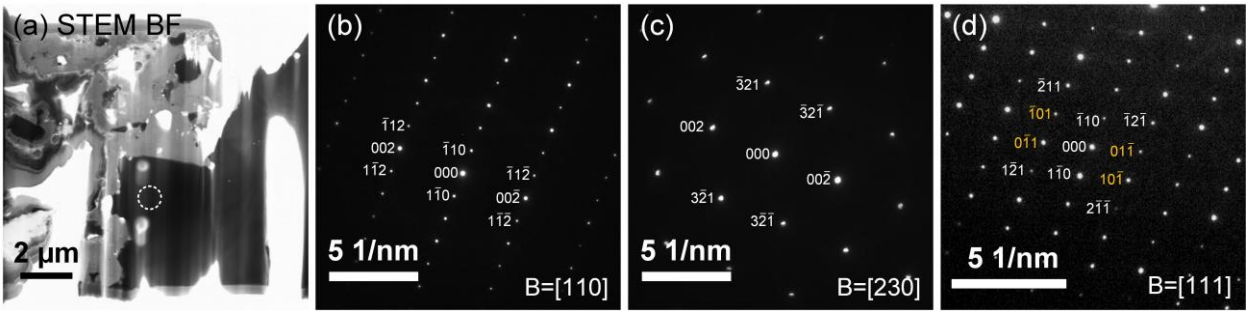

Figure 8. TEM results of the (**U**,Zr)$_6$Fe: (a) STEM BF image, (b)–(d) diffraction patterns of the area marked by dashed white lines in (a), taken at different zones. Yellow labels indicate double diffraction spots.

Lamella #2 was lifted out inside the wastage zone (Figure 5) and has a much more complex microstructure. Figure 9 displays the overall microstructure of the FCCI region contained in TEM lamella #2. Using the same convention as Figure 5 (d), the lamella can be divided into four regions: Region I inside the interdiffusion zone, Region II and III at the interface of the interdiffusion zone and the inner cladding, and Region IV from the cladding region. Region I is marked by fine grains with a high density of nano-sized voids. Region II contains the lamellar structure. Region III is featured by small grains and fine precipitates. Region IV contains relatively large grains with little voids or porosity. The interface region (Regions II and III) is very porous.

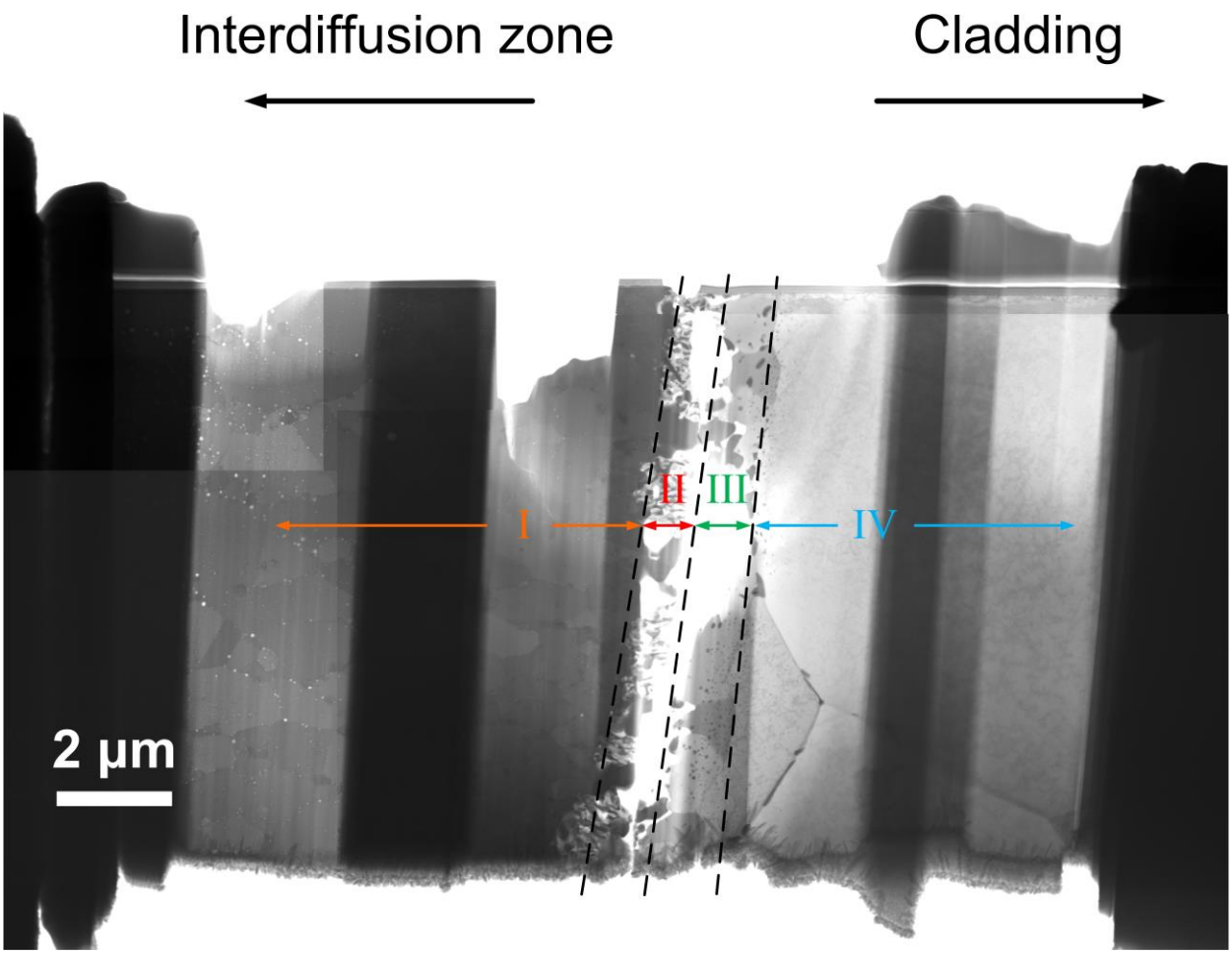

Figure 9. STEM BF image showing the overall microstructure of the FCCI region.

Figure 10 shows the STEM-EDS results of an area inside Region I. The elemental maps show that the matrix of Region I contains U, Fe, and Cr. Uranium carbide precipitates were frequently found in Region I. Figure 10 (g) and (h) also show the EDS spectrum of the uranium carbide (spot 1) and the matrix (spot 2), respectively.

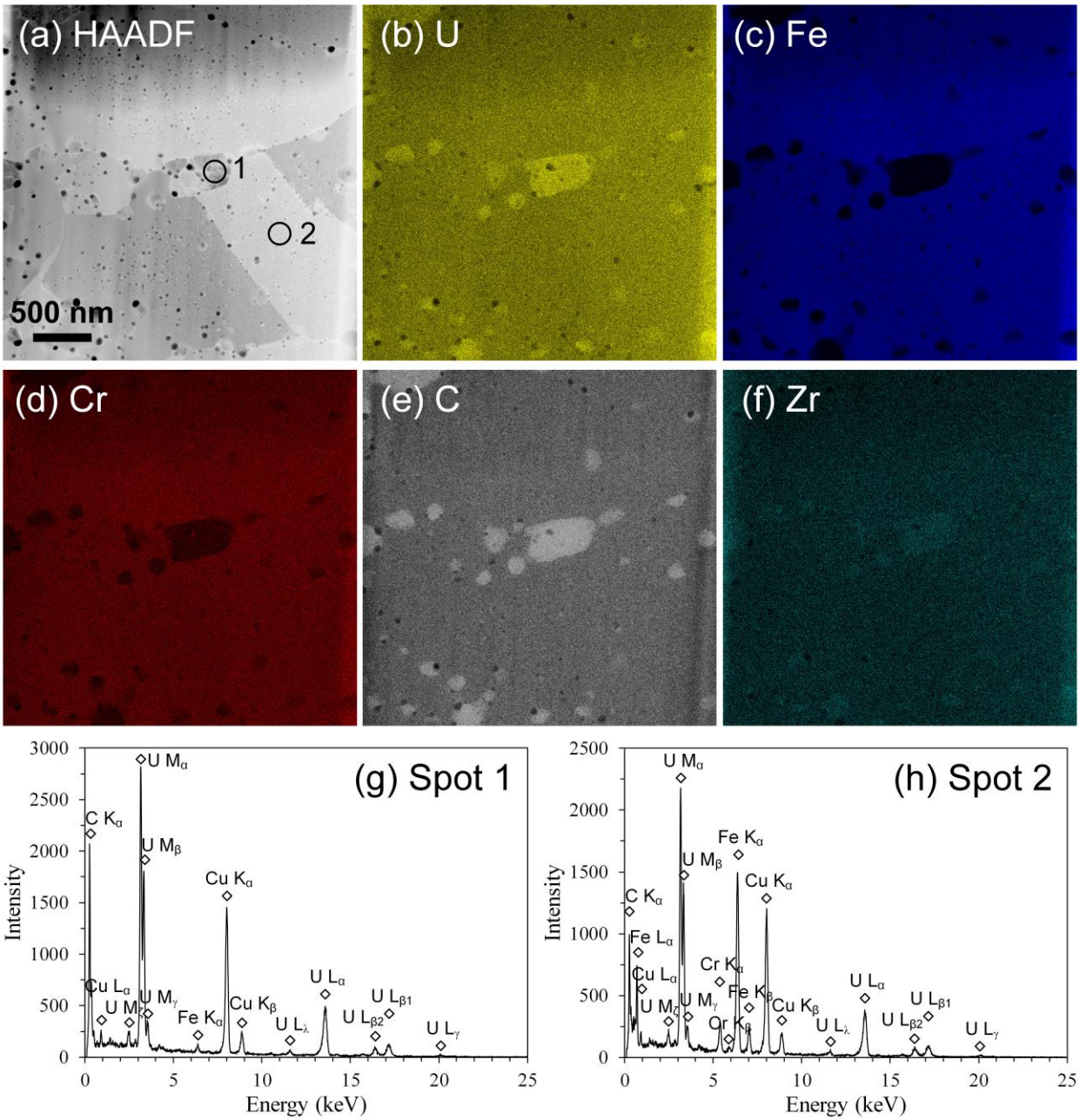

Figure 10. STEM-EDS results of Region I: (a) HAADF image, (b)–(f) raw intensity maps of U, Fe, Cr, C, and W, respectively, (g) EDS spectrum of spot 1 shown in (a), and (h) EDS spectrum of spot 2 shown in (a).

The EDS measurements showed that the matrix in Region I contained about 58.5 at% Fe, 28.1 at% U, 10.0 at% Cr, and 1.2 at% Zr. The (Fe,Cr):(U,Zr) ratio was close to 2:1, which is consistent with the UFe_2 phase. Since U and Fe are the dominant elements, it should be identified as (**U**,Zr)(**Fe**,Cr)$_2$, in which bold symbols indicate the dominant elements.

TEM diffraction patterns were taken to confirm the crystal structure of the matrix in Region I, and the results are shown in Figure 11. Two diffraction patterns (Figure 11 (b) and (c)) were taken and they both matched the UFe_2 phase (space group $Fd\bar{3}m$) perfectly, confirming that the crystal structure of this

(**U**,Zr)(**Fe**,Cr)$_2$ phase is the same as that of the UFe_2 phase that was reported in previous U-Zr and Fe diffusion couple studies [15–17,19–21].

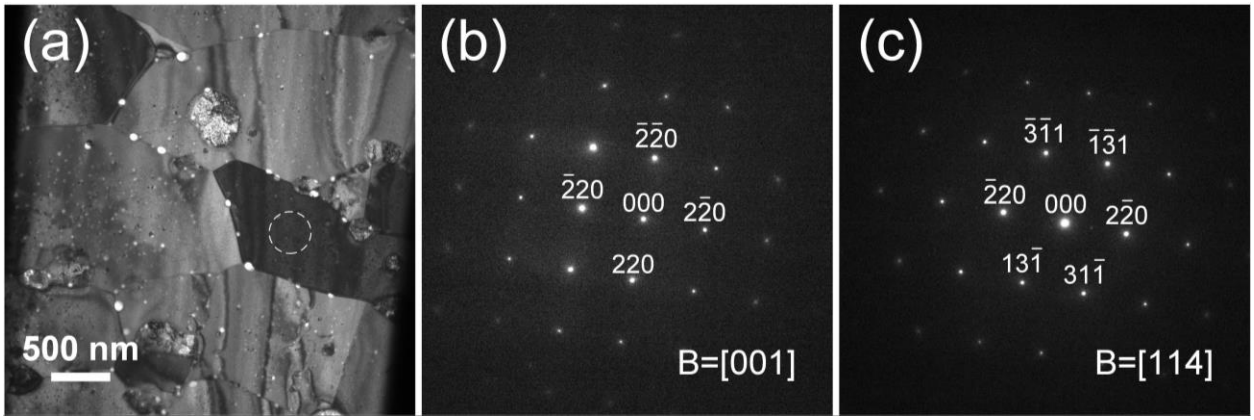

Figure 11. (a) TEM BF image showing the microstructure in Region I, (b) and (c) diffraction patterns taken from the area indicated by the dashed circle in (a).

To confirm the crystal structure of the U-rich carbides in the (**U**,Zr)(**Fe**,Cr)$_2$ phase, TEM diffraction patterns were taken at several different zones. The three diffraction patterns shown in Figure 12 (b)–(d) match perfectly with the [001], [011], and [013] zones of uranium monocarbide (UC) of the NaCl-type crystal structure (space group $Fm\bar{3}m$), respectively. Thus, these U-rich carbides were confirmed to be UC.

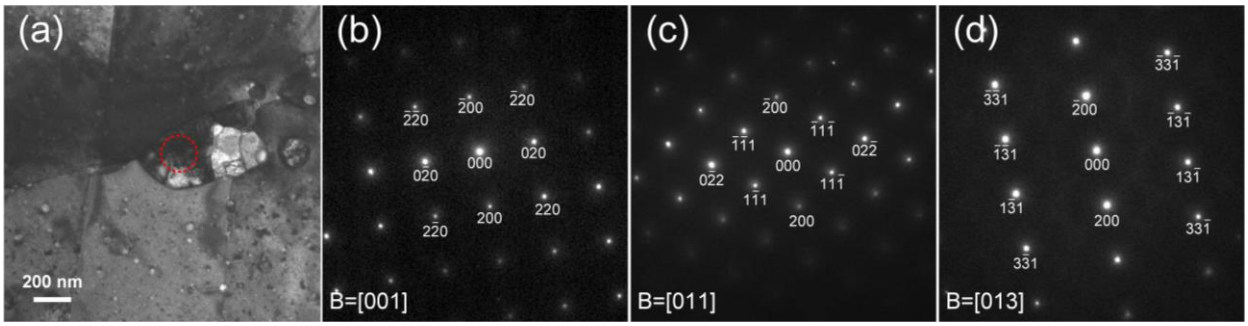

Figure 12. (a) TEM BF image of an intergranular U-rich carbide, (b)–(d) diffraction patterns of the carbide highlighted in (a) at different zone axes. The diffraction patterns confirm the U-rich carbides are uranium monocarbide with a NaCl-type structure.

Details of the microstructure of the (**U**,Zr)(**Fe**,Cr)$_2$ phase are shown in Figure 13. Overall, the (**U**,Zr)(**Fe**,Cr)$_2$ phase contains a high number density of voids, suggesting that this intermetallic phase is prone to irradiation induced swelling. The voids inside grains are generally smaller and some larger voids are located at the interfaces of the uranium carbides. In addition, as shown in the high-magnification STEM BF image in Figure 13 (d) and the corresponding elemental maps in Figure 13 (e)–(h), the voids inside the grains are mostly coupled with small uranium carbide precipitates.

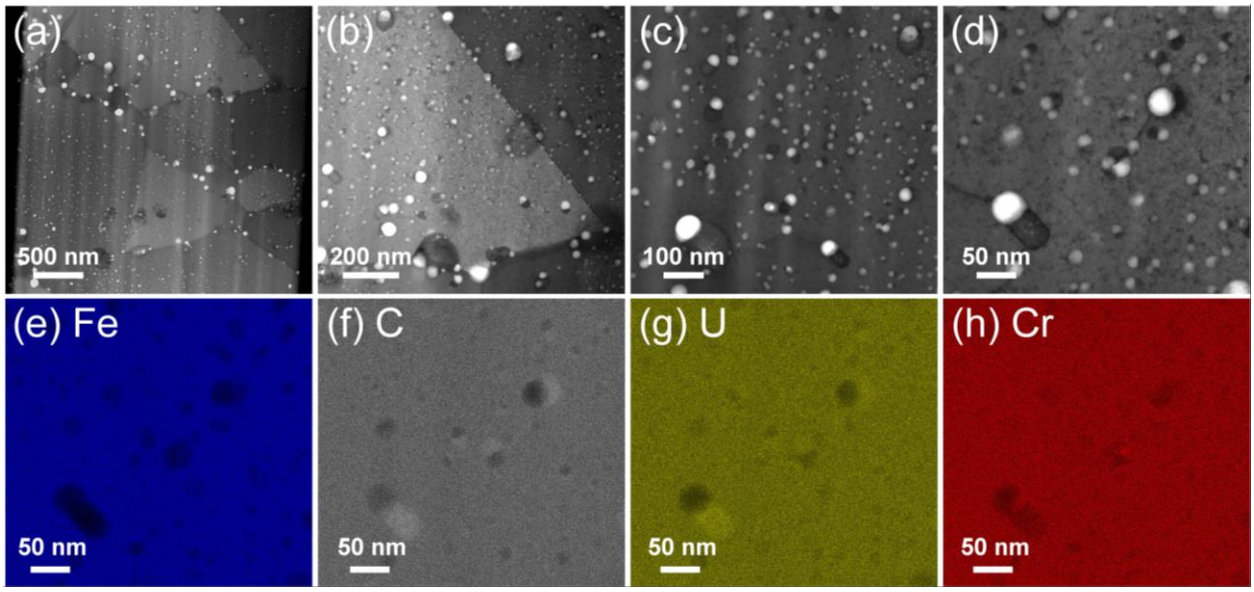

Figure 13. Microstructure of Region I: (a)–(d) STEM BF images of different magnifications, (e)–(h) raw intensity maps of Fe, C, U, and Cr, respectively.

Figure 14. displays the detailed STEM-EDS results of the interaction region. From the high angle annular dark field (HAADF) image in Figure 14 (a) and elemental maps in Figure 14 (b)–(f), it is clear that the interaction region is featured by lamellar structures, uranium carbides, high porosity, and localized distribution of cesium. The lamellar structure is composed of alternating U-rich lamellae and Cr-rich lamellae with a typical width of about 160 nm.

The compositional difference of different regions is more clearly seen in the linescan shown in Figure 14 (g), from which four different regions corresponding to Region I, II, III, and IV are easily identified. From the elemental maps in Figure 14 (b)–(e) show that uranium is mostly found in Region I and Region II, with some U-rich carbides in region III, indicating diffusion of uranium into the cladding. Figure 14 (e) shows that carbon is mostly distributed in Regions I and II, suggesting significant diffusion of carbon into the wastage zone. Figure 14 (d) shows that Regions II and III contain significant amount of chromium, and only limited amount of chromium is found in Region I. It should be noted that some residual cesium was found in Regions II and III, the interface of the interdiffusion zone and the cladding. Since cesium is highly reactive, the actual amount of cesium at the interface before mechanical polishing could be much higher.

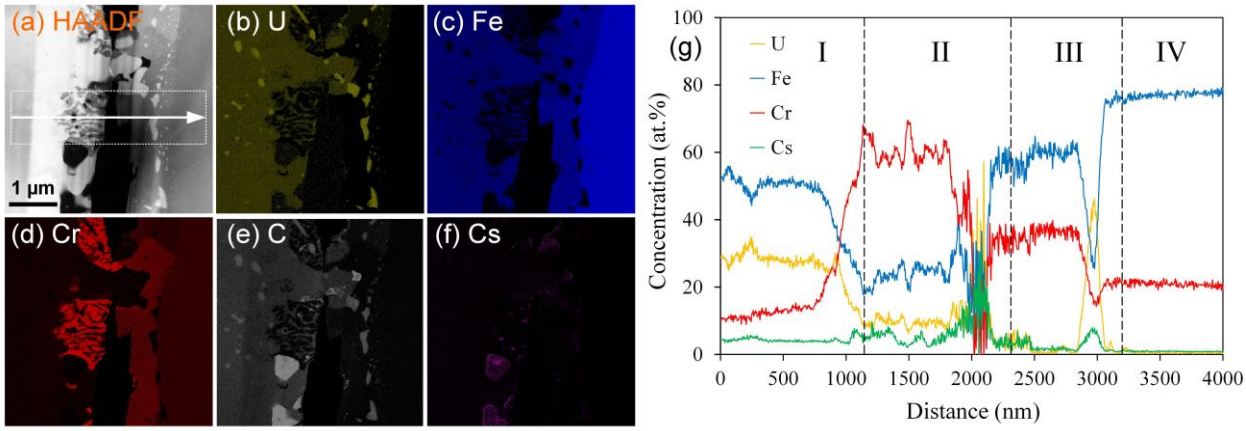

Figure 14. STEM-EDS results of the interaction region: (a) STEM HAADF image, (b)–(f) elemental at.% maps (after quantification) of U, Fe, Cr, C, and Cs, respectively, (g) EDS linescan across the rectangular area marked by dotted white lines in (a).

From the Cr map in Figure 14 (d) and also the EDS linescan in Figure 14 (g), it is apparent that there are noticeable fluctuations in the Cr concentration in both Region II and Region III. The fluctuation in Region II is apparently due to the lamellar structure. The U-rich lamellae are due to the diffusion of uranium into the cladding, and the Cr-rich lamellae are most likely due to the depletion of Fe and the very low solubility of Cr in U.

A closer look into Region III provides some information as to why Region III is also showing concentration fluctuation. Figure 15 shows higher magnification EDS results focusing on Region III. As shown in Figure 15 (a), areas A1, A2, and A3 are inside Region III, and area A4 is in Region IV. The STEM BF image in Figure 15 (a) and elemental maps in Figure 15 (b)–(i) show that there are two different phases in Region III: areas A1 and A3 seem to be one phase with higher Cr concentration, whereas area A2 seems to be a different phase with a lower Cr concentration and also contains some amount of U, Si, Ni, Mo, and W. The compositional differences of these two different phases is also seen from the EDS spectra in Figure 15 (j)–(k), and more quantitatively from the EDS linescan across areas A1 and A2 in Figure 15 (m). From the EDS results, it was confirmed that one phase contained almost only Fe (~59.5 at%) and Cr (~30.8 at%), whereas the other phase contained Fe (~64.0 at%), Cr (~16.4 at%), U (~8.2 at%), Si (~2.3 at%), and Mo (~4.1 at.%).

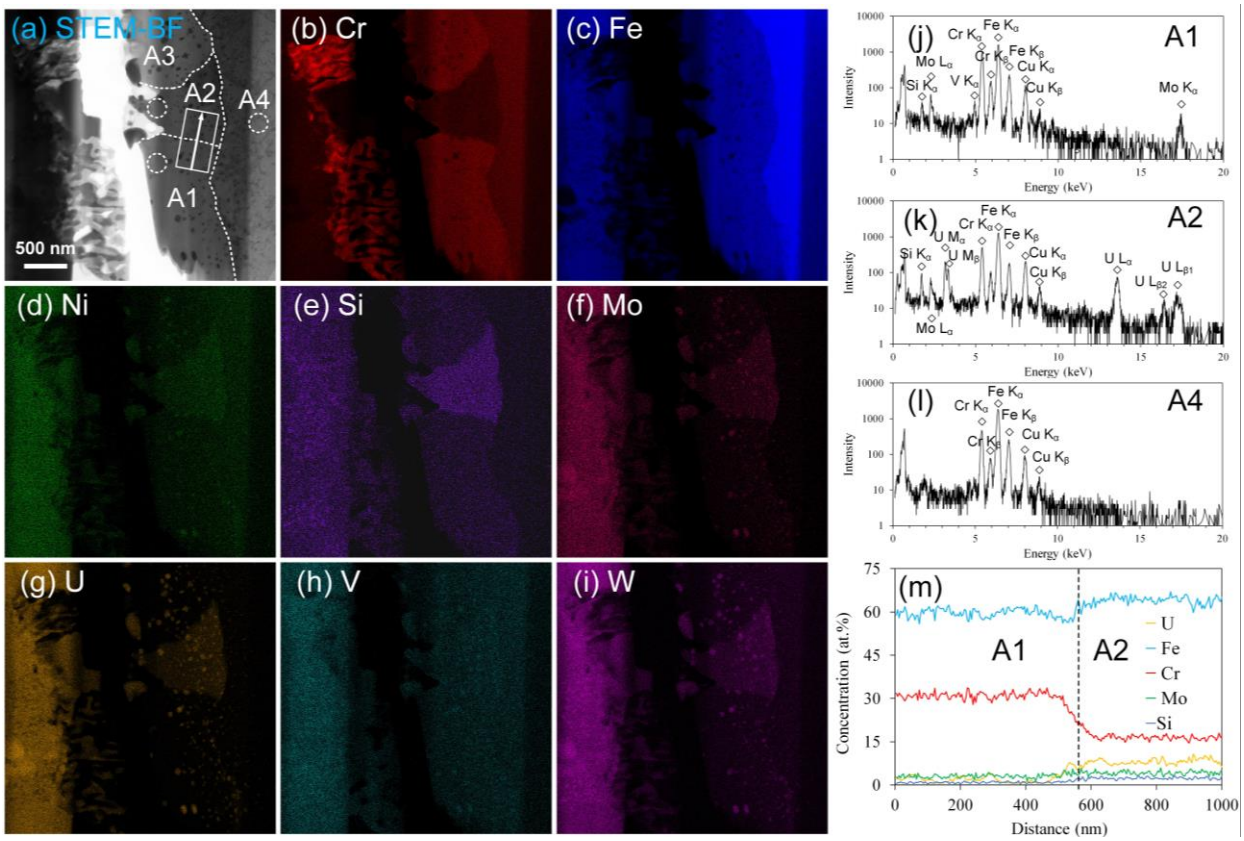

Figure 15. STEM-EDS results of Region III: (a) STEM BF image with four different areas indicated by A1, A2, A3, and A4, (b)–(i) raw intensity maps of Cr, Fe, Ni, Si, Mo, U, V, and W, respectively, (j)–(l) log-scale EDS spectrum corresponding to the areas indicated by dotted circles in A1, A2, and A4, respectively, and (m) EDS linescan from A1 to A2, as indicated by the arrow in (a).

TEM diffraction patterns were then used to identify the crystal structure of the two different phases in Region III, and the results are shown in Figure 16. The diffraction patterns of areas A1 and A3 match well with the binary Fe-Cr σ phase (space group $P4_2/mnm$), as shown by the indexed diffraction patterns of A1 (Figure 16 (b)) and A3 (Figure 16 (g)), respectively. Four diffraction patterns of area A2 were taken, and all four patterns matched well with the quaternary $UCr_{0.1}Fe_{9.9}Si_2$ phase (space group I4/mmm), as shown by the indexed patterns in Figure 16 (c)–(f). In addition, the indexed diffraction pattern of area A4 (Region IV) in Figure 16 (h) confirms that it is the body-centered cubic (BCC) ferrite (α-Fe) phase.

Although the crystal structure of the two phases in Region III was identified, it should be noted that the composition of these two phases differs from those of the standard σ phase and $UCr_{0.1}Fe_{9.9}Si_2$ phase. The σ phase contained only ~30.8 at% Cr and a small amount of Mo. Although there are some discrepancies between calculated Fe-Cr phase diagrams [40–42], the Cr content of the σ phase ranges from ~43% to ~52%, depending on the temperature. The composition of the Fe-Cr-U-Si phase contained less Fe, much more Cr, and much less Si, than the standard $UCr_{0.1}Fe_{9.9}Si_2$ phase.

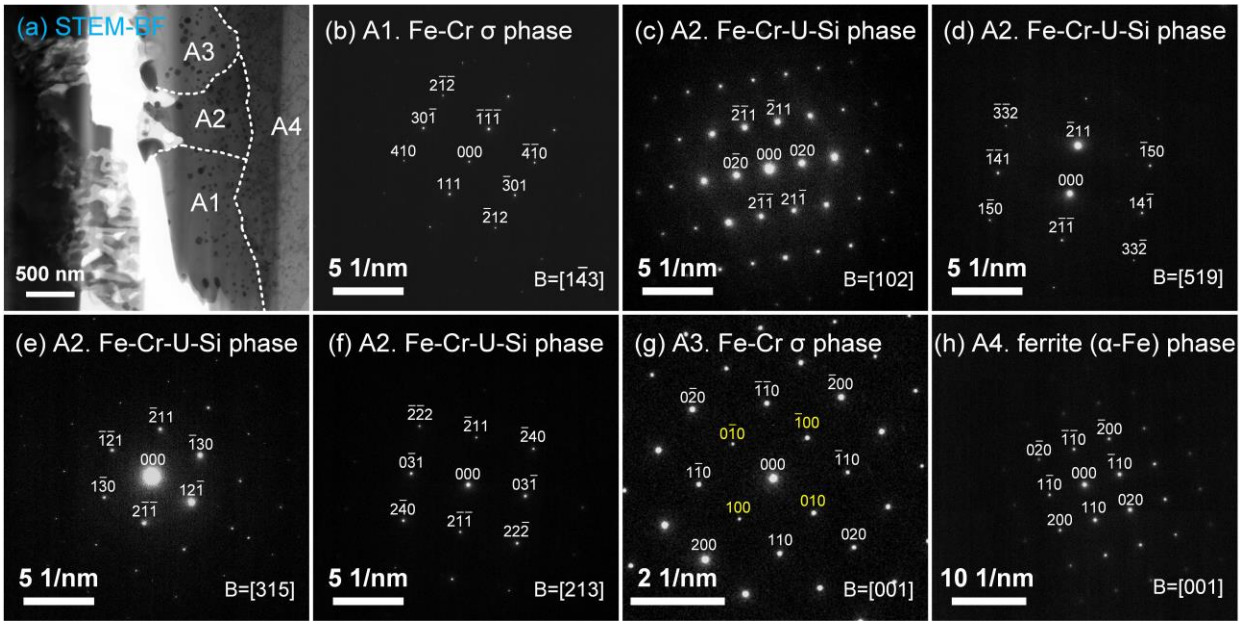

Figure 16. TEM results of the phases in Region III and Region IV: (a) STEM-BF image with areas marked as A1, A2, A3, and A4, (b) diffraction pattern of A1, (c)–(f) diffraction patterns of four different zones of A2, (g) diffraction pattern of A3, and (h) diffraction pattern of A4.

As shown in Figure 16 (h), area A4 in Region IV was identified as the ferrite (α-Fe) phase. However, as displayed in Figure 14 (g), the average Cr concentration of Region IV has increased to ~18 at%, and the average Fe concentration has decreased to ~76 at%, which are significantly different from the composition of unreacted HT-9 (~12.19 at% Cr) before irradiation. The increase in Cr concentration and decrease in Fe concentration in the cladding are apparently the result of the diffusion of Fe from the cladding into the fuel, as shown by the observed $(\mathbf{U},Zr)_6Fe$ and $(\mathbf{U},Zr)(\mathbf{Fe},Cr)_2$ phases. Because of the diffusion of Fe, a spatial gradient is expected along the diffusion direction. A closer look at the chemical composition inside the cladding region (Region IV) shows that the Cr and Fe concentrations are indeed not constant but are dependent on the radial location. The results are shown in Figure 17. It is apparent that the Cr content is much higher than ~12.19 at%, and it decreases with increasing distance from the interaction region.

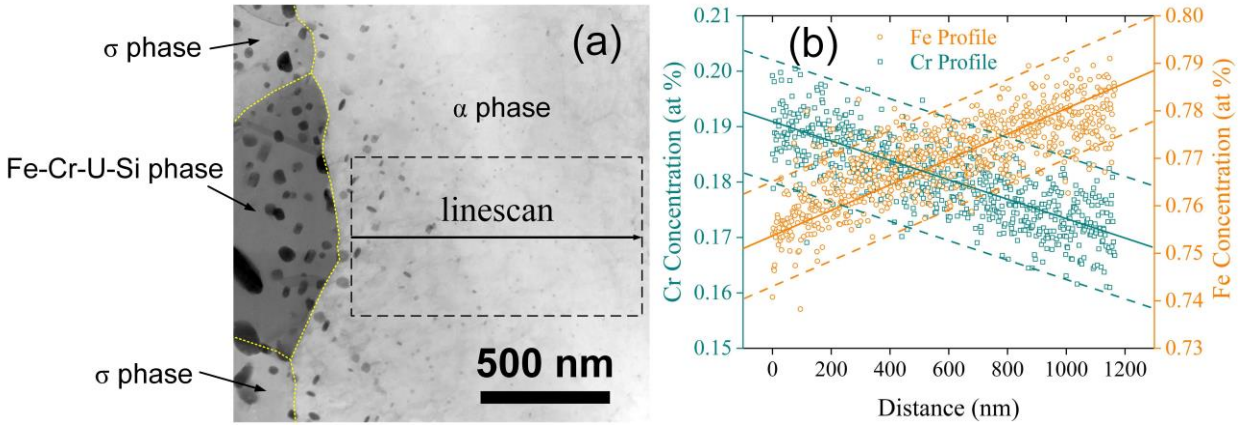

Figure 17. STEM-EDS results of the ferrite (α-Fe) phase: (a) STEM-BF image showing the microstructure of the α-Fe phase, σ phase, and Fe-Cr-U-Si phase, and (b) EDS linescan showing the Fe and Cr profiles. The EDS linescan area is marked by dotted black lines in (a).

HT-9 is a well-known Fe-12Cr ferritic/martensitic steel that has shown excellent swelling resistance in previous irradiation studies. The microstructure of HT-9 is composed of a tempered martensite structure, and the martensite lath is typically several hundred nanometers in width. Both Figure 17 (a) and Region IV in Figure 9 show that the martensite lath structure has disappeared, with only relatively large ferrite (α-Fe) grains in Region IV. This phenomenon can be more clearly seen from the low-magnification backscattered electron image in Figure 18, which shows that the grains close to the FCCI region become equiaxed ferrite grains, whereas the grains near the outer surface of the cladding still maintains the martensite lath structure. The equiaxed ferrite grain structure was even found at regions ~200 μm away from the FCCI region.

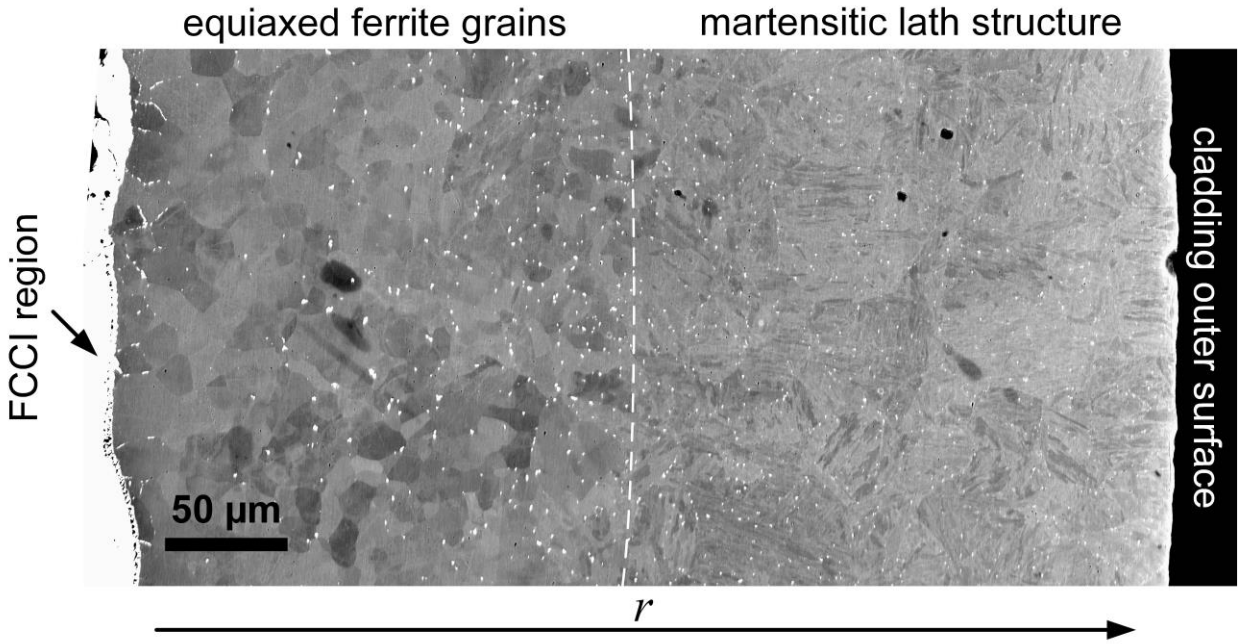

Figure 18. Backscattered electron image showing an overview of the microstructure of the cladding at different radial locations. The white dots are mostly carbides.

The disappearing of the martensite lath structure in the inner region of the cladding is likely due to the diffusion of carbon into the wastage zone, which also resulted in the aforementioned UC precipitates in the (**U**,Zr)(**Fe**,Cr)$_2$ phase. The loss of carbon destabilizes the martensite structure, and ferrite grains are formed instead. The area affected by decarbonization extended much deeper (~200 μm) into the cladding compared with the size of the wastage zone. A similar decarbonization and ferrite formation process in HT-9 cladding after FCCI was mentioned in a previous study [3], in which it was reported that in a solid U-10Zr fuel with HT-9 cladding, a decarbonized zone of ~100 um was developed after 5 at% burnup.

4. Discussions

4.1 Distribution of lanthanides

One of the most unique features of this irradiated U-10Zr fuel is the spatial distribution of the lanthanides. Previous studies [14,32] of solid U-Zr fuel with HT-9 cladding have found significant amount of lanthanides, primarily neodymium and cerium, in the FCCI region at high burnup (> 10 at%). Some low burnup studies [27,39] also confirmed similar behaviors of lanthanides in solid U-Zr fuels. A study [39] of the historical X447 EBR-II experiment indicated that lanthanide fission products were already present in the FCCI region in the DP-69 pin at a local burnup as low as 2.4% FIMA and an average PICT of 667 °C. A recent study of Mechanistic Fuel Failure-3 (MFF-3) experiment showed significant lanthanide distribution in the FCCI region in fuel pin #193045, which has a local burnup of 5.7 % FIMA and an average PICT of 615 °C. Thus, it is believed that the lanthanides in solid U-10Zr fuel can transport and redistribute to the FCCI region even at relatively low burnup. In contrast, almost no lanthanides were found in the FCCI region in this present work. Instead, most lanthanides were found to be retained in the center region where the Zr-rich phase is dominant. The lanthanides observed in the FCCI layer in previous solid U-Zr fuel studies were assumed to be driven by liquid-like diffusion [32] through the fuel pores that were partially filled with sodium and cesium, followed by similar liquid-like diffusion through the sodium bond from the fuel surface to the cladding. In the annular fuel, helium gas replaced the liquid sodium bond. Therefore, the liquid-like diffusion through fuel pores and from the fuel surface to the cladding is significantly suppressed. The fact that much less lanthanides were found in helium back-filled annular fuel might indirectly support the liquid-like diffusion mechanism of lanthanides, which has not been determined yet.

The lanthanide behavior in the annular fuel indicates that the annular fuel using helium bond could be a promising alternative fuel form for fast reactor applications. Elimination of sodium can not only provide back-end fuel cycle benefits but also offer an alternative way to mitigate the transport of lanthanides to the FCCI region by suppressing the liquid-like diffusion mechanism. Further irradiation testing is needed to confirm the lanthanide distribution at higher burnups.

4.2 (**U**,Zr)$_6$Fe and (**U**,Zr)(**Fe**,Cr)$_2$ phases due to interdiffusion of uranium and iron

The interdiffusion of U and Fe near the FCCI region formed tetragonal (**U**,Zr)$_6$Fe phase and cubic (**U**,Zr)(**Fe**,Cr)$_2$ phase. The (**U**,Zr)$_6$Fe is located near the edge of the fuel, and the (**U**,Zr)(**Fe**,Cr)$_2$ phase is in the wastage zone inside the cladding. These two phases are similar to those found in previous U-Fe diffusion couple studies [15–22]. However, the microstructure of the irradiated (**U**,Zr)(**Fe**,Cr)$_2$ phase is much more complicated than the pure UFe_2 phase formed in diffusion couple studies. As shown in Figure 13, the (**U**,Zr)(**Fe**,Cr)$_2$ phase contains a high density of voids and intergranular UC precipitates, indicating that the intermetallic (**U**,Zr)(**Fe**,Cr)$_2$ phase is susceptible to void swelling under irradiation and can therefore degrade the mechanical property of the inner cladding region.

4.3 Compositional and microstructural changes in the cladding

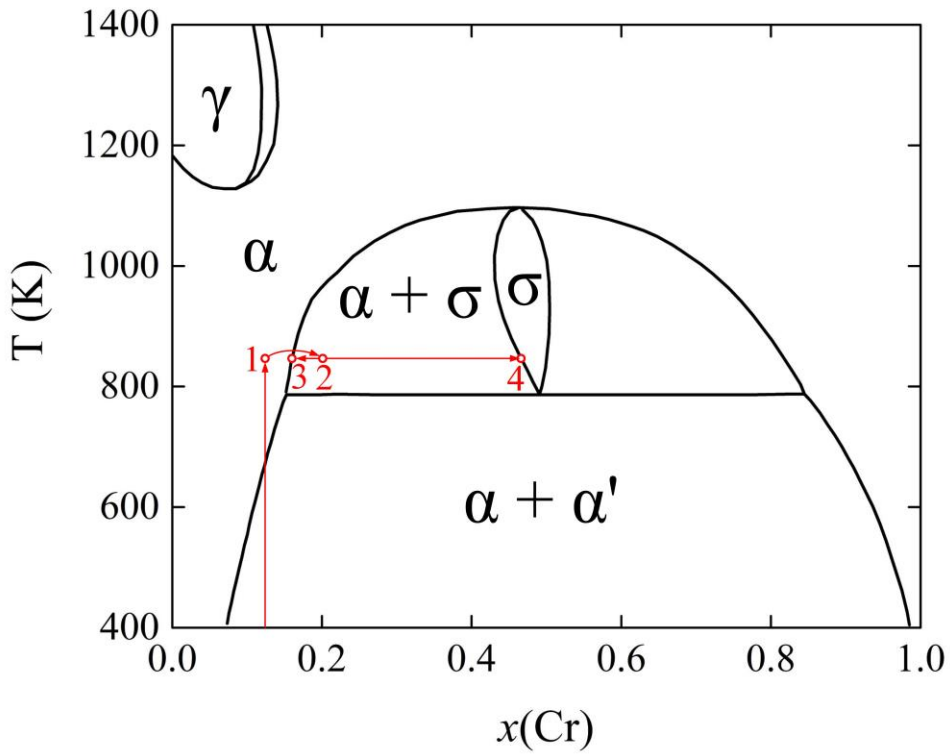

Figure 19. A likely pathway of the observed phase transformation in Region III based on the current Fe-Cr phase diagram [43].

At the cladding side of the interface of the interdiffusion zone and the cladding region (Region III), two different phases were observed: the Fe-Cr σ phase and the tetragonal Fe-Cr-U-Si phase. These two phases are different from the original ferrite/martensite α-Fe phase of HT-9, indicating that phase transformation has occurred at the inner surface of the cladding. Since the unirradiated HT-9 contains only ~12.19 at% Cr, such phase transformation was not expected. A likely pathway for such phase transformation is shown on the Fe-Cr phase diagram [43] in Figure 19. The unirradiated HT-9 contains ~12.19 at% Cr. Therefore, the starting point is somewhere inside the miscibility gap (α+α' region). At the beginning of irradiation, the cladding temperature was raised to ~540 ºC (813 K), and the system was brought to point 1. With increasing burnup, Fe started to diffuse into the fuel, and the Cr content of the most inner region of the cladding started to increase correspondingly. This causes the system to move from point 1 to point 2, passing the α–σ phase boundary. Now the system is thermodynamically favorable to decompose into the σ phase (point 4) and the α phase (point 3). The σ phase is one of the two phases observed in Region III. However, because of the diffusion of uranium into the cladding, the other phase, the α phase, was further transformed to the Fe-Cr-U-Si phase. It should be noted that the compositions of the Fe-Cr σ phase and the tetragonal Fe-Cr-U-Si phase differ from the compositions of the equilibrium σ phase and the standard $UCr_{0.1}Fe_{9.9}Si_2$ phase, respectively. A likely reason is that these two phases were under neutron irradiation and were not at equilibrium. It should also be noted that both phases contain significant amount of uranium carbide precipitates, due to the interdiffusion of U and C.

Two conditions are needed to result in the observed phase transformation: noticeable diffusion of Fe away from the cladding to raise the Cr content and temperature high enough to enter the α+σ region. The brittle σ phase could result in cladding embrittlement. To avoid such phase transformation, ways to suppress the

diffusion of Fe into the fuel would be helpful (e.g., introduce internal sinks into the cladding to suppress radiation-enhanced diffusion).

The diffusion of Fe not only resulted in the phase transformation at the inner surface of the cladding, but also raised the Cr content in Region IV inside the cladding. For lower temperature irradiation, the increase in Cr content moves the system further into the α+α' region and can potentially enhance the formation of the brittle α' phase [44–46].

Another consequence of the FCCI is that the martensite lath structure at the inner side of the cladding is gone, possibly due to decarbonization caused by the diffusion of C into the wastage zone. The martensite structure is characterized by high densities of dislocations and lath structure. This is different from the α phase shown in Figure 17, indicating that the original martensite has transformed to the ferrite phase. Uranium carbide precipitates were found in the ferrite (α-Fe) grains in Region IV. The carbides appear as small precipitates inside the ferrite grains (Figure 17) and as large precipitates at the ferrite grain boundaries (Figure 6 and Figure 9) and the phase boundaries between Region III and Region IV. The uranium carbide precipitates were only found in the first ~15–30 μm region away from the interface, and the equiaxed ferrite grain structure extended ~200 μm deep into the cladding.

These changes in the composition and microstructure of the region near the FCCI layer in the cladding could adversely affect the local mechanical properties and radiation resistance of the cladding. Fuel fabrication defects have a direct impact on the formation and evolution of FCCI layer. Based on the experience of AFC-3A/B irradiation, a final machining step was added after casting of AFC-3C/D annular fuels to ensure a controlled small (<25 μm) gap size, which mitigated FCCI and improved the fuel performance [47].

5. Conclusions

Annular U-Zr fuel is a promising fuel form due to its back-end fuel cycle benefits. Using advanced electron microscopy and spectroscopy characterization techniques, this study revealed the fuel cladding chemical interaction characteristics of a prototype annular U-10wt%Zr fuel and a Fe-12Cr base HT-9 cladding irradiated to 3.3% FIMA. Unlike the solid U-Zr fuels, most lanthanides were retained in the newly formed UZr_2 phase in the center region of the irradiated annular U-10Zr fuel, suggesting an alternative way to mitigate the transport of lanthanides to the FCCI region. Higher burnup irradiation testing is required to confirm whether the center UZr_2 phase region can still retain the lanthanides at higher burnups.

Based on the microstructure results, the microstructural evolution near the FCCI region of the investigated annular U-10Zr fuel with HT-9 cladding is illustrated in Figure 20.

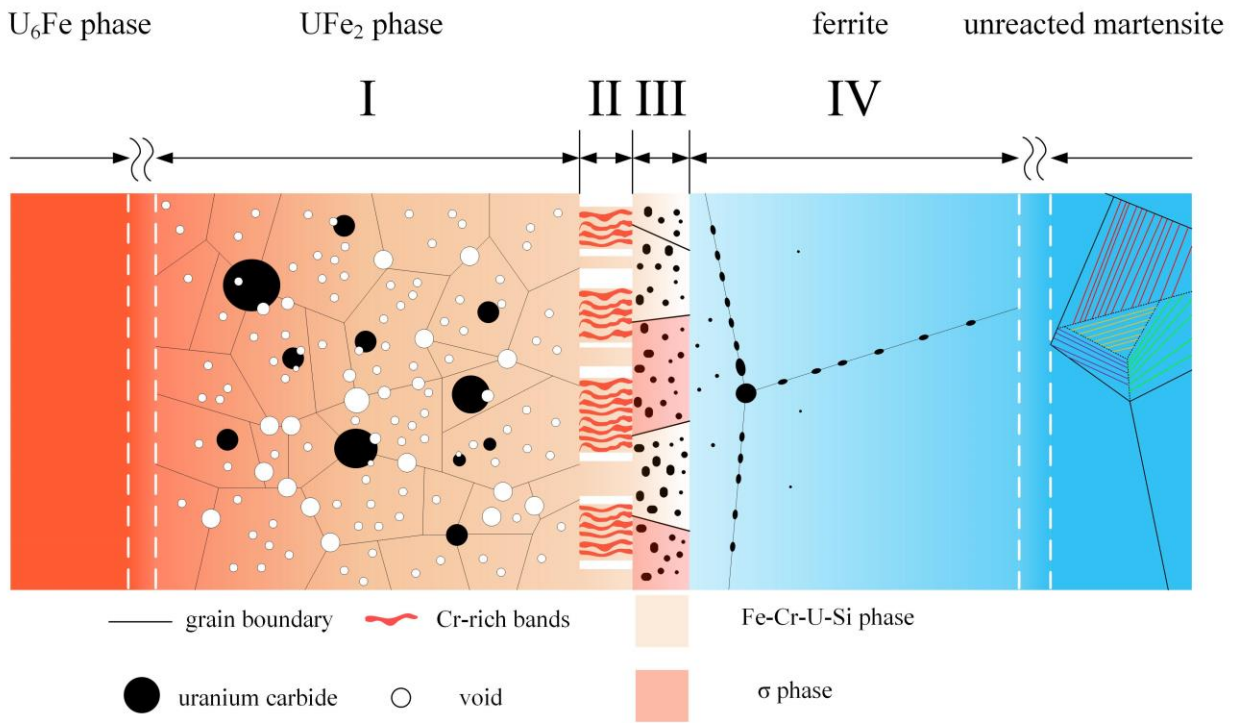

Figure 20. Illustration of the microstructural evolution near the FCCI region.

In the FCCI interdiffusion region, cubic (**U**,Zr)(**Fe**,Cr)$_2$ phase and tetragonal (**U**,Zr)$_6$Fe phase were formed. The (**U**,Zr)(**Fe**,Cr)$_2$ phase contained a significant number of voids and UC precipitates. Most of the voids are spatially associated with the UC precipitates.

At the interface region (Region II and Region III), a lamellar structure was found on the interdiffusion zone side (Region II), and phase transformation was identified on the cladding side (Region III). The lamellar structure is composed of alternating U-rich lamellae and Cr-rich lamellae with a typical width of about 160 nm.

Two phases were identified in Region III: the σ phase and the tetragonal Fe-Cr-U-Si phase. The phase transformation in Region III was explained by a pathway on the Fe-Cr phase diagram. The diffusion of Fe (increase in Cr content) from the cladding into the fuel and high temperature (e.g., ~540 ºC) are both required to form the σ phase. The Fe-Cr-U-Si phase was formed due to the diffusion of U into the cladding.

In the inner bulk cladding region (Region IV), martensite lath structure was not observed, and large ferrite grains were found, possibly due to the diffusion of C into the wastage zone. The Cr content of the ferrite grains is much higher (~18 at%) than that of the unirradiated HT-9 (~12.19 at%), and the ferrite grains contain small intragranular uranium carbide precipitates and large intergranular uranium carbide precipitates. Uranium carbide precipitates were found only in the first ~15–30 μm region away from the interface. These microstructural and compositional changes of the cladding could result in local degradation of mechanical properties and radiation resistance.

It should be noted that this prototype annular fuel had imperfect cylindricity, and the actual local cladding temperature varied at different locations depending on the local fuel-cladding gap size. In some locations, the local cladding temperature was much hotter than expected. Improvements of the fuel fabrication processes, especially a final machining step was adopted for AFC-3C/D annular fuel slugs to ensure a controlled small fuel-cladding gap size, and the fuel performance was significantly improved.

Acknowledgment

X. Liu acknowledges the financial support from the U.S. Department of Energy, Office of Nuclear Energy under DOE Idaho Operations Office Contract DEAC07-051D14517 as part of a Nuclear Science User Facilities. T. Yao and L. He acknowledge the support from the Center for Thermal Energy Transport under Irradiation, an Energy Frontier Research Center funded by the U.S. Department of Energy, Office of Science, Basic Energy Sciences. This work was supported by the Advanced Fuels Campaign (AFC) of the Nuclear Technology Research and Development (NTRD) program in the U.S. Department of Energy, Office of Nuclear Energy under DOE Idaho Operations Office Contract DE-AC07-05ID14517. Accordingly, the U.S. Government retains and the publisher, by accepting the article for publication, acknowledges that the U.S. Government retains a nonexclusive, paid-up, irrevocable, worldwide license to publish or reproduce the published form of this manuscript or allow others to do so, for U.S. Government purposes.

References

[1] K. Aoto, P. Dufour, Y. Hongyi, J.P. Glatz, Y. Kim, Y. Ashurko, R. Hill, N. Uto, A summary of sodium-cooled fast reactor development, Prog. Nucl. Energy. 77 (2014) 247–265. doi:10.1016/j.pnucene.2014.05.008.

[2] S. Hayes, D. Dempsey, J.M. Harp, G.L. Povirk, Developmental Objectives for Advanced Reactor Fuels, Idaho Falls, ID (United States), 2017. doi:10.2172/1599357.

[3] G.L. Hofman, L.C. Walters, T.H. Bauer, Metallic fast reactor fuels, Prog. Nucl. Energy. 31 (1997) 83–110. doi:10.1016/0149-1970(96)00005-4.

[4] W.J. Carmack, D.L. Porter, Y.I. Chang, S.L. Hayes, M.K. Meyer, D.E. Burkes, C.B. Lee, T. Mizuno, F. Delage, J. Somers, Metallic fuels for advanced reactors, J. Nucl. Mater. 392 (2009) 139–150. doi:10.1016/j.jnucmat.2009.03.007.

[5] D.C. Crawford, D.L. Porter, S.L. Hayes, Fuels for sodium-cooled fast reactors: US perspective, J. Nucl. Mater. 371 (2007) 202–231. doi:10.1016/j.jnucmat.2007.05.010.

[6] Y.-I. Chang, TECHNICAL RATIONALE FOR METAL FUEL IN FAST REACTORS, Nucl. Eng. Technol. 39 (2007) 161–170. doi:10.5516/NET.2007.39.3.161.

[7] G.L. Hofman, R.G. Pahl, C.E. Lahm, D.L. Porter, Swelling behavior of U-Pu-Zr fuel, Metall. Trans. A. 21 (1990) 517–528. doi:10.1007/BF02671924.

[8] C.B. Lee, D.H. Kim, Y.H. Jung, Fission gas release and swelling model of metallic fast reactor fuel, J. Nucl. Mater. 288 (2001) 29–42. doi:10.1016/S0022-3115(00)00718-2.

[9] C. Matthews, C. Unal, J. Galloway, D.D. Keiser, S.L. Hayes, Fuel-Cladding Chemical Interaction in U-Pu-Zr Metallic Fuels: A Critical Review, Nucl. Technol. 198 (2017) 231–259. doi:10.1080/00295450.2017.1323535.

[10] D.D. Keiser, Fuel cladding chemical interaction in metallic sodium fast reactor fuels: A historical perspective, J. Nucl. Mater. 514 (2019) 393–398. doi:10.1016/j.jnucmat.2018.09.045.

[11] D.L. Porter, C.B. Hilton, Extending Sodium Fast Reactor Driver Fuel Use to Higher Temperatures, Nucl. Technol. 173 (2011) 218–225. doi:10.13182/NT11-A11551.

[12] L.R. Blake, Achieving high burn-up in fast reactors, J. Nucl. Energy. Parts A/B. React. Sci. Technol. 14 (1961) 31–48. doi:10.1016/0368-3230(61)90071-4.

[13] J.M. Harp, H.J.M. Chichester, L. Capriotti, Postirradiation examination results of several metallic fuel alloys and forms from low burnup AFC irradiations, J. Nucl. Mater. 509 (2018) 377–391. doi:10.1016/j.jnucmat.2018.07.003.

[14] D.D. Keiser, Fuel-cladding interaction layers in irradiated U-Zr and U-Pu-Zr fuel elements, Argonne, IL (United States), 2006. doi:10.2172/885496.

[15] T. Ogata, M. Kurata, K. Nakamura, A. Itoh, M. Akabori, Reactions between U–Zr alloys and Fe at 923 K, J. Nucl. Mater. 250 (1997) 171–175. doi:10.1016/S0022-3115(97)00262-6.

[16] T. Chen, T.A. Smith, J.G. Gigax, D. Chen, R. Balerio, L. Shao, B.H. Sencer, J.R. Kennedy, Intermetallic formation and interdiffusion in diffusion couples made of uranium and single crystal iron, J. Nucl. Mater. 467 (2015) 82–88. doi:10.1016/j.jnucmat.2015.05.026.

[17] D.D. Keiser, M.A. Dayananda, Interdiffusion between U-Zr fuel vs selected cladding steels, Metall. Mater. Trans. A. 25 (1994) 1649–1653. doi:10.1007/BF02668530.

[18] D.D. Keiser, M.A. Dayananda, Interdiffusion between U-Zr fuel and selected Fe-Ni-Cr alloys, J. Nucl. Mater. 200 (1993) 229–243. doi:10.1016/0022-3115(93)90334-U.

[19] K. Huang, Y. Park, A. Ewh, B.H. Sencer, J.R. Kennedy, K.R. Coffey, Y.H. Sohn, Interdiffusion and reaction between uranium and iron, J. Nucl. Mater. 424 (2012) 82–88. doi:10.1016/j.jnucmat.2012.02.004.

[20] Y. Park, K. Huang, A. Paz y Puente, H.S. LEE, B.H. Sencer, J.R. Kennedy, Y.H. Sohn, Diffusional Interaction Between U-10 wt pct Zr and Fe at 903 K, 923 K, and 953 K (630 °C, 650 °C, and 680 °C), Metall. Mater. Trans. A. 46 (2015) 72–82. doi:10.1007/s11661-014-2277-2.

[21] C.T. Lee, H. Kim, T.K. Kim, C.B. Lee, Diffusion behavior in an interface between U–10Zr alloy and HT-9 steel, J. Nucl. Mater. 395 (2009) 140–144. doi:10.1016/j.jnucmat.2009.10.044.

[22] Y. Xie, M.T. Benson, L. He, J.A. King, R.D. Mariani, D.J. Murray, Diffusion behaviors between metallic fuel alloys with Pd addition and Fe, J. Nucl. Mater. 525 (2019) 111–124. doi:10.1016/j.jnucmat.2019.07.028.

[23] M. Kurata, T. Ogata, K. Nakamura, T. Ogawa, Thermodynamic assessment of the Fe–U, U–Zr and Fe–U–Zr systems, J. Alloys Compd. 271–273 (1998) 636–640. doi:10.1016/S0925-8388(98)00176-5.

[24] T. OGATA, K. NAKAMURA, M. KURATA, T. YOKOO, M.A. MIGNANELLI, Reactions between U-Pu-Zr Alloys and Fe at 923 K, J. Nucl. Sci. Technol. 37 (2000) 244–252. doi:10.1080/18811248.2000.9714890.

[25] M. Kurata, K. Nakamura, T. Ogata, Thermodynamic evaluation of the quaternary U–Pu–Zr–Fe

system – assessment of cladding temperature limits of metallic fuel in a fast reactor, J. Nucl. Mater. 294 (2001) 123–129. doi:10.1016/S0022-3115(01)00473-1.

[26] J.M. Harp, L. Capriotti, D.L. Porter, J.I. Cole, U-10Zr and U-5Fs: Fuel/cladding chemical interaction behavior differences, J. Nucl. Mater. 528 (2020) 151840. doi:10.1016/j.jnucmat.2019.151840.

[27] J.M. Harp, D.L. Porter, B.D. Miller, T.L. Trowbridge, W.J. Carmack, Scanning electron microscopy examination of a Fast Flux Test Facility irradiated U-10Zr fuel cross section clad with HT-9, J. Nucl. Mater. 494 (2017) 227–239. doi:10.1016/j.jnucmat.2017.07.040.

[28] A.E. Bridges, A.E. Waltar, R.D. Leggett, R.B. Baker, J.L. Ethridge, A Liquid-Metal Reactor Core Demonstration Experiment Using HT-9, Nucl. Technol. 102 (1993) 353–366. doi:10.13182/NT93-A17034.

[29] R.G. Pahl, D.L. Porter, C.E. Lahm, G.L. Hofman, Experimental studies of U-Pu-Zr fast reactor fuel pins in the experimental breeder reactor-ll, Metall. Trans. A. 21 (1990) 1863–1870. doi:10.1007/BF02647233.

[30] L.. Walters, Thirty years of fuels and materials information from EBR-II, J. Nucl. Mater. 270 (1999) 39–48. doi:10.1016/S0022-3115(98)00760-0.

[31] A.B. Cohen, H. Tsai, L.A. Neimark, Fuel/cladding compatibility in U-19Pu-10Zr/HT9-clad fuel at elevated temperatures, J. Nucl. Mater. 204 (1993) 244–251. doi:10.1016/0022-3115(93)90223-L.

[32] R.D. Mariani, D.L. Porter, T.P. O'Holleran, S.L. Hayes, J.R. Kennedy, Lanthanides in metallic nuclear fuels: Their behavior and methods for their control, J. Nucl. Mater. 419 (2011) 263–271. doi:10.1016/j.jnucmat.2011.08.036.

[33] R.S. Fielding, P.A. Hansen, T.A. Hyde, J. Maupin, Fabrication Report for the FY11 Phases of the AFC-3A and 3B Irradiation Experiments, Idaho Natl. Lab. Rep. (2011) INL/LTD-11-23158.

[34] T.P. O'Holleran, C.A. Papesch, L.N. Squires, T.A. Hyde, J.R. Kennedy, T. Hartmann, AFC-3 Fuel Characterization, Idaho Natl. Lab. Rep. (2012) INL/LTD-12-24346.

[35] G.S. Chang, R.G. Ambrosek, Hardening neutron spectrum for advanced actinide transmutation experiments in the ATR, Radiat. Prot. Dosimetry. 115 (2005) 63–68. doi:10.1093/rpd/nci167.

[36] J.M. Harp, S.L. Hayes, P.G. Medvedev, D.L. Porter, L. Capriotti, Testing Fast Reactor Fuels in a Thermal Reactor: A Comparison Report, Idaho Natl. Lab. Rep. (2017) INL/EXT-17-41677. doi:10.2172/1458766.

[37] P. Medvedev, S. Hayes, S. Bays, S. Novascone, L. Capriotti, Testing fast reactor fuels in a thermal reactor, Nucl. Eng. Des. 328 (2018) 154–160. doi:10.1016/j.nucengdes.2017.12.034.

[38] P.G. Medvedev, BISON Investigation of the Effect of the Fuel- Cladding Contact Irregularities on the Peak Cladding Temperature and FCCI Observed in AFC-3A Rodlet 4, Idaho Falls, ID (United States), 2016. doi:10.2172/1364503.

[39] William J. Carmack, Temperature and Burnup Correlated FCCI in U-10Zr Metallic Fuel, 2012. doi:10.2172/1055966.

[40] J.-O. Andersson, B. Sundman, Thermodynamic properties of the Cr-Fe system, Calphad. 11 (1987) 83–92. doi:10.1016/0364-5916(87)90021-6.

[41] W. Xiong, M. Selleby, Q. Chen, J. Odqvist, Y. Du, Phase Equilibria and Thermodynamic Properties in the Fe-Cr System, Crit. Rev. Solid State Mater. Sci. 35 (2010) 125–152.

doi:10.1080/10408431003788472.

[42] A. Jacob, E. Povoden-Karadeniz, E. Kozeschnik, Revised thermodynamic description of the Fe-Cr system based on an improved sublattice model of the σ phase, Calphad. 60 (2018) 16–28. doi:10.1016/j.calphad.2017.10.002.

[43] W. Xiong, P. Hedström, M. Selleby, J. Odqvist, M. Thuvander, Q. Chen, An improved thermodynamic modeling of the Fe–Cr system down to zero kelvin coupled with key experiments, Calphad. 35 (2011) 355–366. doi:10.1016/j.calphad.2011.05.002.

[44] O. Anderoglu, J. Van den Bosch, P. Hosemann, E. Stergar, B.H. Sencer, D. Bhattacharyya, R. Dickerson, P. Dickerson, M. Hartl, S.A. Maloy, Phase stability of an HT-9 duct irradiated in FFTF, J. Nucl. Mater. 430 (2012) 194–204. doi:10.1016/j.jnucmat.2012.06.038.

[45] C. Zheng, E.R. Reese, K.G. Field, E. Marquis, S.A. Maloy, D. Kaoumi, Microstructure response of ferritic/martensitic steel HT9 after neutron irradiation: effect of dose, J. Nucl. Mater. 523 (2019) 421–433. doi:10.1016/j.jnucmat.2019.06.019.

[46] E.R. Reese, M. Bachhav, P. Wells, T. Yamamoto, G. Robert Odette, E.A. Marquis, On α′ precipitate composition in thermally annealed and neutron-irradiated Fe- 9-18Cr alloys, J. Nucl. Mater. 500 (2018) 192–198. doi:10.1016/j.jnucmat.2017.12.036.

[47] J.M. Harp, L. Capriotti, F. Cappia, Baseline Postirradiation Examination of the AFC-3C, AFC-3D, and AFC-4A Experiments, Idaho Falls, ID (United States), 2018. doi:10.2172/1498255.

Fuel-cladding chemical interaction of a prototype annular U-10Zr fuel with Fe-12Cr ferritic/martensitic HT-9 cladding

Xiang Liu[a,*], Luca Capriotti[a,*], Tiankai Yao[a,*], Jason M. Harp[b], Michael T. Benson[a], Yachun Wang[a], Fei Teng[a], Lingfeng He[a]

[a]*Idaho National Laboratory, Idaho Falls, ID 83415, USA*
[b]*Oak Ridge National Laboratory, Oak Ridge, TN 37831, USA*

[*]Corresponding authors
Email addresses: Xiang.liu@inl.gov (X.Liu), Luca.Capriotti@inl.gov (L. Capriotti), tiankai.yao@inl.gov (T. Yao)

Abstract

Solid metallic fuels have been traditionally used in sodium-cooled fast reactors. However, the sodium bond used in solid fuels complicates the fuel fabrication and back-end fuel cycle processes. As an alternative fuel form, the annular metallic fuel design with helium bond is being investigated to eliminates the liquid sodium bond between the fuel and the cladding. The fuel-cladding chemical interaction (FCCI) of annular fuel also presents features different from sodium bonded solid fuel. Here, state-of-the-art electron microscopy and spectroscopy techniques were used to study the FCCI of a prototype annular U-10wt%Zr (U-10Zr) fuel with ferritic/martensitic HT-9 cladding irradiated to 3.3% fission per initial heavy atom. Compared with sodium-bonded solid fuels, negligible amounts of lanthanides were found in the FCCI layer in the investigated helium-bonded annular fuel. Instead, most lanthanides were retained in the Zr-rich phase in the fuel center region. The interdiffusion of iron and uranium resulted in tetragonal (**U**,Zr)$_6$Fe phase (space group I4/mcm) and cubic (**U**,Zr)(**Fe**,Cr)$_2$ phase (space group Fd$\bar{3}$m). The (**U**,Zr)(**Fe**,Cr)$_2$ phase contains a high density of voids and intergranular uranium monocarbides of NaCl-type crystal structure (space group Fm$\bar{3}$m). At the interdiffusion zone and inner cladding interface, a porous lamellar structure composed of alternating Cr-rich layers and U-rich layers was observed. Next to the lamellar region, unexpected phase transformation from body-centered cubic ferrite (α-Fe) to tetragonal binary Fe-Cr σ phase (space group P4$_2$/mnm) occurred, and tetragonal Fe-Cr-U-Si phase (space group I4/mmm) was identified. Due to the diffusion of carbon into the interdiffusion zone, carbon depletion inside the HT-9 led to the disappearance of the martensite lath structure, and intergranular U-rich carbides formed as a result of the diffusion of uranium into the cladding. These findings reveal the unique FCCI behavior of annular U-Zr fuels, which could be a promising alternative fuel form for high burnup fast reactor applications.

Keywords: Fuel-cladding chemical interaction (FCCI); metallic fuel; advanced nuclear fuel; transmission electron microscopy (TEM); HT-9 cladding; phase transformation.

---

1. Introduction

Sodium-cooled fast reactors (SFR) is one of the advanced reactor designs that have been successfully built and operated globally [1]. One goal of current SFR fuel design is to develop technologies that enable the expanded deployment of SFR technology for different applications. Three possible applications of SFR

technology are actinide management, process heat, and once-through fuel for power or test reactor applications [2].

Metallic U-Zr alloy fuels are candidate fuel types for SFR [3–6]. Irradiation-induced swelling [7], fission gas release [8], and fuel-cladding chemical interaction (FCCI) [9,10] are key limiting factors that restrict fuel performance at high burnup. Historically, SFR fuel designs were adapted to mitigate the challenges posed by swelling and fission gas release. A low smear density was employed to accommodate the rapid swelling and avoid premature mechanical failure of the cladding. A relatively large volume gas plenum was used to accommodate the released fission gas. Limitations on the peak inner cladding temperature of fuel pins below 625 °C were historically used to mitigate FCCI. However, this limited the maximum outlet temperature of SFR to between 500–550 °C, which excludes SFR use from many potential process heat applications [11]. Annular metallic fuel that is sodium free is an exemplary technology that can help enable once-through fuel scenarios.

Swelling in metallic fuel can be accommodated in many ways [12]. Most often, it was accommodated by placing a solid fuel into a larger cladding tube and filling the space between with a high thermal conductivity liquid, like sodium. However, sodium-bonded spent fuels are considered mixed hazardous waste in a once-through fuel cycle and require a costly sodium removal process prior to disposal [13]. As a possible alternative to the historical solid U-Zr fuels, annular U-Zr fuels are being evaluated. In the annular U-Zr fuel design shown in Figure 1, the small gap between the fuel and the cladding allows helium to be used as the bonding material, eliminating the hazards associated with sodium. However, because of the differences in bonding material and fuel design, the FCCI behavior of these annular U-Zr fuels could be very different from historical solid U-Zr fuels.

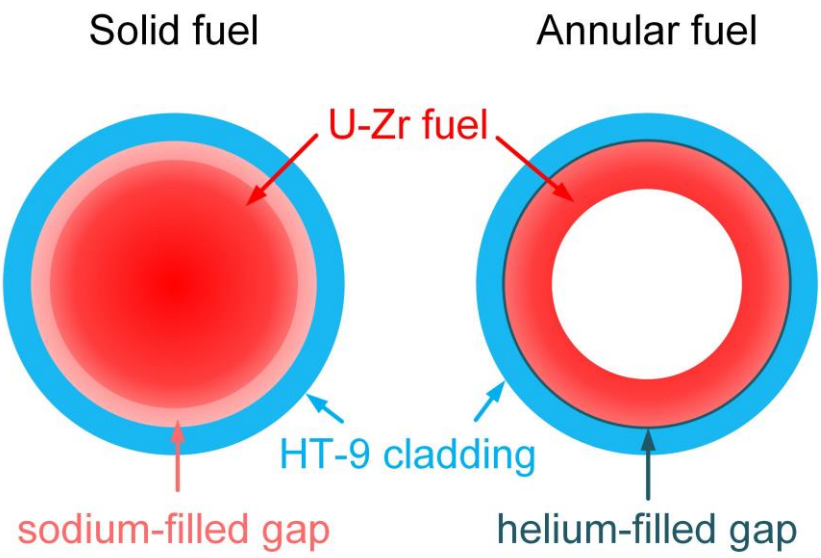

Figure 1. Illustration of the differences in the design of sodium-bonded solid fuel versus helium-bonded annular fuel.

Metallic fuel FCCI can involve both fission products interaction with cladding and interaction between the primary fuel elements and the cladding. On one hand, as the lanthanide fission products diffuse down the thermal gradient and interact with cladding constituents, a brittle wastage zone along the inner surface of the cladding is formed [14]. This wastage zone poses threats to the mechanical integrity of the cladding. On the other hand, the diffusion of iron into the fuel can form low melting eutectic phases and potentially

lead to fuel melting. For instance, two representative phases found in U-Zr fuel with Fe base cladding interdiffusion studies [15–22] are U_6Fe and UFe_2, the melting points of which are ~1102 K and ~1504 K, respectively [23]. The melting point can be further lowered by the addition of plutonium in U-Pu-Zr fuels [24,25]. Direct interaction between cladding elements and fuel was also observed in the irradiation experience of U-5Fs alloys [26].

Previous studies found that Zr-rich regions (Zr-rind) at the fuel periphery could act as diffusion barriers to reduce FCCI, and the Zr-rind was assumed to be a result of impurities during fuel fabrication [9]. Zr liners were then proposed as one approach to mitigate FCCI.

The vast majority of existing irradiated metallic alloy fuel pins from past U.S. fast reactor fuel research programs were composed of U-10wt% Zr (U-10Zr) fuel sodium bonded to HT-9 cladding with a smear density of ~75% [5,27] to accommodate fuel swelling. The liquid sodium bond was chosen to ensure efficient heat transfer from the fuel to the cladding. HT-9 is a Fe-12Cr base ferritic/martensitic alloy that shows excellent swelling resistance and compatibility with metallic fuels [28–30]. The FCCI of HT-9 cladding with U-Zr and U-Pu-Zr fuels were investigated in previous scanning electron microscopy (SEM) [14,27,31] and electron micro probe analyzer (EPMA) [14] studies, and it was found that lanthanides penetrated into the cladding and iron diffused into the fuel. Previous studies [9,32] also proposed that the transport of lanthanides could be through liquid-like diffusion via interconnected pores filled with sodium and cesium. The liquid sodium bond used in historical solid U-Zr fuels might have played an important role in the transportation of lanthanides to the FCCI region.

In this study, the FCCI behavior of an sodium-free helium-bonded annular U-10Zr fuel with HT-9 cladding was investigated in detail for the first time, utilizing the recently available advanced electron microscopy and spectroscopy capabilities for highly radioactive samples at the Materials and Fuels Complex (MFC), Idaho National Laboratory (INL). The results shed light on the unique FCCI behavior of annular U-10Zr fuel, which could be a promising fuel type for SFR applications.

2. Experimental

2.1 Materials

The investigated fuel is an annular U-10Zr fuel from the Advanced Fuels Campaign (AFC) series (AFC-3A) of irradiation experiments. As part of the AFC-3A irradiation, this fuel rodlet was designated AFC-3A R4, and the corresponding fuel fabrication was described in Fielding *et al.* [33], and pre-irradiation characterization was reported in O'Holleran *et al.* [34]. Post-irradiation examination (PIE) data and the overall irradiation performance of AFC-3A and AFC-3B fuels were discussed in a recent study [13].

The AFC-3A R4 fuel rodlet has a nominal composition of U-10wt%Zr. The rodlet is in the annular fuel form with an inner diameter of 3.25 mm, an outer diameter of 4.86 mm, and a total height of 38.0 mm. The nominal smear density is 55%, and the as-fabricated smear density is 53.8%. Helium was used as the bonding material. The fuel alloy was fabricated by mixing uranium and zirconium metals in an arc melter and homogenized through several melts, followed by injection casting into a quartz mold with an inner quartz core. After casting, the inner quartz core was removed by drilling, and the outside mold was removed by breaking the quartz off the outside of the cast pin. The fuel slug was then cut into the desired length for irradiation testing. Some fabrication imperfections were observed for this annular U-10Zr fuel pin. Specifically, an oversized inner capsule tube diminishes the fuel outer diameter and leads to a generally large fuel cladding gap (> 50 μm) prior to irradiation. A lack of final machining step causes rough surfaces and localized contact between fuel and cladding during irradiation. Furthermore, the capsule tube inner

diameter was not concentric with the outer diameter due to poor cylindricity, which led to circumferential variations of the fuel pin.

2.2 Neutron irradiation

The as-fabricated annular U-10Zr fuel was sealed inside ferritic/martensitic steel HT-9. The cladding had an outer diameter of 5.842 mm and a wall thickness of 0.4445 mm. The HT-9 steel used in this work was from legacy EBR-II cladding. Although the heat treatment information for this specific cladding tube was not available, information from similar EBR-II Mark-IV driver fuel HT-9 cladding show that these cladding tubes met the grade UNS Designation S42100 and ASTM A771–83 requirements. All the HT-9 cladding tubes were manufactured by the Carpenter Technology Corporation. The HT-9 tubes were cold drawn 20±5 %, followed by adequate annealing at 2035 ºF (1113 ºC) and tempering at 1200–1300 ºF for two hours and rapid cooling. The final tempered martensitic microstructure has an ASTM grain size number of 7–9. The nominal chemical composition of the HT-9 cladding tube is listed in Table 1.

Table 1. Nominal chemical composition of the HT-9 cladding tube.

Element	Fe	C	Mn	P	S	Si	Ni	Cr	Mo	Cu	V	Co	W
wt%	Bal.	0.22	0.56	0.13	0.002	0.30	0.57	11.53	1.08	0.02	0.31	0.02	0.52
at%	Bal.	1.007	0.56	0.23	0.003	0.587	0.534	12.19	0.619	0.017	0.335	0.0187	0.1555

The rodlet was sealed inside a cylindrical capsule container that served as the primary boundary between the rodlet and the coolant. The capsules were back-filled with helium gas. The temperature of the rodlets is controlled by the gap between the rodlets and the capsule and by the enrichment level of the fuel.

The investigated annular fuel was part of the AFC-3 irradiation experiments, which were performed at the INL Advanced Test Reactor (ATR). The AFC capsules were irradiated in a cadmium-shrouded position that hardens the ATR neutron spectrum to create a radial power profile appropriate for fast spectrum fuel testing [35–37]. Detailed description of the irradiation experiment setup can be found in recent works [13,36]. The irradiation history, including the linear heat generation rate (LHGR, in unit of W/cm) and peak inner cladding temperature (PICT) of each effective full-power day (EFPD), is plotted in Figure 2. As mentioned in a previous AFC-3 study [13], the PICT was calculated from the LHGR and assumed as-built dimensions of the rodlets and capsules.

The effect of fuel cladding gaps/contacts on PICT was simulated by BISON fuel performance code [38] and found to be insignificant with only a 12 ℃ increase of PICT at maximum compared with nominal sodium bonded U-10Zr metallic fuel. However, cladding temperature variation/gradient shows stronger depends on irregularities of fuel cladding gaps/contacts. For example, the elliptical fuel shape and the single point fuel cladding contact during irradiation leads to a maximum temperature of 592 ºC at the contact but a much lower temperature of 528 ºC distant from the contact. The effects of large and small voids at a scale relevant to the microscopy observation (Figure 3) will leads to a temperature variation of 509 ºC–587 ºC and 566 ºC–597 ºC, respectively. Based on these numbers, the uncertainty of the cladding temperature should be within 15 %.

The initial enrichment level of the AFC-3A R4 rodlet was 45 wt.% U-235. The AFC-3A and 3B irradiation lasted for about 120 EFPD. The burnup of the AFC-3A R4 rodlet was determined to be 3.3% fission per initial heavy metal atom (FIMA), and the fission density was about 8.91×10^{20} fission/cm^3.

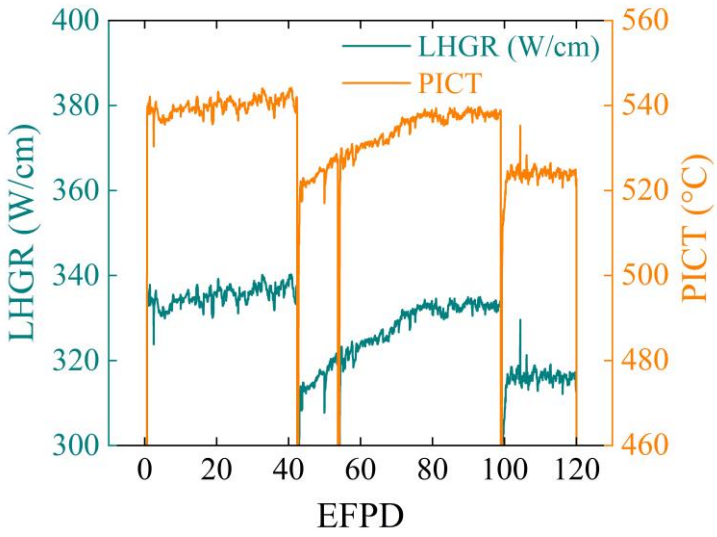

Figure 2. Peak inner cladding temperature (PICT) and linear heat generation rate (LHGR) for each effective full-power day (EFPD) for the AFC-3A R4 rodlet.

2.3 Post-irradiation electron microscopy characterization

The electron microscopy characterization of the irradiated fuel was performed at the Electron Microscopy Laboratory (EML) and the Irradiated Materials Characterization Laboratory (IMCL) at Idaho National Laboratory (INL). A JEOL JSM-7000F field emission gun (FEG) scanning electron microscope (SEM) equipped with energy dispersive X-ray spectroscopy (EDS) was used for the initial microstructure characterization. Figure 3 shows the overall microstructure of irradiated annular U-10Zr fuel with HT-9 cladding.

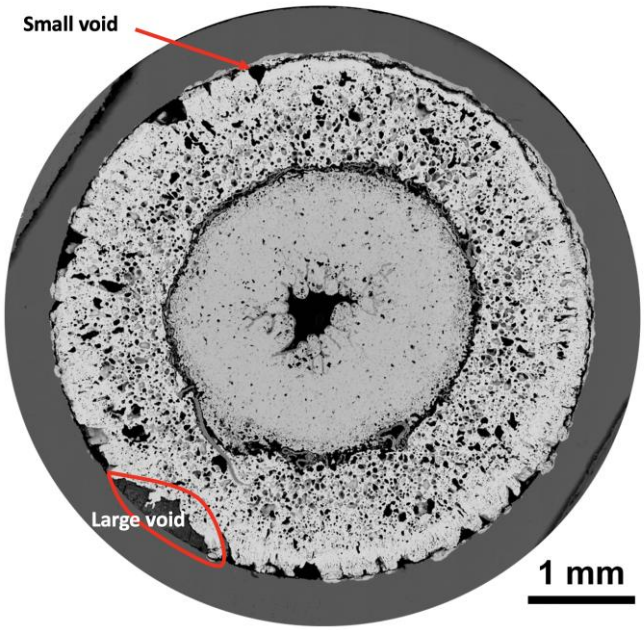

Figure 3. Montage created from a set of SEM images showing the overall microstructure of a cross section of the irradiated annular U-10Zr fuel.

Following the SEM characterization, a FEI Quanta 3D scanning electron microscope/focused ion beam (SEM/FIB) was used to prepare the transmission electron microscopy (TEM) lamellae. After lift-out, the TEM lamellae were mounted onto Cu grids and thinned to a thickness of ~100 nm using 30 keV Ga ions with decreasing ion beam current. The final thinning current was about 100 pA. To minimize FIB-induced damage, the lamellae were polished by 5 keV Ga ions for ~2 min and 2 keV Ga ions for ~4 min. TEM and scanning transmission electron microscopy with energy dispersive X-ray spectroscopy (STEM-EDS) characterization was carried out on a Thermo Scientific Talos F200X field emission gun (FEG) scanning/transmission electron microscope (S/TEM) equipped with ChemiSTEM™ and operated at 200 kV. STEM-EDS was used for elemental mapping and composition analysis. All EDS quantifications were performed using the Thermo Scientific Velox™ software using the default Brown-Powell ionization cross-section model and multi-polynomial model for background correction. TEM diffraction patterns and STEM-EDS results were used together for phase identification.

3. Results

As shown in Figure 3, the dimensions of the cladding and the outer diameter of the irradiated fuel were similar to the unirradiated condition. However, the originally empty center region of the annular fuel is now filled with a new phase. As discussed in a recent PIE study on the AFC-3 fuels [13], this annular fuel grew inward, and the center region seemed more resistant to oxidation than the outer region, suggesting constituent redistribution and higher Zr concentration in the center region.

To gain insight into the elemental distribution in the irradiated fuel, large area SEM-EDS mapping was performed from the center region of the fuel all the way into the cladding, as shown in Figure 4. The U and Zr distribution show that the fuel region is composed of two different phases: a Zr-rich phase at the center region and a U-rich phase at the outer region. A (Zr, Si)-rich layer was found between these two phases, and Si was believed to be from the quartz mold used during fuel fabrication. Chromium was almost exclusively found inside the cladding, indicating no Cr diffusion into the fuel. However, as shown in Figure 4 (d), Fe was found diffused into the fuel. The fuel and the cladding were not in good contact at the chosen EDS mapping region and almost no U was found in the cladding, as shown in Figure 4 (b).

The most surprising result shown in Figure 4 is the distribution of neodymium, which is the most representative element of lanthanides. Nd was mostly retained in the Zr-rich phase at the fuel center, as shown in Figure 4 (c). This is very different from the lanthanide behavior in irradiated solid U-Zr fuels in which the lanthanides were mostly found in the FCCI region [14,27,39].

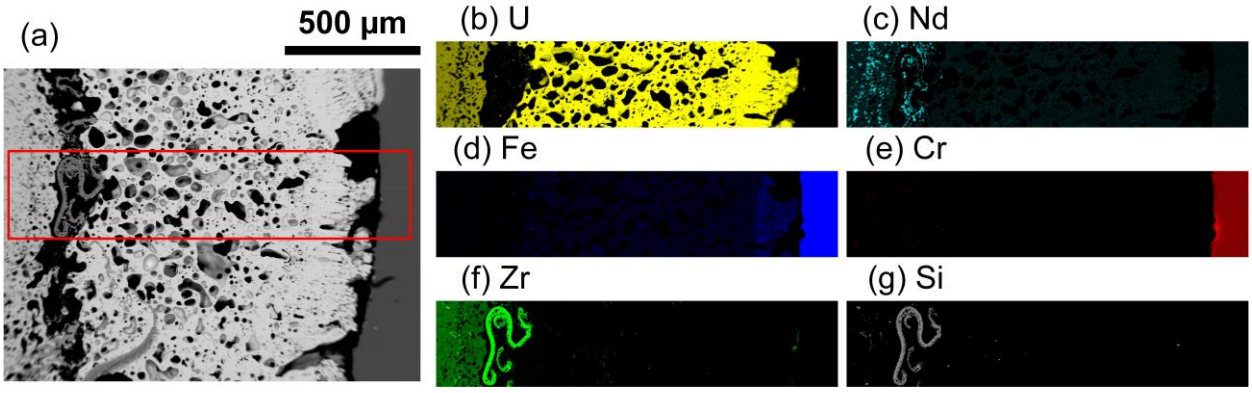

Figure 4. SEM-EDS results showing the overall elemental distribution from the fuel center to the cladding: (a) SEM image, (b)–(g) raw intensity maps of U, Nd, Fe, Cr, Zr, and Si of the region marked by solid red lines in (a).

The fuel came into contact with the cladding and reacted at multiple locations, as shown in Figure 3. To further investigate the detailed microstructure of the FCCI region, two TEM lamellae, lamella #1 and lamella #2, were lifted out from a location that showed significant fuel-cladding contact. The SEM images at different magnifications in Figure 5 shows the locations of the TEM lift-outs. As shown in the high-magnification SEM image in Figure 5 (d), four distinct areas were identified in the wastage zone inside the cladding: Region I inside the interdiffusion zone, Region II at the interface of the interdiffusion zone and the inner cladding, Region III on the cladding side of the interface, and Region IV from the bulk cladding region. The interdiffusion zone-inner cladding interface is basically composed of two thin regions with distinct microstructures: one with a lamellar structure (Region II) and the other (Region III) with two different contrasts (light grey and dark grey). Lamella #1 was lifted out from a region inside the fuel but near the cladding, as shown in Figure 5 (b). Lamella #2 covers all four regions in the wastage zone, as shown in Figure 5 (c)–(d).

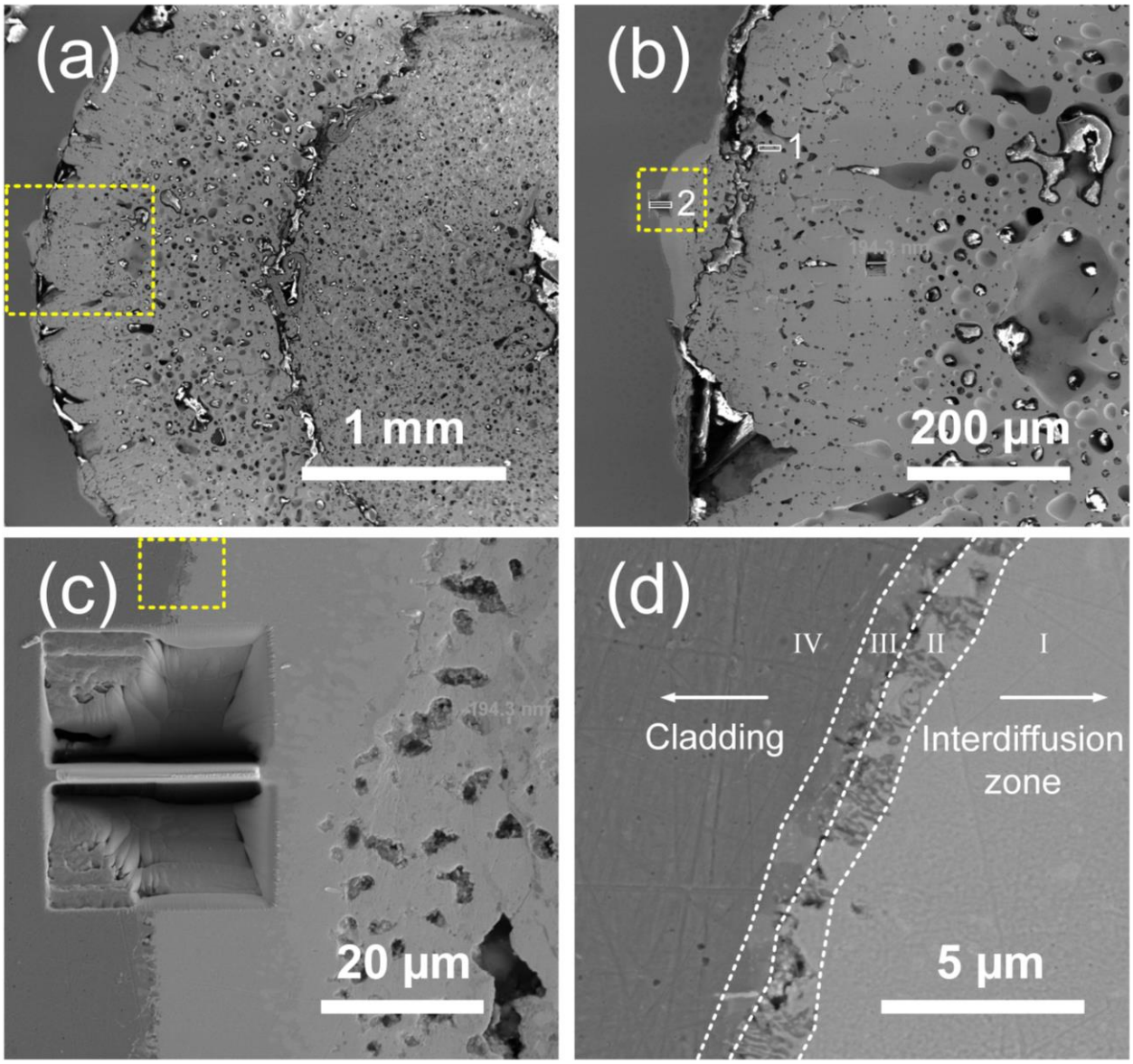

Figure 5. (a)–(d) SEM images at different magnifications showing the microstructure of the FCCI region and the location of the lift-out. Rectangular areas marked by dotted yellow lines indicate the area of the next SEM image. Two lamellae marked as 1 and 2 in (b) were studied in present work.

Before TEM characterization, SEM-EDS mapping was performed at one of the regions that showed good fuel-cladding contact, and an example result is shown in Figure 6. At the fuel-cladding interface, the SEM image and the elemental maps show a lamellar structure similar to the Region II in Figure 5 (d).

It should also be noted that in the SEM images and elemental maps in Figure 6, precipitates which were later confirmed to be U-rich carbides were found at the grain boundaries of the HT-9 grains, as indicated by the red arrows. Most of the precipitates were located inside the light-blue band in Figure 6 (b). A few precipitates were found in the cladding further away from the FCCI interface.

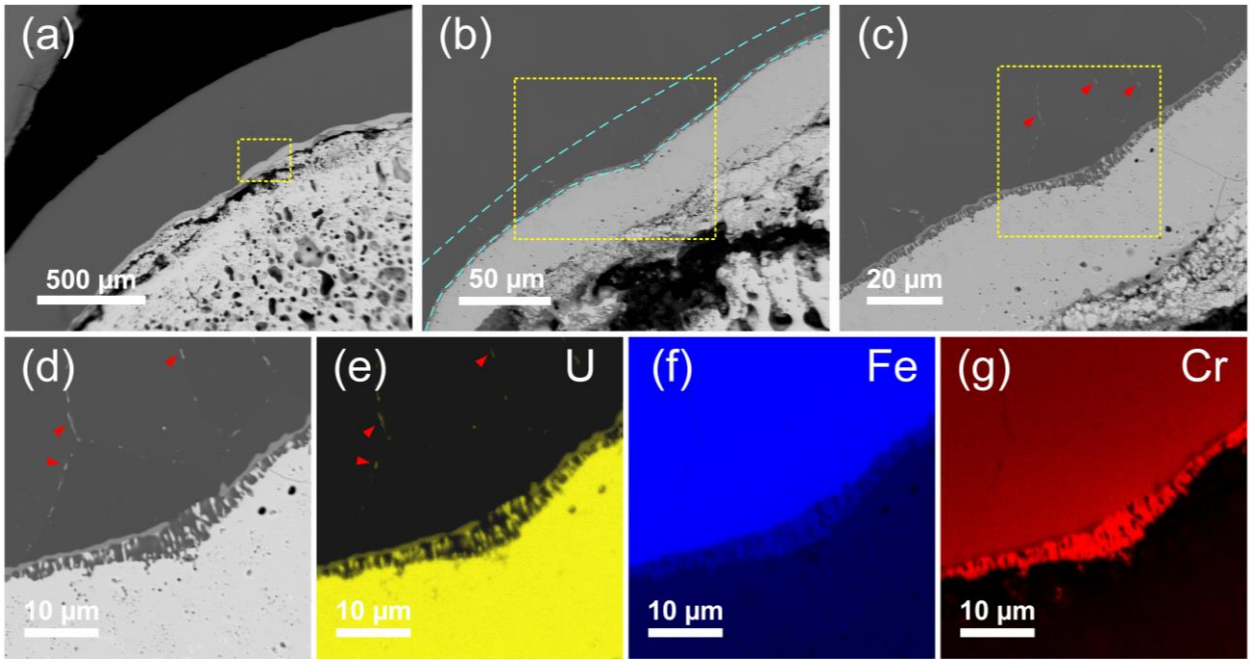

Figure 6. SEM images and EDS mapping showing the microstructure and elemental distribution at the fuel-cladding interface: (a)–(d) SEM images at different magnifications, with the rectangular areas marked by dotted yellow lines indicate the area of the next SEM image; (e)–(g) Elemental maps of U, Fe, and Cr of the region in (d). Red arrows in (c)–(e) indicate the U-rich precipitates at the grain boundaries of HT-9 cladding, and the dashed blue lines in (b) indicate the region where the U-rich precipitates were found.

TEM was then used to reveal details of the microstructure near the FCCI region. Figure 7 shows the STEM-EDS results of lamella #1 lifted out near the edge of the fuel. As shown in the elemental maps in Figure 7 (b)–(d), two phases, one Zr-rich and one (U,Fe)-rich, were found in this lamella. The noticeable Fe signal inside lamella #1 suggests the diffusion of Fe into the fuel. The EDS spectra of the (U,Fe)-rich phase and the Zr-rich phase are shown in Figure 7 (e) and (f), respectively. Based on the spectra, the composition of the Zr-rich phase was measured to be ~96 at% Zr and ~2.4 at% U. The composition of the (U,Fe)-rich phase was measured to be ~77 at% U, ~4 at% Zr, and ~14 at% Fe, very close to the composition of the U_6Fe phase identified in previous U-Fe diffusion couple studies [15–22].

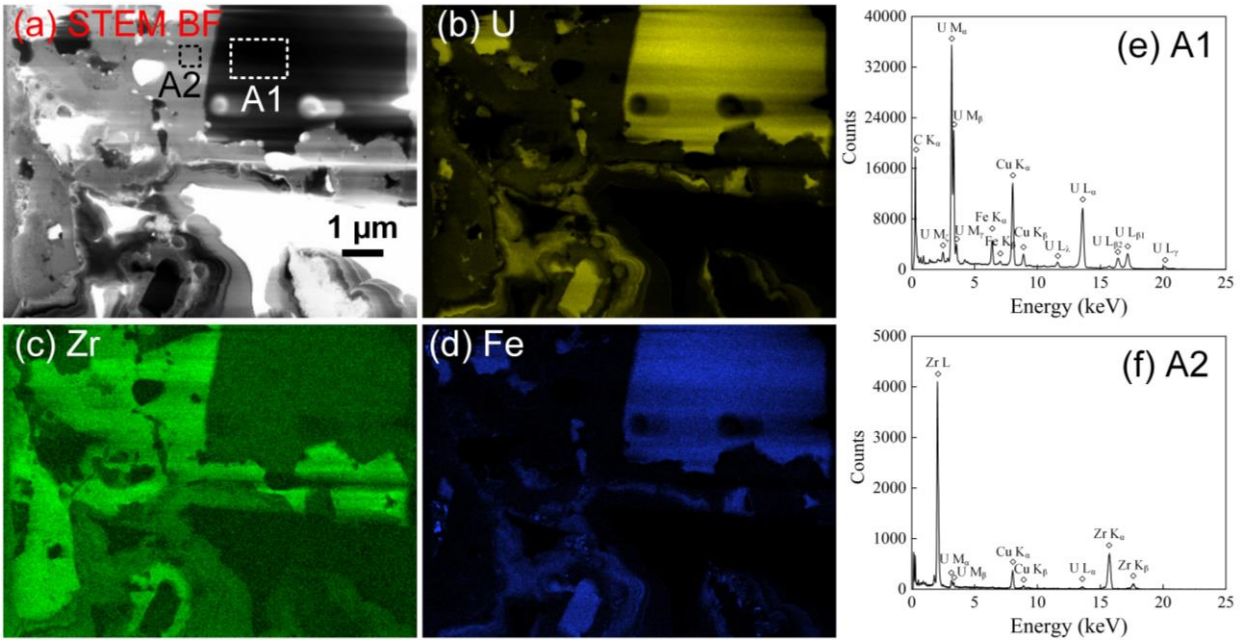

Figure 7. STEM EDS results of lamella #1: (a) STEM bright-field (BF) image, (b)–(d) raw intensity maps of U, Zr, and Fe, (e) EDS spectrum of area A1 marked in (a), (f) EDS spectrum of area A2 marked in (a). The Cu K_α and K_β peaks are background signals from the Cu grid.

To confirm the crystal structure of the (U,Fe)-rich phase, TEM diffraction patterns were acquired, and the results are shown in Figure 8. Indeed all the diffraction patterns from this (U,Fe)-rich phase matched well with the standard tetragonal U_6Fe phase, as shown by the indexed results in Figure 8 (b)–(d). Therefore, the composition and the crystal structure confirms that this (U,Fe)-rich phase is U_6Fe (space group I4/mcm), or more precisely (**U**,Zr)$_6$Fe (bold symbols indicate the dominant elements).

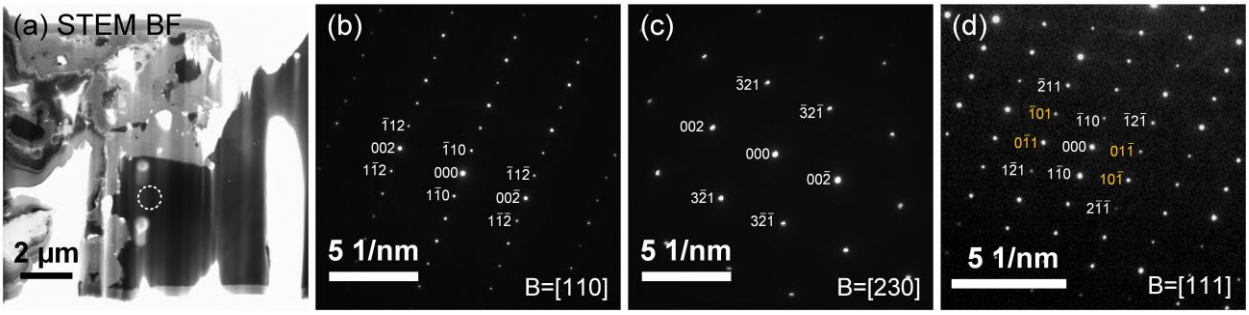

Figure 8. TEM results of the (**U**,Zr)$_6$Fe: (a) STEM BF image, (b)–(d) diffraction patterns of the area marked by dashed white lines in (a), taken at different zones. Yellow labels indicate double diffraction spots.

Lamella #2 was lifted out inside the wastage zone (Figure 5) and has a much more complex microstructure. Figure 9 displays the overall microstructure of the FCCI region contained in TEM lamella #2. Using the same convention as Figure 5 (d), the lamella can be divided into four regions: Region I inside the interdiffusion zone, Region II and III at the interface of the interdiffusion zone and the inner cladding, and Region IV from the cladding region. Region I is marked by fine grains with a high density of nano-sized voids. Region II contains the lamellar structure. Region III is featured by small grains and fine precipitates. Region IV contains relatively large grains with little voids or porosity. The interface region (Regions II and III) is very porous.

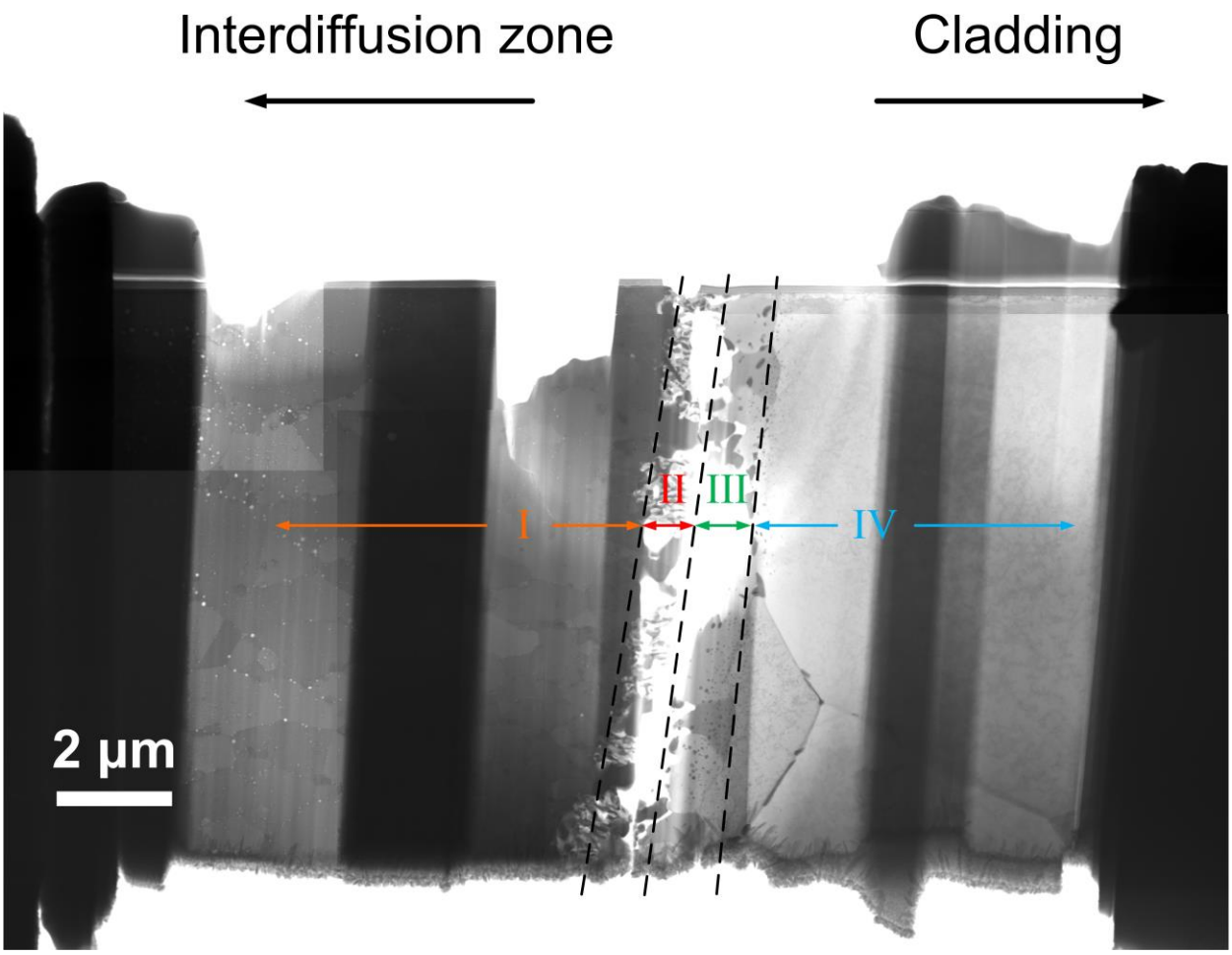

Figure 9. STEM BF image showing the overall microstructure of the FCCI region.

Figure 10 shows the STEM-EDS results of an area inside Region I. The elemental maps show that the matrix of Region I contains U, Fe, and Cr. Uranium carbide precipitates were frequently found in Region I. Figure 10 (g) and (h) also show the EDS spectrum of the uranium carbide (spot 1) and the matrix (spot 2), respectively.

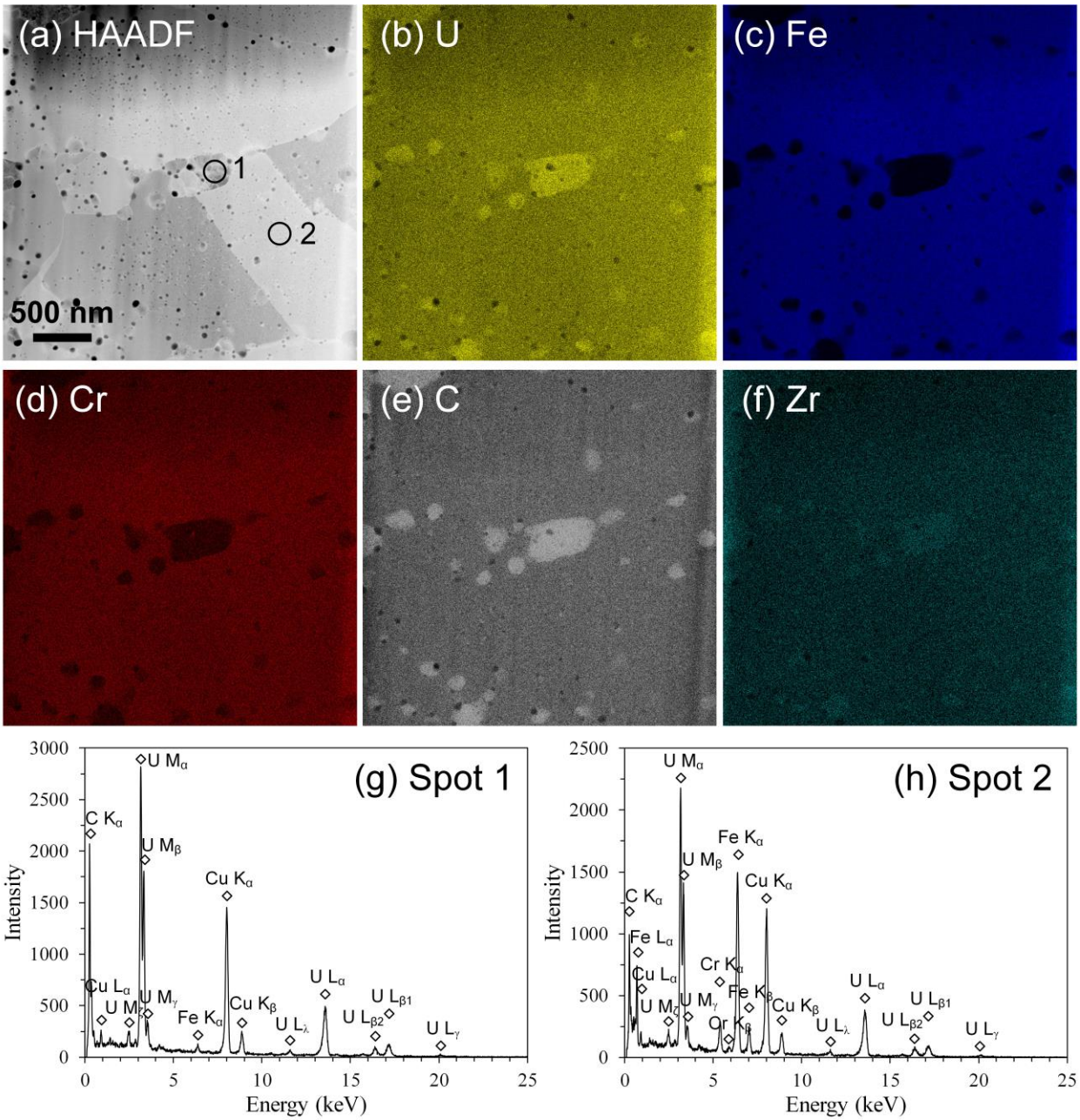

Figure 10. STEM-EDS results of Region I: (a) HAADF image, (b)–(f) raw intensity maps of U, Fe, Cr, C, and W, respectively, (g) EDS spectrum of spot 1 shown in (a), and (h) EDS spectrum of spot 2 shown in (a).

The EDS measurements showed that the matrix in Region I contained about 58.5 at% Fe, 28.1 at% U, 10.0 at% Cr, and 1.2 at% Zr. The (Fe,Cr):(U,Zr) ratio was close to 2:1, which is consistent with the UFe_2 phase. Since U and Fe are the dominant elements, it should be identified as (**U**,Zr)(**Fe**,Cr)$_2$, in which bold symbols indicate the dominant elements.

TEM diffraction patterns were taken to confirm the crystal structure of the matrix in Region I, and the results are shown in Figure 11. Two diffraction patterns (Figure 11 (b) and (c)) were taken and they both matched the UFe_2 phase (space group $Fd\bar{3}m$) perfectly, confirming that the crystal structure of this

(**U**,Zr)(**Fe**,Cr)$_2$ phase is the same as that of the UFe_2 phase that was reported in previous U-Zr and Fe diffusion couple studies [15–17,19–21].

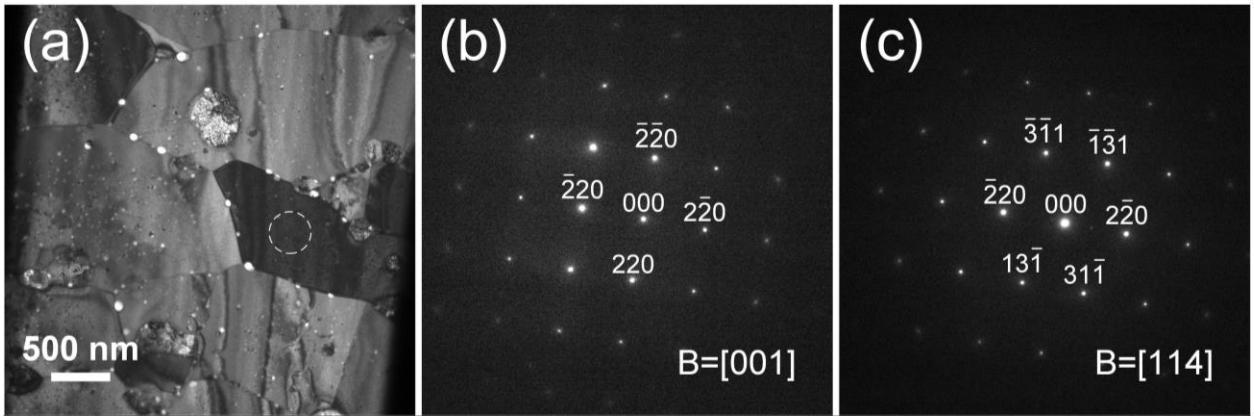

Figure 11. (a) TEM BF image showing the microstructure in Region I, (b) and (c) diffraction patterns taken from the area indicated by the dashed circle in (a).

To confirm the crystal structure of the U-rich carbides in the (**U**,Zr)(**Fe**,Cr)$_2$ phase, TEM diffraction patterns were taken at several different zones. The three diffraction patterns shown in Figure 12 (b)–(d) match perfectly with the [001], [011], and [013] zones of uranium monocarbide (UC) of the NaCl-type crystal structure (space group $Fm\bar{3}m$), respectively. Thus, these U-rich carbides were confirmed to be UC.

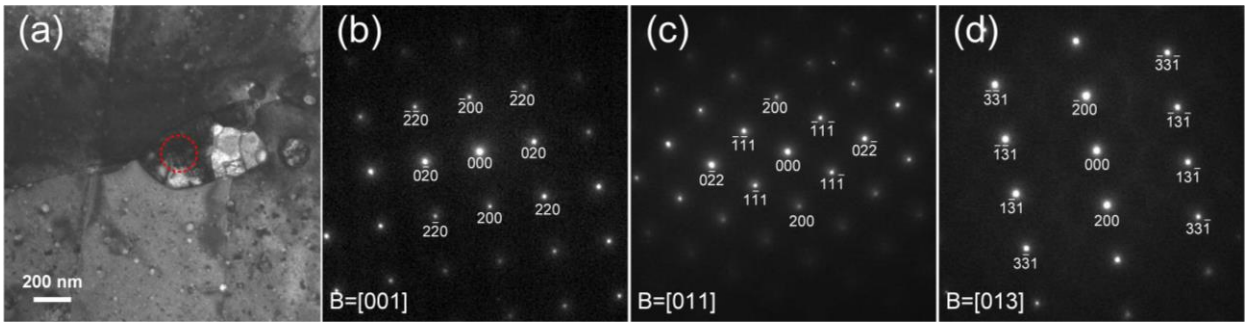

Figure 12. (a) TEM BF image of an intergranular U-rich carbide, (b)–(d) diffraction patterns of the carbide highlighted in (a) at different zone axes. The diffraction patterns confirm the U-rich carbides are uranium monocarbide with a NaCl-type structure.

Details of the microstructure of the (**U**,Zr)(**Fe**,Cr)$_2$ phase are shown in Figure 13. Overall, the (**U**,Zr)(**Fe**,Cr)$_2$ phase contains a high number density of voids, suggesting that this intermetallic phase is prone to irradiation induced swelling. The voids inside grains are generally smaller and some larger voids are located at the interfaces of the uranium carbides. In addition, as shown in the high-magnification STEM BF image in Figure 13 (d) and the corresponding elemental maps in Figure 13 (e)–(h), the voids inside the grains are mostly coupled with small uranium carbide precipitates.

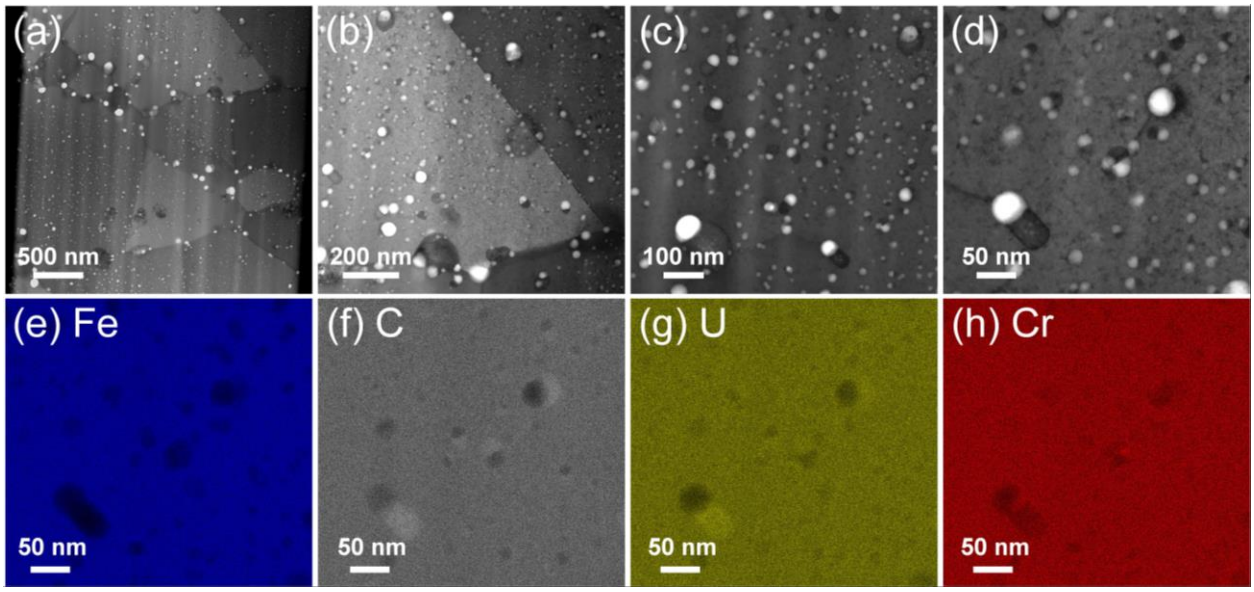

Figure 13. Microstructure of Region I: (a)–(d) STEM BF images of different magnifications, (e)–(h) raw intensity maps of Fe, C, U, and Cr, respectively.

Figure 14. displays the detailed STEM-EDS results of the interaction region. From the high angle annular dark field (HAADF) image in Figure 14 (a) and elemental maps in Figure 14 (b)–(f), it is clear that the interaction region is featured by lamellar structures, uranium carbides, high porosity, and localized distribution of cesium. The lamellar structure is composed of alternating U-rich lamellae and Cr-rich lamellae with a typical width of about 160 nm.

The compositional difference of different regions is more clearly seen in the linescan shown in Figure 14 (g), from which four different regions corresponding to Region I, II, III, and IV are easily identified. From the elemental maps in Figure 14 (b)–(e) show that uranium is mostly found in Region I and Region II, with some U-rich carbides in region III, indicating diffusion of uranium into the cladding. Figure 14 (e) shows that carbon is mostly distributed in Regions I and II, suggesting significant diffusion of carbon into the wastage zone. Figure 14 (d) shows that Regions II and III contain significant amount of chromium, and only limited amount of chromium is found in Region I. It should be noted that some residual cesium was found in Regions II and III, the interface of the interdiffusion zone and the cladding. Since cesium is highly reactive, the actual amount of cesium at the interface before mechanical polishing could be much higher.

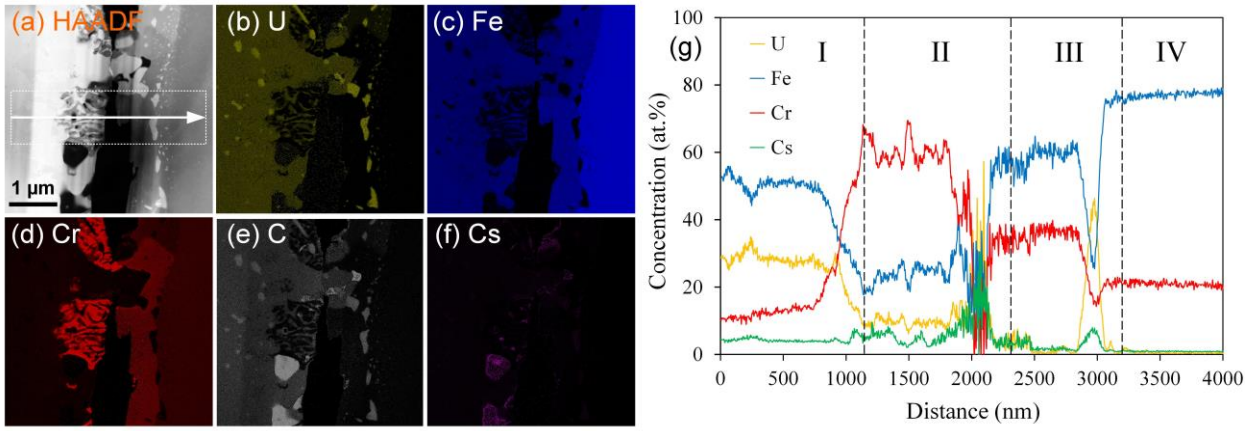

Figure 14. STEM-EDS results of the interaction region: (a) STEM HAADF image, (b)–(f) elemental at.% maps (after quantification) of U, Fe, Cr, C, and Cs, respectively, (g) EDS linescan across the rectangular area marked by dotted white lines in (a).

From the Cr map in Figure 14 (d) and also the EDS linescan in Figure 14 (g), it is apparent that there are noticeable fluctuations in the Cr concentration in both Region II and Region III. The fluctuation in Region II is apparently due to the lamellar structure. The U-rich lamellae are due to the diffusion of uranium into the cladding, and the Cr-rich lamellae are most likely due to the depletion of Fe and the very low solubility of Cr in U.

A closer look into Region III provides some information as to why Region III is also showing concentration fluctuation. Figure 15 shows higher magnification EDS results focusing on Region III. As shown in Figure 15 (a), areas A1, A2, and A3 are inside Region III, and area A4 is in Region IV. The STEM BF image in Figure 15 (a) and elemental maps in Figure 15 (b)–(i) show that there are two different phases in Region III: areas A1 and A3 seem to be one phase with higher Cr concentration, whereas area A2 seems to be a different phase with a lower Cr concentration and also contains some amount of U, Si, Ni, Mo, and W. The compositional differences of these two different phases is also seen from the EDS spectra in Figure 15 (j)–(k), and more quantitatively from the EDS linescan across areas A1 and A2 in Figure 15 (m). From the EDS results, it was confirmed that one phase contained almost only Fe (~59.5 at%) and Cr (~30.8 at%), whereas the other phase contained Fe (~64.0 at%), Cr (~16.4 at%), U (~8.2 at%), Si (~2.3 at%), and Mo (~4.1 at.%).

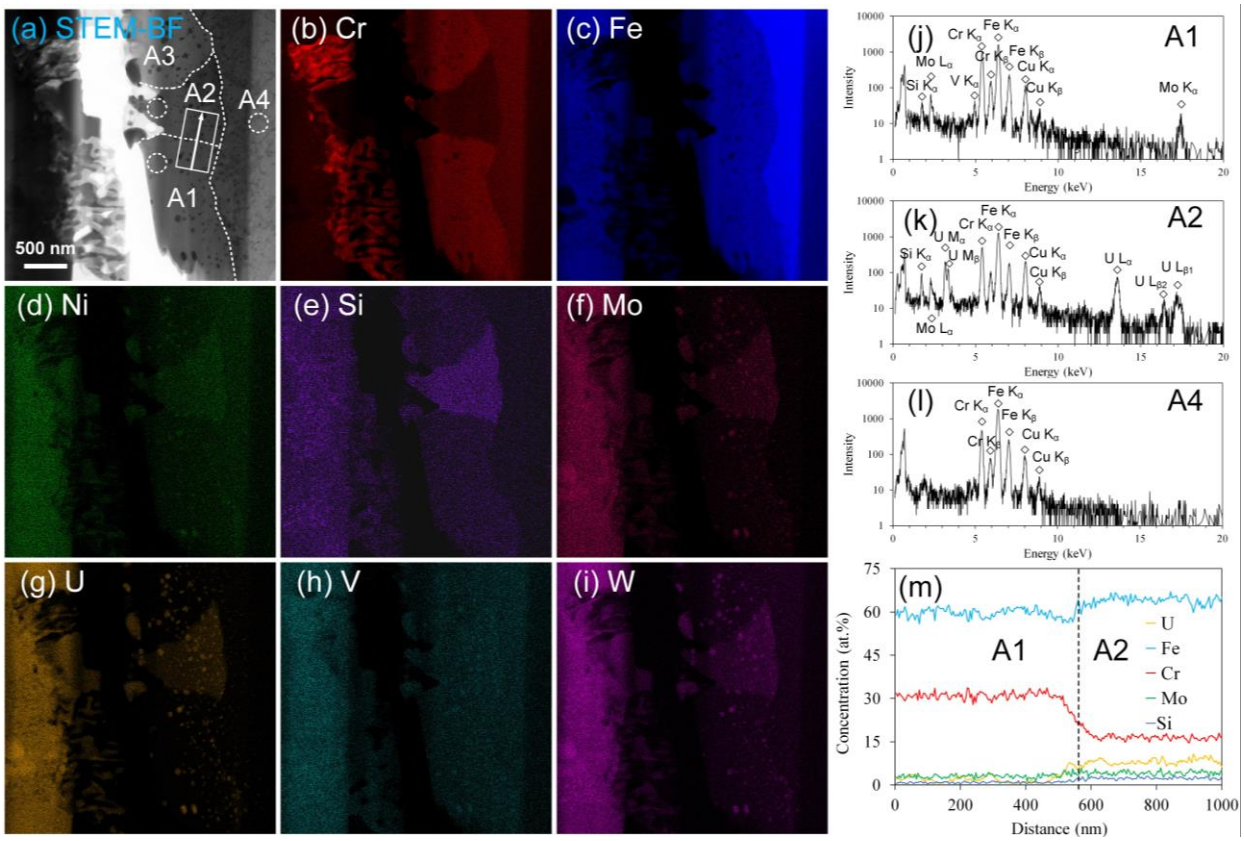

Figure 15. STEM-EDS results of Region III: (a) STEM BF image with four different areas indicated by A1, A2, A3, and A4, (b)–(i) raw intensity maps of Cr, Fe, Ni, Si, Mo, U, V, and W, respectively, (j)–(l) log-scale EDS spectrum corresponding to the areas indicated by dotted circles in A1, A2, and A4, respectively, and (m) EDS linescan from A1 to A2, as indicated by the arrow in (a).

TEM diffraction patterns were then used to identify the crystal structure of the two different phases in Region III, and the results are shown in Figure 16. The diffraction patterns of areas A1 and A3 match well with the binary Fe-Cr σ phase (space group $P4_2/mnm$), as shown by the indexed diffraction patterns of A1 (Figure 16 (b)) and A3 (Figure 16 (g)), respectively. Four diffraction patterns of area A2 were taken, and all four patterns matched well with the quaternary $UCr_{0.1}Fe_{9.9}Si_2$ phase (space group I4/mmm), as shown by the indexed patterns in Figure 16 (c)–(f). In addition, the indexed diffraction pattern of area A4 (Region IV) in Figure 16 (h) confirms that it is the body-centered cubic (BCC) ferrite (α-Fe) phase.

Although the crystal structure of the two phases in Region III was identified, it should be noted that the composition of these two phases differs from those of the standard σ phase and $UCr_{0.1}Fe_{9.9}Si_2$ phase. The σ phase contained only ~30.8 at% Cr and a small amount of Mo. Although there are some discrepancies between calculated Fe-Cr phase diagrams [40–42], the Cr content of the σ phase ranges from ~43% to ~52%, depending on the temperature. The composition of the Fe-Cr-U-Si phase contained less Fe, much more Cr, and much less Si, than the standard $UCr_{0.1}Fe_{9.9}Si_2$ phase.

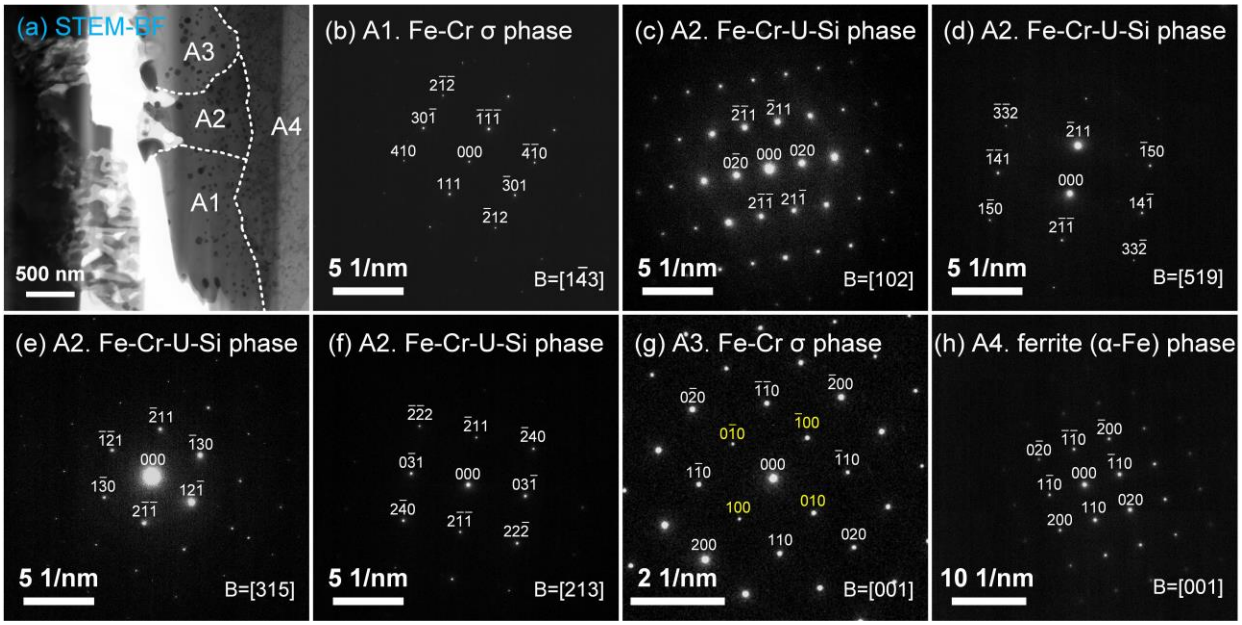

Figure 16. TEM results of the phases in Region III and Region IV: (a) STEM-BF image with areas marked as A1, A2, A3, and A4, (b) diffraction pattern of A1, (c)–(f) diffraction patterns of four different zones of A2, (g) diffraction pattern of A3, and (h) diffraction pattern of A4.

As shown in Figure 16 (h), area A4 in Region IV was identified as the ferrite (α-Fe) phase. However, as displayed in Figure 14 (g), the average Cr concentration of Region IV has increased to ~18 at%, and the average Fe concentration has decreased to ~76 at%, which are significantly different from the composition of unreacted HT-9 (~12.19 at% Cr) before irradiation. The increase in Cr concentration and decrease in Fe concentration in the cladding are apparently the result of the diffusion of Fe from the cladding into the fuel, as shown by the observed $(\mathbf{U},Zr)_6Fe$ and $(\mathbf{U},Zr)(\mathbf{Fe},Cr)_2$ phases. Because of the diffusion of Fe, a spatial gradient is expected along the diffusion direction. A closer look at the chemical composition inside the cladding region (Region IV) shows that the Cr and Fe concentrations are indeed not constant but are dependent on the radial location. The results are shown in Figure 17. It is apparent that the Cr content is much higher than ~12.19 at%, and it decreases with increasing distance from the interaction region.

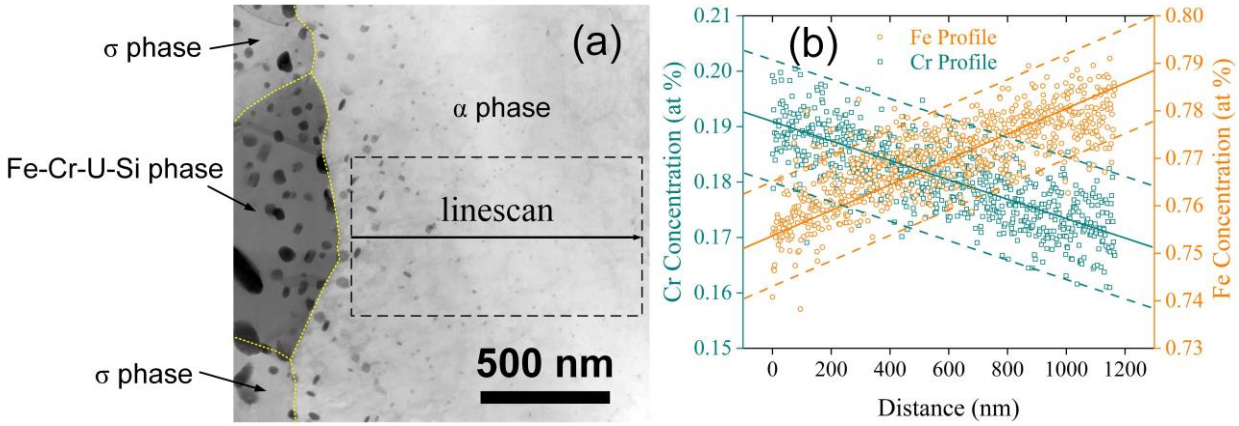

Figure 17. STEM-EDS results of the ferrite (α-Fe) phase: (a) STEM-BF image showing the microstructure of the α-Fe phase, σ phase, and Fe-Cr-U-Si phase, and (b) EDS linescan showing the Fe and Cr profiles. The EDS linescan area is marked by dotted black lines in (a).

HT-9 is a well-known Fe-12Cr ferritic/martensitic steel that has shown excellent swelling resistance in previous irradiation studies. The microstructure of HT-9 is composed of a tempered martensite structure, and the martensite lath is typically several hundred nanometers in width. Both Figure 17 (a) and Region IV in Figure 9 show that the martensite lath structure has disappeared, with only relatively large ferrite (α-Fe) grains in Region IV. This phenomenon can be more clearly seen from the low-magnification backscattered electron image in Figure 18, which shows that the grains close to the FCCI region become equiaxed ferrite grains, whereas the grains near the outer surface of the cladding still maintains the martensite lath structure. The equiaxed ferrite grain structure was even found at regions ~200 μm away from the FCCI region.

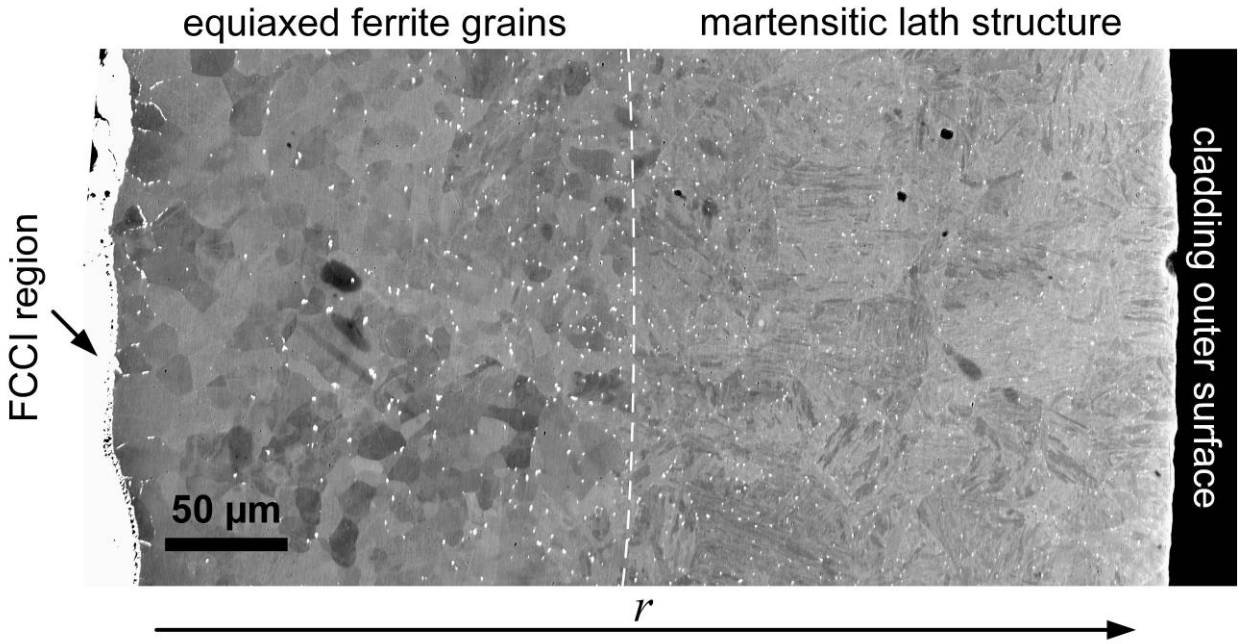

Figure 18. Backscattered electron image showing an overview of the microstructure of the cladding at different radial locations. The white dots are mostly carbides.

The disappearing of the martensite lath structure in the inner region of the cladding is likely due to the diffusion of carbon into the wastage zone, which also resulted in the aforementioned UC precipitates in the (**U**,Zr)(**Fe**,Cr)$_2$ phase. The loss of carbon destabilizes the martensite structure, and ferrite grains are formed instead. The area affected by decarbonization extended much deeper (~200 μm) into the cladding compared with the size of the wastage zone. A similar decarbonization and ferrite formation process in HT-9 cladding after FCCI was mentioned in a previous study [3], in which it was reported that in a solid U-10Zr fuel with HT-9 cladding, a decarbonized zone of ~100 um was developed after 5 at% burnup.

4. Discussions

4.1 Distribution of lanthanides

One of the most unique features of this irradiated U-10Zr fuel is the spatial distribution of the lanthanides. Previous studies [14,32] of solid U-Zr fuel with HT-9 cladding have found significant amount of lanthanides, primarily neodymium and cerium, in the FCCI region at high burnup (> 10 at%). Some low burnup studies [27,39] also confirmed similar behaviors of lanthanides in solid U-Zr fuels. A study [39] of the historical X447 EBR-II experiment indicated that lanthanide fission products were already present in the FCCI region in the DP-69 pin at a local burnup as low as 2.4% FIMA and an average PICT of 667 °C. A recent study of Mechanistic Fuel Failure-3 (MFF-3) experiment showed significant lanthanide distribution in the FCCI region in fuel pin #193045, which has a local burnup of 5.7 % FIMA and an average PICT of 615 °C. Thus, it is believed that the lanthanides in solid U-10Zr fuel can transport and redistribute to the FCCI region even at relatively low burnup. In contrast, almost no lanthanides were found in the FCCI region in this present work. Instead, most lanthanides were found to be retained in the center region where the Zr-rich phase is dominant. The lanthanides observed in the FCCI layer in previous solid U-Zr fuel studies were assumed to be driven by liquid-like diffusion [32] through the fuel pores that were partially filled with sodium and cesium, followed by similar liquid-like diffusion through the sodium bond from the fuel surface to the cladding. In the annular fuel, helium gas replaced the liquid sodium bond. Therefore, the liquid-like diffusion through fuel pores and from the fuel surface to the cladding is significantly suppressed. The fact that much less lanthanides were found in helium back-filled annular fuel might indirectly support the liquid-like diffusion mechanism of lanthanides, which has not been determined yet.

The lanthanide behavior in the annular fuel indicates that the annular fuel using helium bond could be a promising alternative fuel form for fast reactor applications. Elimination of sodium can not only provide back-end fuel cycle benefits but also offer an alternative way to mitigate the transport of lanthanides to the FCCI region by suppressing the liquid-like diffusion mechanism. Further irradiation testing is needed to confirm the lanthanide distribution at higher burnups.

4.2 (**U**,Zr)$_6$Fe and (**U**,Zr)(**Fe**,Cr)$_2$ phases due to interdiffusion of uranium and iron

The interdiffusion of U and Fe near the FCCI region formed tetragonal (**U**,Zr)$_6$Fe phase and cubic (**U**,Zr)(**Fe**,Cr)$_2$ phase. The (**U**,Zr)$_6$Fe is located near the edge of the fuel, and the (**U**,Zr)(**Fe**,Cr)$_2$ phase is in the wastage zone inside the cladding. These two phases are similar to those found in previous U-Fe diffusion couple studies [15–22]. However, the microstructure of the irradiated (**U**,Zr)(**Fe**,Cr)$_2$ phase is much more complicated than the pure UFe_2 phase formed in diffusion couple studies. As shown in Figure 13, the (**U**,Zr)(**Fe**,Cr)$_2$ phase contains a high density of voids and intergranular UC precipitates, indicating that the intermetallic (**U**,Zr)(**Fe**,Cr)$_2$ phase is susceptible to void swelling under irradiation and can therefore degrade the mechanical property of the inner cladding region.

4.3 Compositional and microstructural changes in the cladding

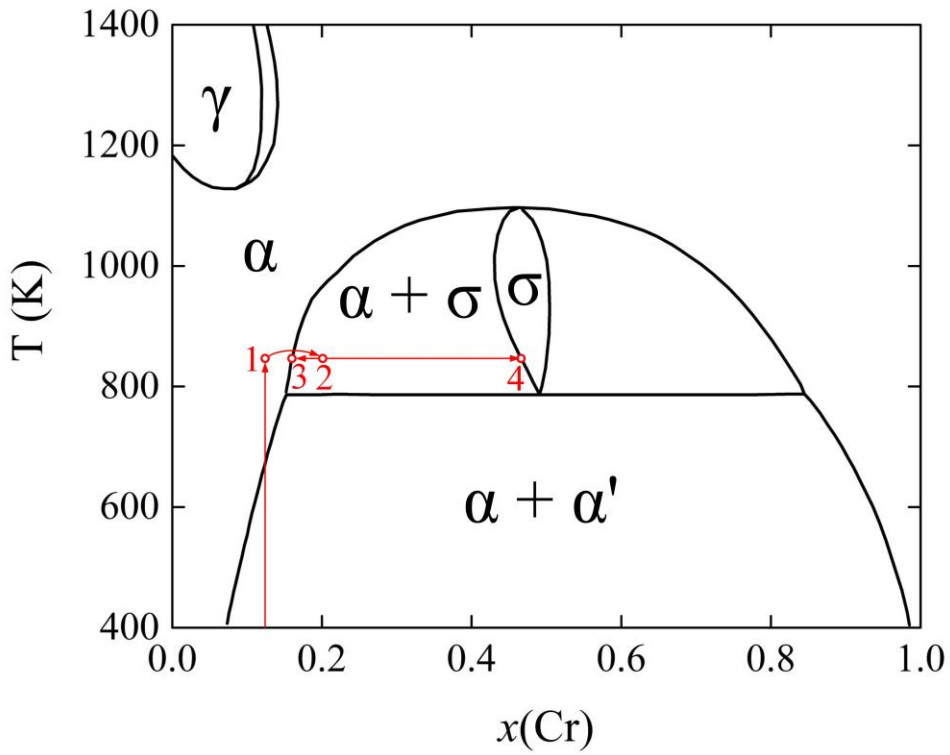

Figure 19. A likely pathway of the observed phase transformation in Region III based on the current Fe-Cr phase diagram [43].

At the cladding side of the interface of the interdiffusion zone and the cladding region (Region III), two different phases were observed: the Fe-Cr σ phase and the tetragonal Fe-Cr-U-Si phase. These two phases are different from the original ferrite/martensite α-Fe phase of HT-9, indicating that phase transformation has occurred at the inner surface of the cladding. Since the unirradiated HT-9 contains only ~12.19 at% Cr, such phase transformation was not expected. A likely pathway for such phase transformation is shown on the Fe-Cr phase diagram [43] in Figure 19. The unirradiated HT-9 contains ~12.19 at% Cr. Therefore, the starting point is somewhere inside the miscibility gap (α+α' region). At the beginning of irradiation, the cladding temperature was raised to ~540 ºC (813 K), and the system was brought to point 1. With increasing burnup, Fe started to diffuse into the fuel, and the Cr content of the most inner region of the cladding started to increase correspondingly. This causes the system to move from point 1 to point 2, passing the α–σ phase boundary. Now the system is thermodynamically favorable to decompose into the σ phase (point 4) and the α phase (point 3). The σ phase is one of the two phases observed in Region III. However, because of the diffusion of uranium into the cladding, the other phase, the α phase, was further transformed to the Fe-Cr-U-Si phase. It should be noted that the compositions of the Fe-Cr σ phase and the tetragonal Fe-Cr-U-Si phase differ from the compositions of the equilibrium σ phase and the standard $UCr_{0.1}Fe_{9.9}Si_2$ phase, respectively. A likely reason is that these two phases were under neutron irradiation and were not at equilibrium. It should also be noted that both phases contain significant amount of uranium carbide precipitates, due to the interdiffusion of U and C.

Two conditions are needed to result in the observed phase transformation: noticeable diffusion of Fe away from the cladding to raise the Cr content and temperature high enough to enter the α+σ region. The brittle σ phase could result in cladding embrittlement. To avoid such phase transformation, ways to suppress the

diffusion of Fe into the fuel would be helpful (e.g., introduce internal sinks into the cladding to suppress radiation-enhanced diffusion).

The diffusion of Fe not only resulted in the phase transformation at the inner surface of the cladding, but also raised the Cr content in Region IV inside the cladding. For lower temperature irradiation, the increase in Cr content moves the system further into the α+α' region and can potentially enhance the formation of the brittle α' phase [44–46].

Another consequence of the FCCI is that the martensite lath structure at the inner side of the cladding is gone, possibly due to decarbonization caused by the diffusion of C into the wastage zone. The martensite structure is characterized by high densities of dislocations and lath structure. This is different from the α phase shown in Figure 17, indicating that the original martensite has transformed to the ferrite phase. Uranium carbide precipitates were found in the ferrite (α-Fe) grains in Region IV. The carbides appear as small precipitates inside the ferrite grains (Figure 17) and as large precipitates at the ferrite grain boundaries (Figure 6 and Figure 9) and the phase boundaries between Region III and Region IV. The uranium carbide precipitates were only found in the first ~15–30 μm region away from the interface, and the equiaxed ferrite grain structure extended ~200 μm deep into the cladding.

These changes in the composition and microstructure of the region near the FCCI layer in the cladding could adversely affect the local mechanical properties and radiation resistance of the cladding. Fuel fabrication defects have a direct impact on the formation and evolution of FCCI layer. Based on the experience of AFC-3A/B irradiation, a final machining step was added after casting of AFC-3C/D annular fuels to ensure a controlled small (<25 μm) gap size, which mitigated FCCI and improved the fuel performance [47].

5. Conclusions

Annular U-Zr fuel is a promising fuel form due to its back-end fuel cycle benefits. Using advanced electron microscopy and spectroscopy characterization techniques, this study revealed the fuel cladding chemical interaction characteristics of a prototype annular U-10wt%Zr fuel and a Fe-12Cr base HT-9 cladding irradiated to 3.3% FIMA. Unlike the solid U-Zr fuels, most lanthanides were retained in the newly formed UZr_2 phase in the center region of the irradiated annular U-10Zr fuel, suggesting an alternative way to mitigate the transport of lanthanides to the FCCI region. Higher burnup irradiation testing is required to confirm whether the center UZr_2 phase region can still retain the lanthanides at higher burnups.

Based on the microstructure results, the microstructural evolution near the FCCI region of the investigated annular U-10Zr fuel with HT-9 cladding is illustrated in Figure 20.

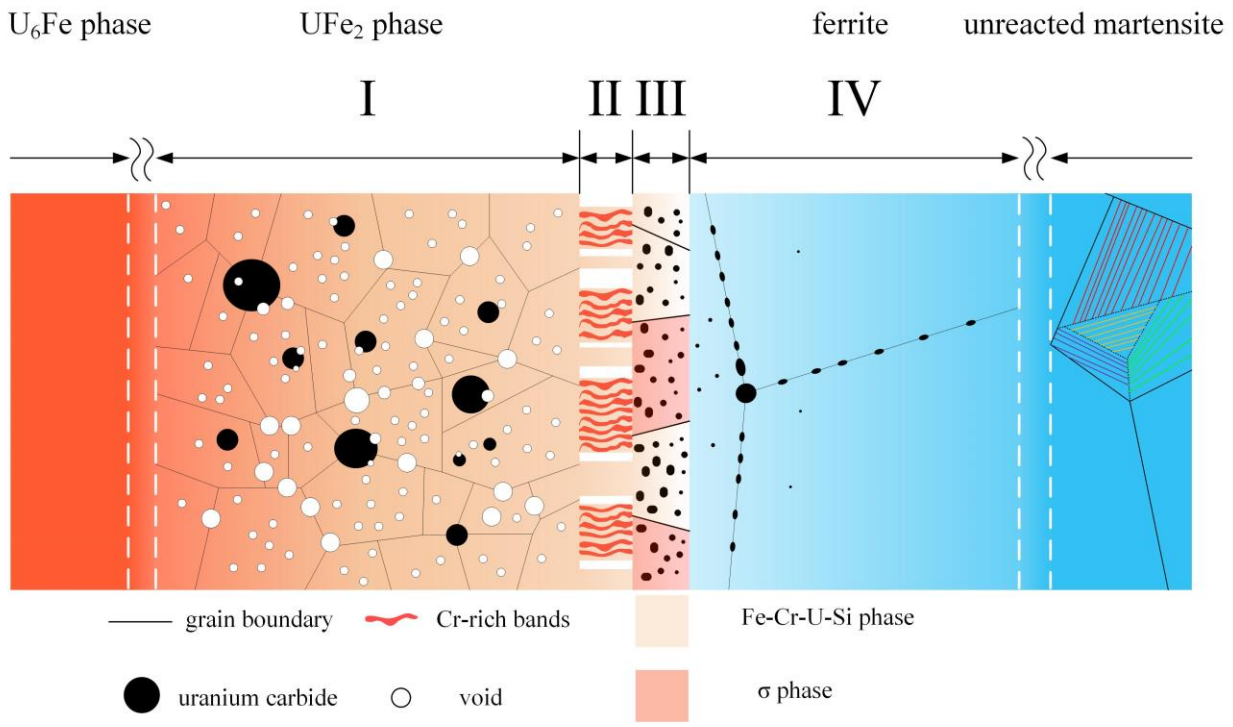

Figure 20. Illustration of the microstructural evolution near the FCCI region.

In the FCCI interdiffusion region, cubic (**U**,Zr)(**Fe**,Cr)$_2$ phase and tetragonal (**U**,Zr)$_6$Fe phase were formed. The (**U**,Zr)(**Fe**,Cr)$_2$ phase contained a significant number of voids and UC precipitates. Most of the voids are spatially associated with the UC precipitates.

At the interface region (Region II and Region III), a lamellar structure was found on the interdiffusion zone side (Region II), and phase transformation was identified on the cladding side (Region III). The lamellar structure is composed of alternating U-rich lamellae and Cr-rich lamellae with a typical width of about 160 nm.

Two phases were identified in Region III: the σ phase and the tetragonal Fe-Cr-U-Si phase. The phase transformation in Region III was explained by a pathway on the Fe-Cr phase diagram. The diffusion of Fe (increase in Cr content) from the cladding into the fuel and high temperature (e.g., ~540 ºC) are both required to form the σ phase. The Fe-Cr-U-Si phase was formed due to the diffusion of U into the cladding.

In the inner bulk cladding region (Region IV), martensite lath structure was not observed, and large ferrite grains were found, possibly due to the diffusion of C into the wastage zone. The Cr content of the ferrite grains is much higher (~18 at%) than that of the unirradiated HT-9 (~12.19 at%), and the ferrite grains contain small intragranular uranium carbide precipitates and large intergranular uranium carbide precipitates. Uranium carbide precipitates were found only in the first ~15–30 μm region away from the interface. These microstructural and compositional changes of the cladding could result in local degradation of mechanical properties and radiation resistance.

It should be noted that this prototype annular fuel had imperfect cylindricity, and the actual local cladding temperature varied at different locations depending on the local fuel-cladding gap size. In some locations, the local cladding temperature was much hotter than expected. Improvements of the fuel fabrication processes, especially a final machining step was adopted for AFC-3C/D annular fuel slugs to ensure a controlled small fuel-cladding gap size, and the fuel performance was significantly improved.

Acknowledgment

X. Liu acknowledges the financial support from the U.S. Department of Energy, Office of Nuclear Energy under DOE Idaho Operations Office Contract DEAC07-051D14517 as part of a Nuclear Science User Facilities. T. Yao and L. He acknowledge the support from the Center for Thermal Energy Transport under Irradiation, an Energy Frontier Research Center funded by the U.S. Department of Energy, Office of Science, Basic Energy Sciences. This work was supported by the Advanced Fuels Campaign (AFC) of the Nuclear Technology Research and Development (NTRD) program in the U.S. Department of Energy, Office of Nuclear Energy under DOE Idaho Operations Office Contract DE-AC07-05ID14517. Accordingly, the U.S. Government retains and the publisher, by accepting the article for publication, acknowledges that the U.S. Government retains a nonexclusive, paid-up, irrevocable, worldwide license to publish or reproduce the published form of this manuscript or allow others to do so, for U.S. Government purposes.

References

[1] K. Aoto, P. Dufour, Y. Hongyi, J.P. Glatz, Y. Kim, Y. Ashurko, R. Hill, N. Uto, A summary of sodium-cooled fast reactor development, Prog. Nucl. Energy. 77 (2014) 247–265. doi:10.1016/j.pnucene.2014.05.008.

[2] S. Hayes, D. Dempsey, J.M. Harp, G.L. Povirk, Developmental Objectives for Advanced Reactor Fuels, Idaho Falls, ID (United States), 2017. doi:10.2172/1599357.

[3] G.L. Hofman, L.C. Walters, T.H. Bauer, Metallic fast reactor fuels, Prog. Nucl. Energy. 31 (1997) 83–110. doi:10.1016/0149-1970(96)00005-4.

[4] W.J. Carmack, D.L. Porter, Y.I. Chang, S.L. Hayes, M.K. Meyer, D.E. Burkes, C.B. Lee, T. Mizuno, F. Delage, J. Somers, Metallic fuels for advanced reactors, J. Nucl. Mater. 392 (2009) 139–150. doi:10.1016/j.jnucmat.2009.03.007.

[5] D.C. Crawford, D.L. Porter, S.L. Hayes, Fuels for sodium-cooled fast reactors: US perspective, J. Nucl. Mater. 371 (2007) 202–231. doi:10.1016/j.jnucmat.2007.05.010.

[6] Y.-I. Chang, TECHNICAL RATIONALE FOR METAL FUEL IN FAST REACTORS, Nucl. Eng. Technol. 39 (2007) 161–170. doi:10.5516/NET.2007.39.3.161.

[7] G.L. Hofman, R.G. Pahl, C.E. Lahm, D.L. Porter, Swelling behavior of U-Pu-Zr fuel, Metall. Trans. A. 21 (1990) 517–528. doi:10.1007/BF02671924.

[8] C.B. Lee, D.H. Kim, Y.H. Jung, Fission gas release and swelling model of metallic fast reactor fuel, J. Nucl. Mater. 288 (2001) 29–42. doi:10.1016/S0022-3115(00)00718-2.

[9] C. Matthews, C. Unal, J. Galloway, D.D. Keiser, S.L. Hayes, Fuel-Cladding Chemical Interaction in U-Pu-Zr Metallic Fuels: A Critical Review, Nucl. Technol. 198 (2017) 231–259. doi:10.1080/00295450.2017.1323535.

[10] D.D. Keiser, Fuel cladding chemical interaction in metallic sodium fast reactor fuels: A historical perspective, J. Nucl. Mater. 514 (2019) 393–398. doi:10.1016/j.jnucmat.2018.09.045.

[11] D.L. Porter, C.B. Hilton, Extending Sodium Fast Reactor Driver Fuel Use to Higher Temperatures, Nucl. Technol. 173 (2011) 218–225. doi:10.13182/NT11-A11551.

[12] L.R. Blake, Achieving high burn-up in fast reactors, J. Nucl. Energy. Parts A/B. React. Sci. Technol. 14 (1961) 31–48. doi:10.1016/0368-3230(61)90071-4.

[13] J.M. Harp, H.J.M. Chichester, L. Capriotti, Postirradiation examination results of several metallic fuel alloys and forms from low burnup AFC irradiations, J. Nucl. Mater. 509 (2018) 377–391. doi:10.1016/j.jnucmat.2018.07.003.

[14] D.D. Keiser, Fuel-cladding interaction layers in irradiated U-Zr and U-Pu-Zr fuel elements, Argonne, IL (United States), 2006. doi:10.2172/885496.

[15] T. Ogata, M. Kurata, K. Nakamura, A. Itoh, M. Akabori, Reactions between U–Zr alloys and Fe at 923 K, J. Nucl. Mater. 250 (1997) 171–175. doi:10.1016/S0022-3115(97)00262-6.

[16] T. Chen, T.A. Smith, J.G. Gigax, D. Chen, R. Balerio, L. Shao, B.H. Sencer, J.R. Kennedy, Intermetallic formation and interdiffusion in diffusion couples made of uranium and single crystal iron, J. Nucl. Mater. 467 (2015) 82–88. doi:10.1016/j.jnucmat.2015.05.026.

[17] D.D. Keiser, M.A. Dayananda, Interdiffusion between U-Zr fuel vs selected cladding steels, Metall. Mater. Trans. A. 25 (1994) 1649–1653. doi:10.1007/BF02668530.

[18] D.D. Keiser, M.A. Dayananda, Interdiffusion between U-Zr fuel and selected Fe-Ni-Cr alloys, J. Nucl. Mater. 200 (1993) 229–243. doi:10.1016/0022-3115(93)90334-U.

[19] K. Huang, Y. Park, A. Ewh, B.H. Sencer, J.R. Kennedy, K.R. Coffey, Y.H. Sohn, Interdiffusion and reaction between uranium and iron, J. Nucl. Mater. 424 (2012) 82–88. doi:10.1016/j.jnucmat.2012.02.004.

[20] Y. Park, K. Huang, A. Paz y Puente, H.S. LEE, B.H. Sencer, J.R. Kennedy, Y.H. Sohn, Diffusional Interaction Between U-10 wt pct Zr and Fe at 903 K, 923 K, and 953 K (630 °C, 650 °C, and 680 °C), Metall. Mater. Trans. A. 46 (2015) 72–82. doi:10.1007/s11661-014-2277-2.

[21] C.T. Lee, H. Kim, T.K. Kim, C.B. Lee, Diffusion behavior in an interface between U–10Zr alloy and HT-9 steel, J. Nucl. Mater. 395 (2009) 140–144. doi:10.1016/j.jnucmat.2009.10.044.

[22] Y. Xie, M.T. Benson, L. He, J.A. King, R.D. Mariani, D.J. Murray, Diffusion behaviors between metallic fuel alloys with Pd addition and Fe, J. Nucl. Mater. 525 (2019) 111–124. doi:10.1016/j.jnucmat.2019.07.028.

[23] M. Kurata, T. Ogata, K. Nakamura, T. Ogawa, Thermodynamic assessment of the Fe–U, U–Zr and Fe–U–Zr systems, J. Alloys Compd. 271–273 (1998) 636–640. doi:10.1016/S0925-8388(98)00176-5.

[24] T. OGATA, K. NAKAMURA, M. KURATA, T. YOKOO, M.A. MIGNANELLI, Reactions between U-Pu-Zr Alloys and Fe at 923 K, J. Nucl. Sci. Technol. 37 (2000) 244–252. doi:10.1080/18811248.2000.9714890.

[25] M. Kurata, K. Nakamura, T. Ogata, Thermodynamic evaluation of the quaternary U–Pu–Zr–Fe

system – assessment of cladding temperature limits of metallic fuel in a fast reactor, J. Nucl. Mater. 294 (2001) 123–129. doi:10.1016/S0022-3115(01)00473-1.

[26] J.M. Harp, L. Capriotti, D.L. Porter, J.I. Cole, U-10Zr and U-5Fs: Fuel/cladding chemical interaction behavior differences, J. Nucl. Mater. 528 (2020) 151840. doi:10.1016/j.jnucmat.2019.151840.

[27] J.M. Harp, D.L. Porter, B.D. Miller, T.L. Trowbridge, W.J. Carmack, Scanning electron microscopy examination of a Fast Flux Test Facility irradiated U-10Zr fuel cross section clad with HT-9, J. Nucl. Mater. 494 (2017) 227–239. doi:10.1016/j.jnucmat.2017.07.040.

[28] A.E. Bridges, A.E. Waltar, R.D. Leggett, R.B. Baker, J.L. Ethridge, A Liquid-Metal Reactor Core Demonstration Experiment Using HT-9, Nucl. Technol. 102 (1993) 353–366. doi:10.13182/NT93-A17034.

[29] R.G. Pahl, D.L. Porter, C.E. Lahm, G.L. Hofman, Experimental studies of U-Pu-Zr fast reactor fuel pins in the experimental breeder reactor-ll, Metall. Trans. A. 21 (1990) 1863–1870. doi:10.1007/BF02647233.

[30] L.. Walters, Thirty years of fuels and materials information from EBR-II, J. Nucl. Mater. 270 (1999) 39–48. doi:10.1016/S0022-3115(98)00760-0.

[31] A.B. Cohen, H. Tsai, L.A. Neimark, Fuel/cladding compatibility in U-19Pu-10Zr/HT9-clad fuel at elevated temperatures, J. Nucl. Mater. 204 (1993) 244–251. doi:10.1016/0022-3115(93)90223-L.

[32] R.D. Mariani, D.L. Porter, T.P. O'Holleran, S.L. Hayes, J.R. Kennedy, Lanthanides in metallic nuclear fuels: Their behavior and methods for their control, J. Nucl. Mater. 419 (2011) 263–271. doi:10.1016/j.jnucmat.2011.08.036.

[33] R.S. Fielding, P.A. Hansen, T.A. Hyde, J. Maupin, Fabrication Report for the FY11 Phases of the AFC-3A and 3B Irradiation Experiments, Idaho Natl. Lab. Rep. (2011) INL/LTD-11-23158.

[34] T.P. O'Holleran, C.A. Papesch, L.N. Squires, T.A. Hyde, J.R. Kennedy, T. Hartmann, AFC-3 Fuel Characterization, Idaho Natl. Lab. Rep. (2012) INL/LTD-12-24346.

[35] G.S. Chang, R.G. Ambrosek, Hardening neutron spectrum for advanced actinide transmutation experiments in the ATR, Radiat. Prot. Dosimetry. 115 (2005) 63–68. doi:10.1093/rpd/nci167.

[36] J.M. Harp, S.L. Hayes, P.G. Medvedev, D.L. Porter, L. Capriotti, Testing Fast Reactor Fuels in a Thermal Reactor: A Comparison Report, Idaho Natl. Lab. Rep. (2017) INL/EXT-17-41677. doi:10.2172/1458766.

[37] P. Medvedev, S. Hayes, S. Bays, S. Novascone, L. Capriotti, Testing fast reactor fuels in a thermal reactor, Nucl. Eng. Des. 328 (2018) 154–160. doi:10.1016/j.nucengdes.2017.12.034.

[38] P.G. Medvedev, BISON Investigation of the Effect of the Fuel- Cladding Contact Irregularities on the Peak Cladding Temperature and FCCI Observed in AFC-3A Rodlet 4, Idaho Falls, ID (United States), 2016. doi:10.2172/1364503.

[39] William J. Carmack, Temperature and Burnup Correlated FCCI in U-10Zr Metallic Fuel, 2012. doi:10.2172/1055966.

[40] J.-O. Andersson, B. Sundman, Thermodynamic properties of the Cr-Fe system, Calphad. 11 (1987) 83–92. doi:10.1016/0364-5916(87)90021-6.

[41] W. Xiong, M. Selleby, Q. Chen, J. Odqvist, Y. Du, Phase Equilibria and Thermodynamic Properties in the Fe-Cr System, Crit. Rev. Solid State Mater. Sci. 35 (2010) 125–152.

doi:10.1080/10408431003788472.

[42] A. Jacob, E. Povoden-Karadeniz, E. Kozeschnik, Revised thermodynamic description of the Fe-Cr system based on an improved sublattice model of the σ phase, Calphad. 60 (2018) 16–28. doi:10.1016/j.calphad.2017.10.002.

[43] W. Xiong, P. Hedström, M. Selleby, J. Odqvist, M. Thuvander, Q. Chen, An improved thermodynamic modeling of the Fe–Cr system down to zero kelvin coupled with key experiments, Calphad. 35 (2011) 355–366. doi:10.1016/j.calphad.2011.05.002.

[44] O. Anderoglu, J. Van den Bosch, P. Hosemann, E. Stergar, B.H. Sencer, D. Bhattacharyya, R. Dickerson, P. Dickerson, M. Hartl, S.A. Maloy, Phase stability of an HT-9 duct irradiated in FFTF, J. Nucl. Mater. 430 (2012) 194–204. doi:10.1016/j.jnucmat.2012.06.038.

[45] C. Zheng, E.R. Reese, K.G. Field, E. Marquis, S.A. Maloy, D. Kaoumi, Microstructure response of ferritic/martensitic steel HT9 after neutron irradiation: effect of dose, J. Nucl. Mater. 523 (2019) 421–433. doi:10.1016/j.jnucmat.2019.06.019.

[46] E.R. Reese, M. Bachhav, P. Wells, T. Yamamoto, G. Robert Odette, E.A. Marquis, On α′ precipitate composition in thermally annealed and neutron-irradiated Fe- 9-18Cr alloys, J. Nucl. Mater. 500 (2018) 192–198. doi:10.1016/j.jnucmat.2017.12.036.

[47] J.M. Harp, L. Capriotti, F. Cappia, Baseline Postirradiation Examination of the AFC-3C, AFC-3D, and AFC-4A Experiments, Idaho Falls, ID (United States), 2018. doi:10.2172/1498255.

Credit Author Statement

X. Liu: Conceptualization; Data curation; Formal analysis; Investigation; Visualization; Project administration; Writing – review & editing; Roles/Writing – original draft.

L. Capriotti: Conceptualization; Investigation; Visualization; Funding acquisition; Writing – review & editing; Roles/Writing – original draft.

T. Yao: Conceptualization; Data curation; Formal analysis; Investigation; Visualization; Writing – review & editing

J.M. Harp: Conceptualization; Investigation; Visualization; Writing – review & editing

M. T. Benson: Conceptualization; Investigation; Visualization; Funding acquisition; Writing – review & editing.

Y. Wang: Investigation; Visualization; Writing – review & editing.

F. Teng: Investigation; Visualization; Writing – review & editing.

L. He: Investigation; Visualization; Funding acquisition; Writing – review & editing.

Declaration of interests

☒ The authors declare that they have no known competing financial interests or personal relationships that could have appeared to influence the work reported in this paper.

☐The authors declare the following financial interests/personal relationships which may be considered as potential competing interests:
